Swansea University
Prifysgol Abertawe

Multiscale Deformation Modelling of Small Scale Mechanical Tests

Dissertation Submitted to Swansea University
in fulfilment of the requirements for the Degree of
Doctor of Engineering

Tristan Hearsey McKay

BEng

Swansea University

Abstract

Novel techniques that accelerate the development of new steel alloys by combining miniaturised tests with modelling techniques is key for TATA steel to remain competitive. The research undertaken here modelled the deformation of small-scale mechanical tests of dual-phase steels as part of a Rapid Alloying Process. This was achieved via a multiscale approach using finite element models developed in ABAQUS to simulate deformation of shear punch tests at the continuum level and microstructural deformation modelling via representative volume elements using synthetically generated microstructures. An axisymmetric modelling approach was first used to validate geometrical parameters of the shear punch test. This showed that the radius of the punch head and corner tip radiuses are key aspects that must be controlled for when setting up experimental test rigs to ensure that shear dominant deformation takes place and minimize other deformation mechanisms like bending or stretching of test pieces. A 3D half-symmetry model was developed to review advanced damage mechanisms that develop during shear punch tests. From this it was concluded that due to the multiphase nature of dual phase steels, continuum modelling alone is not enough to characterise the deformation of dual phase steels. Whilst strength characteristics of dual phase correlated well with experimental tests the ductility and elongation values did not correlate with real world experimentation. Microstructural deformation was modelled using representative volume elements to characterise the deformation of a pure ferrite-martensite dual phase steel using both 2D and 3D models. Synthetic models using a composite approach with variable martensite content were successfully used to review dual phase steel deformation, generating better results than using a real microstructure. This work produced a plug-in script which was used to automatically generate 2D microstructural models of dual phase steels whose parameters could easily be varied. Whilst the 2D microscale modelling approach was not exhaustive in accounting for all characteristics of dual phase alloy, it did show that composite modelling of these kinds of steels can be used to generate reliable predictions of mechanical properties and deformation evolution when used for the development prototype steel alloys as part of a Rapid Alloy Prototyping process.

If you DON'T have a bar on access, include the declarations below

Declarations

This work has not previously been accepted in substance for any degree and is not being concurrently submitted in candidature for any degree.

Signed [redacted] .....

Date 10/08/2025 .....

This thesis is the result of my own investigations, except where otherwise stated. Other sources are acknowledged by footnotes giving explicit references. A bibliography is appended.

Signed [redacted] .....

Date 10/08/2025 .....

I hereby give consent for my thesis, if accepted, to be available for photocopying and for inter-library loan, and for the title and summary to be made available to outside organisations.

Signed [redacted] .....

Date 10/08/2025 .....

The University's ethical procedures have been followed and, where appropriate, that ethical approval has been granted.

Signed. [redacted] .....

Date 10/08/2025 .....

Contents

Abstract ii

Declarations iii

List of Figures ix

List of Tables xiii

Acknowledgements xv

Nomenclature xvi

1 Introduction 1

1.1 Motivation 1

1.2 Overview and Structure of the Thesis 2

2 Literature Review 4

2.1 Introduction 4

2.2 Steel Prototyping and Small Scale Manufacturing & Testing 4

2.2.1 RAP 20-40g 5

2.2.2 RAP 200g 6

2.2.3 RAP 4.5kg 7

2.3 Small Punch Testing 7

2.3.1 History and Background 7

2.3.2 Test Set-Up 8

2.3.3 Outputs 9

2.4 Obtaining Material properties 10

2.4.1 Tolerances 11

2.5 Shear Punch Testing 12

2.6 Nakajima Test 17
2.7 Small Scale Tensile Tests 19
2.7.1 Miniaturized Tensile Bar Tests 19
2.8 Finite Element Method 21
2.8.1 What is the Finite Element Method? 21
2.8.2 Implicit vs Explicit Time Integration 22
2.8.3 FEM in Punch Testing 24
2.8.4 Small Scale Modelling in FEM 27
2.8.5 Dual Phase Steel Alloys 28
2.8.6 Deformation of DP Steels 33
2.9 Summary 36
3 Experimental Shear Punch Testing 37
3.1 Introduction 37
3.2 Materials Selected 37
3.3 Experimental Test Setup 37
3.4 Sample Preparation 38
3.5 Results 40
3.5.1 Thickness Effects 42
3.6 Summary 43
4 Axisymmetric Modelling & Parameter Study 44
4.1 Introduction 44
4.2 Parameter Study Objectives 44
4.2.1 Parameters Investigated 45
4.3 Model Set-Up 45

4.3.1 Primary Geometry of Master Parts 45
4.3.2 Part Interactions 49
4.3.3 Meshing of Deformable Parts 50
4.3.4 Boundary Conditions 51
4.4 Mesh Sensitivity Analysis 52
4.5 Results XY Data Plots 56
4.5.1 Friction 57
4.5.2 Effects of Sample Thickness 58
4.5.3 Radial Clearance 62
4.5.4 Punch and Die Corner Tip Radius 65
4.6 Shear Yield Points 68
4.7 Evolution of Stress during Shear Punch Test 72
4.8 Summary 74
5 3D Model 76
5.1 Introduction 76
5.2 Strategic Reason for going into the 3D model 76
5.3 Constructing the Parts 77
5.3.1 Punch 77
5.3.2 Clamp 78
5.3.3 Die 78
5.3.4 Disc 79
5.3.5 Half-Symmetry & Quarter Symmetry 80
5.3.6 Mesh 81
5.4 Material Properties 83

5.4.1 Time Step & Mass Scaling 84
5.5 Boundary Conditions 85
5.5.1 Boundary Conditions for Top and Bottom Clamp 86
5.5.2 Boundary Conditions for Half Symmetry 86
5.5.3 Punch Displacement 86
5.5.4 Output Requests 87
5.6 Results 87
5.6.1 Mesh Sensitivity & Corner Tip Radius 88
5.6.2 Simulation Outputs 90
5.6.3 Assembly Stiffness 93
5.7 Summary 94
6 Microscale Modelling of Dual Phase Steel 96
6.1 Introduction 96
6.2 Material Properties, Constitutive Description 96
6.3 2D Microstructure Modelling of a Dual Phase Steel 99
6.3.1 Real Microstructure RVE 99
6.3.2 Applying Material Properties 99
6.3.3 Results from real Dual Phase Steel microstructure 100
6.3.4 Random RVE 103
6.4 Scripting and Development of 2D Representative Volume Element 104
6.4.1 Boundary Conditions and mesh 105
6.5 Results 107
6.5.1 Initial Results for the Boundary Conditions 107
6.5.2 Martensite Vm Surface Fraction Concentration 111

6.5.3 Failure mode for DP in 2D RVE 115
6.5.4 Stress-Strain Distributions for varying martensite concentrations 117
6.6 2D Synthetic RVE Conclusions 122
6.6.1 Randomly Generated Microstructure 122
6.6.2 Real Microstructure 124
6.7 3D Modelling 125
6.7.1 Introduction 125
6.7.2 Developing 3D RVE 125
6.7.3 3D RVE using different mesh approach 128
6.7.4 Visual Results for Stress distribution 129
6.7.5 Visual Results Plastic Strain 131
6.7.6 3D RVE Results 132
6.8 Summary 133
7 Conclusions 134
8 Future Work 136
References 137

List of Figures

Fig. 1 – Typical setup of a SP test [24] 8

Fig. 2 – SPT Load-Deflection curve of a ductile metallic alloy 10

Fig. 3 – Shear Punch Test setup [41] 12

Fig. 4 – Schematic of the Shear Punch rig (in mm) with dimensions shown. a) punch, b) top holder, c) sample disc, & d) lower die 13

Fig. 5 – Schematic of the Shear Punch Test Output [51] 15

Fig. 6 – Offset methodology for determining yield load for ShP test [51] 16

Fig. 7 – Typical ShP Test curve with Shear Stress-Normalized Displacement [50] ... 17

Fig. 8 – Forming Limit Curve for DP800 [61] 18

Fig. 9 – Definition of L_t, L_c, L_0, a_0, b_o and R in **Table 1** from [11] 20

Fig. 10 – Phase Diagram for steel [121] 30

Fig. 11 – The Global Formability Diagram (GFD) of different steel grades showing typical elongation and tensile strengths [111] 31

Fig. 12 – Schematic Diagram of Shear Punch Test setup, vertical axis is cut along the centreline. Pr is the punch radius, R1 is the fillet radius of the lower and upper clamp, R2 is the fillet radius of the punch, Hr is the radius of the receiving hole of the lower die, c is the radial clearance and is the difference in the length between Pr and Hr, Tr is the radius of the sample disc, and t is the sample disc thickness 38

Fig. 13 – Mean Load Deflection curve for typical DP800 and DX57 alloy undergoing Shear Punch test. The curves show mean curves for the DP800 and DX57. 41

Fig. 14 – Force Deflection curves for DP800 alloy, note the variation in the curve for DP800-3 showing an initial higher amount of deformation for a lower punch load 42

Fig. 15 – DP800 Peak Stress when accounting for sample thickness 43

Fig. 16 - Cross Sectional Diagram of parts in ShP Test setup for parameter study 46

Fig. 17 – Engineering Stress-Strain and Trus Stress-Strain curve for DP800 used 48

Fig. 18 – True Plastic Stress-Strain for DP800 used for the material property in the model 49
Fig. 19 – Interaction between surfaces of the Assembly..... 50
Fig. 20 – Cross sectional view of disc, a higher density mesh has been applied in the shear with coarser mesh in areas of low deformation 51
Fig. 21 – Assembly boundary condition applied to the RP in the holder, lower die and punch. No boundary conditions are applied to the test piece and is held in place through friction from the lower die and top holder 52
Fig. 22 – Mesh Density Comparison..... 53
Fig. 23 – Elements in the shear zone comparison with computation time..... 54
Fig. 24 – Coarse mesh in the shear zone..... 55
Fig. 25 – Structured higher density mesh in the shear zone 56
Fig. 26 – Friction effects of the ShP Test 57
Fig. 27 – Effects of sample thickness on load displacement curves in Shear Punch test 59
Fig. 28 – Shear punch tests results expressed as shear stress and normalized displacement. Shear stress is in part a function of the sample thickness 60
F**ig. 29** – Punch load at a specific displacement of 0.05mm and 0.1mm. Increases sample thickness requires an increasing load to obtain an equivalent displacement 61
Fig. 30 – Shear stress and a specific normalized displacement. Effects of sample thickness are reduced once accounted for in stress and normalized displacement 62
Fig. 31 – Effect of varying radial clearance on the shear punch test..... 63
Fig. 32 – Radial Clearance Shear Stress vs Normalized Displacement 64
Fig. 33 – Varying of punch and die fillet radius. The clearance between the punch and dies remains constant. A) radius of 0.05mm B) radius of 0.1mm C) punch radius 0.1mm, die radius 0.2mm 65
Fig. 34 – a) Die Corner Tip Radius 0.1mm & b) Punch Corner Tip Radius 0.1mm 66
Fig. 35 – Effect of varying punch corner tip radius on load displacement curves..... 67

Fig. 36 – Effects of increasing punch corner tip radius from left to right: a) 0.01, b) 0.03mm, c) 0.05mm, and d) 0.1mm 68
Fig. 37 – Simulation Results of Varying Clearances 69
Fig. 38 – Typical Shear Punch Curve with the Intersect 70
Fig. 39 – Showing the impacts of friction on the ShPT 71
Fig. 40 – Evolution of stress in the sample during ShP test. Axisymmetric model with sweep applied to give a 3D view of von Mises stress evolution 73
Fig. 41 – Assembly of the 1/2 symmetry FE ShP Test model 77
Fig. 42 – a) Diagram showing a schematic of the punch and b) the 3D analytical revolution with partition 78
Fig. 43 – a) Diagram schematic of the clamp and b) 3D analytical revolution with partition 78
Fig. 44 – a) Diagram schematic of the die and b) 3D analytical revolution with partition 79
Fig. 45 – a) Schematic of the disc and b) 3D analytical part with partition 79
Fig. 46 – 2D schematic of the disc 80
Fig. 47 – Blown-Up Schematic of the assembly for half symmetry test piece 80
Fig. 48 – Blown-Up Schematic of the assembly for quarter symmetry 81
Fig. 49 – Half Symmetry Mesh, overall view and view along the x-axis 82
Fig. 50 – Quarter Disc Mesh, overall view and view along the x-axis 83
Fig. 51 – a) DP800 Engineering MACH1 Data b) DP800 True Stress Strain 83
Fig. 52 – Boundary Conditions for the ShP Test Assembly 86
Fig. 53 – Cross section of Shear zone of Shear Punch Test. This shows development of von Mises stress and that peak stress is at the corners of the punch tip and lower die 89
Fig. 54 – Section of 3D assembly Shear Punch Test 89
Fig. 55 – Effects of mesh density in the shear zone on the output results of the 3D model of ShP test 90
Fig. 56 – a) Sample Disc at 15sec, b) Sample at 81sec this having failed. 91

Fig. 57 – Force deflection curve of 3D shear punch test, different modelling approaches compared with experimental testing..... 92
Fig. 58 – Difference of results from measuring displacement at the punch compared to the deflection measured at the bottom of the sample..... 94
Fig. 59 – Plastic Flow curves for ferrite and martensite 98
Fig. 60 – DP800 alloy with 30% Martensite content 99
Fig. 61 – Flow curves of ferrite and martensite phase used for the RVE micromechanical model with the material strength properties applied to different segments of the RVE 100
Fig. 62 – 2D RVE of real DP microstructure showing severe localised failure..... 101
Fig. 63 – Stress-Strain distribution with different meshes of 2D RVE of real microstructure 102
Fig. 64 – Randomly Generated 2D microstructure, discrete martensite phase distributed throughout..... 104
Fig. 65 – Free Body Diagram for the Representative Volume Element with boundary conditions applied..... 105
Fig. 66 – 2D RVE with all nodes paired along the edges and corners. 107
Fig. 67 – Simple 2D RVE with PBC applied, showing strain..... 108
Fig. 68 – Combined deformed RVEs showing a repeating mosaic pattern..... 109
Fig. 69 – Stress Distribution in 2D RVE of DP Steel, stresses concentrate in the martensite particles with ferrite that has undergone large local deformation also showing higher relative strain..... 110
Fig. 70 – 2D RVE with 30% Martensite content showing von Mises Stress and Plastic Equivalent Stress at the same time step..... 110
Fig. 71 – 2D RVEs Stress Strain curves with varying martensite Vm 112
Fig. 72 – 2D RVEs Stress Strain curves with varying martensite V_m 113
Fig. 73 – Maximum Stress vs Strain, Varying martensite content plotted against stresses and strain. Each dot represents the peak von Mises stress of a RVE with martensite Vm, with left to right having a higher to lower martensite concentration. 114

Fig. 74 – Failure along the shear strain bands in the RVE micromechanical model . 115
Fig. 75 – Failure of DP alloy due stress incompatibility at M-F grain boundary shows initiation of strain..... 117
Fig. 76 – Failure of DP alloy due stress incompatibility at M-F grain boundary shows ferrite elements that are no longer reinforcing the RVE shown in grey. Elements are not deleted but do not contribute to the strength of the RVE. 117
Fig. 77 – von Mises Stress A_1 to E1 and PEEQ A_2 to E_2 for 5% martensite content .. 119
Fig. 78 – von Mises Stress A_1 to E1 and PEEQ A_2 to E_2 with 20% martensite content 120
Fig. 79 – von Mises Stress A_1 to E1 and PEEQ A_2 to E_2 with 30% martensite content 121
Fig. 80 – 2D RVE showing the development of strain bands 45° relative to the loading direction. Martensite particles interrupt the growth of these strain bands, reinforcing the RVE..... 123
Fig. 81 – Cut at 50% along the z-axis showing the grains in the 3D RVE, green being martensite and red ferrite all generated in NEPER 126
Fig. 82 – 3D RVE tessellation having been meshed in NEPER 127
Fig. 83 – Meshed 3D RVE part imported into ABAQUS 128
Fig. 84 – 3D Tessellation generated in NEPER 128
Fig. 85 – Meshed tessellation that can be imported into Abaqus 129
Fig. 86 – Stress in Martensite in the 3D RVE 130
Fig. 87 – Stress in Ferrite in the 3D RVE 130
Fig. 88 – Plastic Equivalent Strain in the 3D RVE..... 131
Fig. 89 – Plastic Equivalent Stress Ferrite the 3D RVE 132

List of Tables

Table 1 - Mini1 and Mini2 tensile bar dimensions [11]..... 20
Table 2 - Composition for DP800 and DX57 provided by the Mach 1 lab in Swansea37
Table 3 - DX57 and DP800 Thicknesses 40

Table 4 - Variables in Parameter study going from lowest setting to highest, standard measures are highlighted in bold 45
Table 5 - DP800 properties 49
Table 6 - Shear and Converted von Mises Stress 70
Table 7 - DP800 Material Properties used from the axisymmetric modelling approach 84
Table 8 – Punch Displacement Rate 87
Table 9 – Elastic Properties for Ferrite and Martensite 97
Table 10 – Hardening Coefficients for DP800 *[118]* 97
Table 11 – DP800 Chemical composition from Mach 1 Lab at Swansea University . 98

Acknowledgements

I wish to express my immense gratitude at my supervisors Dr Will Harrison, Dr Didier Farrugia and Professor Djordje Peric for the support they have given me throughput. I want to give a mention of the patience and understanding that Dr Will Harrison gave me when personal circumstances got in the way and for not giving up on me. I will never be able to repay your support throughout this time.

The M2A Team who have acted as a support network by providing guidance throughout this process.

Tata Steel who have supported this project by coming on board as an industrial partner.

I also want to thank my family and friends who have been a continuous source of encouragement throughout this time in keeping me going when there were times it could have gone the other way.

This project has been supported by UKRI who provided funding to carry out this research project.

Nomenclature

E = Young's Modulus (MPa)

S = von Mises Stress (MPa)

σ = Stress (MPa)

V = Poisson's Ratio

ε = Strain

FLC = Forming Limit Curve

GLB = Global Formability Diagram

V_m = Volume Fraction (%)

A = Initial Yield Strength

B = Flow stress on hardening behaviour at quasi-static strain rate

n = Flow stress on hardening behaviour at quasi-static strain rate

C = Strain rate effect

ε^* = Material parameter below the transition temperature

T^{*m} = static yield stress

Small and Shear Punch Test

τ = Shear Stress (MPa)

F = Applied Force (N)

F_M = Maximum Applied Force (N)

d = Displacement (mm)

δ = Normalized Displacement (no units)

t = Specimen Thickness (mm)

r_{CT} = Corner Tip Radius (mm)

r_D = Die Radius (mm)

r_P = Punch Radius (mm)

c = Radial Clearance

RVE = Representative Volume Element

M-V% = Martensite Volume Fraction

F-M% = Ferrite Volume Fraction

1 Introduction

1.1 Motivation

Advances in the automotive industry have over the years resulted in improvements in many areas. Some of these include greater passenger safety, improved fuel efficiency and a higher recyclability content. These continue to be drivers of innovation within the industry, especially as legislation becomes stricter with performance targets being continually updated. These include the reduction of emissions from motor vehicles [1] from more robust testing procedures. A key factor in achieving these targets will be the development of new steel alloys used in the manufacture of vehicles. As such, car manufacturers are requiring more advanced steel from their suppliers. However, the development of new alloys is usually a time and resource intensive process requiring many iterations of prototype alloys. Many tests are required for any alloy to be homogenised, including yield tests, tensile tests, elongation tests, formability tests (Nakajima test) etc…, with the risk that customer specifications may not be met. New developments in how new alloys are developed is therefore a key requirement for manufacturers. One of the current research groups is Rapid Alloy Prototyping (RAP). This thesis is focusing on accelerating the development of prototype alloys through a combination of small batch production, computational modelling and data analysis to identify promising alloy combinations. This allows testing of hundreds prototype alloys in a relatively short amount of time. Promising chemistries are identified which can then put into trial runs before identifying the key prototype alloy.

A component of this is the use of small-scale mechanical tests such as punching of small metal discs. These can be used to obtain preliminary data and benchmark different prototype alloys. Through a combination of testing and computational modelling material data can be obtained which will help with the development of new alloys. The report will at first discuss the two small testing techniques investigated. These being the small punch and shear punch test. The shear punch is the current area of interest as there are currently more research opportunities. Many papers have already been written in establishing the small punch standard. The shear punch is a

comparatively new test, whilst similar does differentiate in some key areas. Next will be the modelling work that is currently being done. Modelling therefore is also required to track the development and evolution of damage on punch testing techniques.

Developing new grades of steel alloy is a costly and time-consuming process. The process is typically iterative with many different physical samples having to be produced for testing. This can run up to 100s of tonnes being manufactured when only a relatively small fraction of that is needed for assessment and certification. With new steel products becoming ever more complex due to the greater performance demands from customers, being able to quickly develop new grades of steel alloy will be a key factor for manufacturers to be competitive. New development pathways that quickly homologate novel alloy grades and brings them to market is needed to achieve this. Additionally, with ever more stringent emission regulations being enforced it is necessary to have a lower carbon intensity when developing and manufacturing new steel alloys. This is where Rapid Alloy Prototyping (RAP) presents new opportunities for novel steel development. RAP is a partnership between Tata Steel, MACH1 Swansea University, Warwick Manufacturing Group (WMG) and the EPSRC. The aim of the partnership is to adapt the high throughput approach with many small-scale samples prepared and tested. The properties are assessed and computationally modelled using novel image and simulation techniques.

1.2 Overview and Structure of the Thesis

Chapter 2 of the thesis begins with a literature review of RAP processes as a technique for how the development of novel steels is being done as well as the changes that need to be made in how material properties are obtained when using nonstandard sample volumes. The use of punch test techniques for testing material properties to screen many alloys when only small volumes of material are available. The use of finite element techniques are used to analyse deformation and damage with this type of procedure and the different scale sizes that FEM can be modelled. The chapter finally does an analysis of Dual Phase steels looking at the unique properties they possess and why they are an area of interest for researchers.

Chapter 3 describes the process of preparing samples that undergo shear punch testing. Evaluating the performance of two alloys with different strength characteristics and obtaining material properties of DP800 via this route to compare finite element models going forward.

Chapter 4 is a study of the set up of the shear punch test geometries. It aims to explore the key factors in set up the test required to achieve shear dominant deformation. Exploring how deformation happens within the material and where failure is happens in the test sample. This piece of work will examine many different tests with varying geometries and will use a simplified modelling approach to accelerate throughput of models and form a basis for future more complex modelling.

Chapter 5 builds on the work done in the simplified modelling approach performed after test parameters identified. It goes over the complexities of modelling punch tests in 3D as well difficulties in developing the right material damage and strain values. Concluding with the limitations in results generated from this line of research.

Chapter 6 explores microstructure modelling of dual phase steels and developing novel approaches to develop synthetic microstructures in 2D to evaluate characteristics of the microstructure which would be possible from either experimental testing or using real microstructures. It then also looks to apply these principals to 3D microstructures

Chapter 7 draws on the on the major academic conclusions and insights that were drawn from this body of work. It highlights the major academic conclusions that were drawn from the research around the testing of materials in shear punch testing, the parameter study done, 3D modelling and microstructure modelling.

Chapter 8 concludes with initial summary and proposes suggestions for future avenues of work that have been identified by this body of work.

2 Literature Review

2.1 Introduction

This project is scoped around improving the understanding of punch testing techniques used for the development of prototype steel alloys. Though the project focuses on the modelling of these tests, this section serves as background knowledge to the development of steel alloys and the novel work being done in this area. The project investigates the feasibility of using small scale tests for evaluating material properties via a modelling route and ultimately determine if these tests can generate material properties which allows for the identification of promising alloy grades and ultimately speed up the development of new steel alloys.

2.2 Steel Prototyping and Small Scale Manufacturing & Testing

For development of new alloy grades such as in the steel industry typical prototype samples range mass between 25-60kg. This is usually done by Vacuum Induction Melting (VIM) casting. In VIM casting a material of a single composition is cast, this followed by various through-processing and downstream techniques to simulate a finished cold annealed rolled and coated steel. These processes include hot and/or cold rolling deformation, and heat treatments applied to the alloy. Final steps then include sample machining and preparation before it is ready for testing. This process has allowed for the optimisation of existing grades and facilitated development of new alloy grades prior to launch and implementation. Historically this kind of incremental approach via trial and error has produced reliable data of mechanical properties of new alloy grades [2,3]. However, this process is time inefficient as it requires many samples differing composition for analysis to obtain mechanical data. To accelerate the development of new alloy grades, smaller scale manufacturing and testing is needed for streamlining development, application and development of new alloy grades. Traditional development routes are limited in this regard and act as a limiter in competitiveness for manufacturers to bring new products to market. New methods to more rapidly produce and therefore efficiently develop new alloy grades is required.

Ideally, this would be where a large sample set of varying alloy content is produced using the same or less starting material volume and identify alloy compositions that have the most desired mechanical properties. This would allow early sifting in the development cycle of the most promising alloys for further analysis. This would be a Rapid Alloy Prototyping (RAP) process and speed up the development of new alloy grades. This type of approach gained interest by other researchers [4,5], Kada et al. used additive manufacturing techniques to produce NI-Co alloys for development of scratch resistant alloys. In [6] a modified RAP process was used to screen multiple compositions of different alloying elements of an Invar alloy (an alloy grade with a low coefficient of thermal expansion) against a master alloy to identify promising multicomponent multi-functional alloys. In [7], a rapid prototyping approach is by combining physical modelling to optimize metal extrusion and bonding, and additive manufacturing techniques in aluminium alloys using plastic samples. In [8], additive manufacturing of aluminium alloy as a RAP route was used to quickly develop metal parts and investigate its microstructure. Many of these papers refer to RAP as a novel manufacturing technique for the development of metal parts. However, the term RAP is used differently by these different authors showing that it is still an ongoing area of research and development. In this thesis RAP [9,10] refers to an approach that accelerates the development of new alloys by combining novel downsized manufacturing techniques with small scale testing and modelling. What follows is a description of the RAP routes for producing small quantities of prototype material.

2.2.1 RAP 20-40g

This route primarily uses powder manufacturing, this involves powder selection, weighing, compaction to reduce porosity and followed by induction melting to develop cylindrical ingots. The upper 40g route allows for more reproductivity of composition, to have more material available in one melt to recreate the wider range of processing techniques involved and have more material available for testing after composition analysis. This route will not completely be able to match the standard 30-60kg VIM laboratory route. As such, not all of the benefits that the RAP20-40g presents can be used to develop an end product or validated by miniaturised testing such as mini-tensile or punch tests. The benefits that do present themselves are testing of

composition microstructures, and the effects of residual elements, which can be determined faster and earlier on during the development cycle. Compared to the standard VIM route more sample can be prepared and compared, with an expected throughput that is 20 higher when manufacturing [9] the same number of test specimen. However, this is dependent on reliable production of samples that pass quality assurances. A final benefit is the lower up front capital investment needed to get this process route started as it has a lower special requirement and can be set up in parallel with other processing techniques to increase the throughput of samples.

2.2.2 RAP 200g

The RAP 200g route is the intermediate scale manufacturing route being developed within the Prosperity Partnership . This route uses either solid or pellet alloy material followed by induction melting and centrifugal casting in argon to produce ingots of up to 200g. This process allows for steel sheets of up to 300mm length in a variety of widths. This permits accommodation for various tensile test designs including industry standard ASTM A80 [11], ready for release of production material. The RAP 200g route has the addition of centrifugal casting and a mini hot mill included in the manufacturing process [9,10]. Additionally, thermo-mechanical simulators can be used to provide thermal-mechanical-microstructure data as a method to shorten the design process. The main benefit of this intermediate scale route is the combination of throughput speed and length scale for feedstock to be cast and hit rolled in a miniature mill to simulate downstream processes. This process is still being refined to develop optimum microstructures to replicate standard manufacturing processes.

The RAP 200g and RAP 20-40g process routes are the main source of sample material for the testing performed on the miniaturised tests, those being mini tensile tests and punch tests (Small Punch and Shear Punch). As described, the objective of these new process routes is to bridge the gap between laboratory manufacturing methods and the industry standard development routes of new steel alloys up to 30kg. Work still needs to be done to optimise these lines to produce samples in consistent and replicable manners, which will include optimisation of melting and annealing, particularly for multi-step processes such as those used in manufacturing of DP alloy and replication also needs to be established with the miniaturised test techniques [9].

2.2.3 RAP 4.5kg

This route is closest to the more traditional laboratory manufacturing processes with hot and cold milling, furnaces for annealing and continuous annealing processes to impart homogenous cooling to create an improved surface state. It is still considered a RAP route as is it capable of developing and processing novel compositions within 2 two weeks, this includes machining of samples for tensile testing.

2.3 Small Punch Testing

2.3.1 History and Background

The Small Punch (SP) test is a procedure that was first developed during the 1980s in the US and Japanese nuclear industries [12]. This came out of a need to assess the performance of in-service materials of operational nuclear reactors. These include structural components of buildings that house reactors, pressure vessels and pipes. The risks to worker safety from high level radiation exposure and not compromising the structural integrity of key components required the development of new test techniques. This came from the challenge of obtaining sufficient material for at the time standard techniques. These challenges from obtaining enough material for assessment purposes led to the developing of new tests for assessing key material properties. Particularly that of steels which are exposed to elevated levels of free hydrogen leading to alloy embrittlement. Where knowing the life cycle evolution of material properties is needed, particularly for validating the safety of sites. This resulted in the creation of the SP test which has since developed as one of the assessment tools used within the global nuclear industry with much work having gone into standardized test procedures and assessment of results. Particularly for looking at particular properties like Yield Strength (σ_Y), Ultimate Strength (UTS) and Elasticity (ε). Since then it has gained interest in other industries where only laboratory quantities of test metals are produced [13], testing many different metal alloys and for testing of metals that may have local heat affected zones such as from spot welds [14]. The SP test has also gained interest in other research areas that focus on the development of new alloys. The benefit being able to downsize the volumes of material required for assessing material properties of prototype alloys.

2.3.2 Test Set-Up

The main components of the SP test consist of the sample disc, also called a test piece or specimen, dimensions of 0.5mm thickness (t) and 8mm diameter. An upper die and lower die are used for holding the sample in place. The most common geometries for the lower die are receiver hole diameter of 4mm. To this a 45° chamfer with an edge length of 0.2mm. The upper die is used to hold the disc place preventing any sliding. The punch head has a diameter of 2.5mm using either a hemispherical head that is fixed to the punch or a metal sphere with an equivalent diameter that can move freely, a typical setup with a fixed hemispherical punch head is shown in **Fig. 1**. Different drawbacks and benefits have been commented by various authors [15–17]. The benefit of using a sphere is the ease at which it can be replaced once there is excessive wear. Unlike the hemispherical punch head where with repeated use parts can get worn impacting the force deflection curves. The primary drawback of the spherical approach is the free movement that may occur during a test run. With the tight tolerances ±1% that exist in this setup, it necessary to ensure that proper central alignment us achieved [15,16]. It has been proposed that a groove can be used in the punch to ensure alignment of the sphere. Overall, there is no single consensus on which a more optimum approach for either setup with both having been used to generate reliable results [18,19].

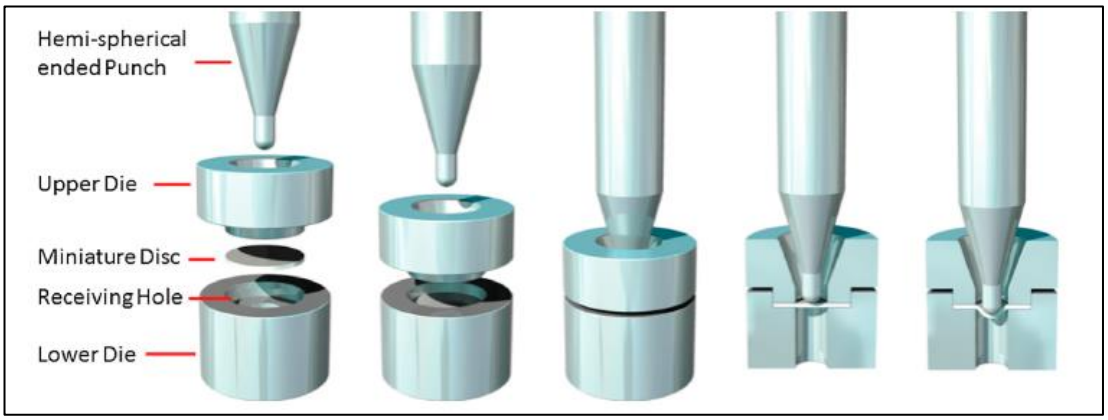

Fig. 1 – Typical setup of a SP test [24]

Punch displacement rate has been an area with greater amounts of variation between authors. With velocities ranging from 0.3mm/min [20] to 1mm/min [21]. In all cases the punch is driven against the test piece at a constant displacement rate. The main

results recorded from the SP test are the measured punch force (F) required to push through the test piece as a function of either the punch displacement (v) or sample deflection (u) measured at the bottom of the test piece. This is different to the Small Punch Creep (SPC) test where a constant load is applied onto the test piece and displacement is measured as a function of time. These tests have been used to assess the fatigue strength of materials rather than the yield and ultimate strength of materials.

A code of practice [22] was developed in 2006, this document is based on the work performed by multiple researchers over several years and provides a best practice guidance on test setup and procedure. This test procedure is different to the Erichsen Test in size of the samples being tested and geometries employed for the punch head. Whereas in the SP test sample thickness is 0.5mm and the punch head has a 2.5mm diameter, in the Erichsen test the sample has a 1.5mm thickness and the punch a 20mm diameter [23]. Additionally, the Erichsen test is used to determine the ductility of a sheet metal whereas SP testing is used to determine the tensile strength of a metal by empirical correlations.

Multiple authors have commented on the compliance of the test setup [15–18,25–29]. This is the small amounts of deflection in the clamping components or punch due to the resistance of the test piece and delays in in the measured force and deflection [24,30]. Due to the small size of the test piece and displacement of the punch, even a small amount of compliance in the test rig has significant impacts on the accuracy on the SP test. Therefore, it is preferred to measure the deflection at the bottom of the test piece rather than the punch displacement. Furthermore, in the later stages as the test piece approaches failure, a thickness reduction occurs before rupture. This creates a further divergence in results between deflection and displacement.

2.3.3 Outputs

Fig. 2 shows the plot of a typical SPT curve for a ductile metallic alloy with the plot divided into 4 zones [30]. Zone 1 is the elastic bending of the test piece and the indentation on the top surface of the test piece caused by contact from the punch. Zone 2 is the plastic bending spreading through the deformation zone to rest of the test piece. Zone 3 is the onset of membrane stretching and hardening of the test piece. Zone 4 is

the point at which peak load is reached and where the onset of plastic instability begins. As slope of the curve decreases failure mechanisms develop, including necking and the development of visible cracks until failure. F_e corresponds to the load at which the yield strength (Y_S) has been reached. F_m is the ultimate load of the punch and corresponds to the ultimate tensile strength (UTS). E_{TO} is the total energy required to deform the sample until failure being the area under the curve.

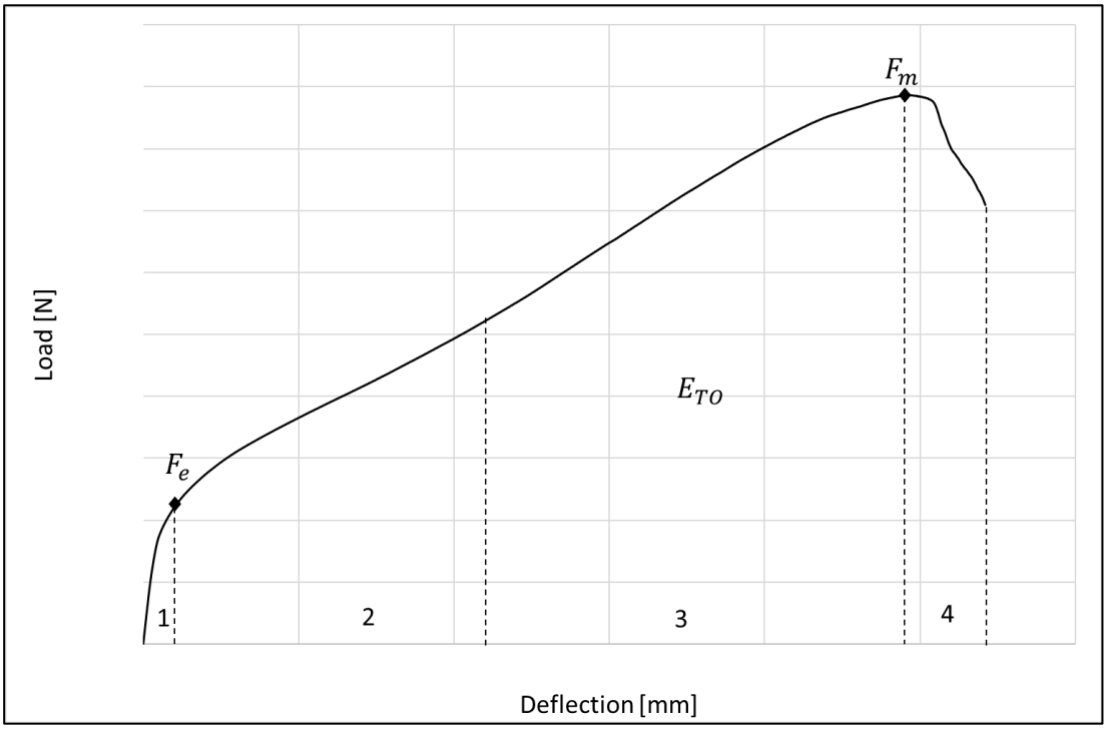

Fig. 2 – SPT Load-Deflection curve of a ductile metallic alloy

2.4 Obtaining Material properties

Direct Yield and Ultimate strengths cannot be obtained from SP tests as they would be in tensile tests. Conversions must be applied to the punch load outputs, these have typically involved the initial specimen thickness as well as the use of empirical constants for a given material.

The empirical equation to obtain Y_S is given by [31–34]:

$$\mathbf{Y_S = \alpha_1 + \frac{F_e}{t^2} + \alpha_2} \quad \textbf{(1)}$$

F_e is the load at which the specimen transitions from the linear relationship in zone 1 to zone 2 and is agreed among researchers as being the point at which the yield strength has been reached. t is the initial thickness of the test piece and both α_1 and α_2 are test constants. However, different methods have been proposed of estimating at which point along the SPT curve the transition has been reached. One method [35] defines this point as being the crossing point of two tangents in zone 1 and zone 2. The CEN code of practice modifies this slightly as being a vertical point of the crossing point of the two tangents along the test curve. Other authors [36] have used a standard offset defined as being t/10 parallel to the slope in the elastic region.

Two expressions have been proposed to obtain UTS in [32,33,37]:

$$\mathbf{UTS} = \boldsymbol{\beta_1} + \frac{\mathbf{F_m}}{\mathbf{t^2}} + \boldsymbol{\beta_2} \tag{2}$$

$$\mathbf{UTS} = \boldsymbol{\beta_1} + \frac{\mathbf{F_m}}{\mathbf{t} \cdot \boldsymbol{d_m}} + \boldsymbol{\beta_2} \tag{3}$$

The method for obtaining the UTS was to divide the peak load by the square of the initial thickness. Different authors [32,38,39] have observed that the UTS is dependent on the deflection of the specimen at the maximum punch load. Dividing the peak load by the product of the initial thickness and the deflection at that maximum load. As the deflection is during a SP test, in the region of 1.5mm-2.2mm [15,16,29]. Significantly higher than what would be expected in a standard tensile test.

2.4.1 Tolerances

As highlighted in the SP test, tight tolerances are required when setting up, performing, and measuring each individual test. The CEN [22] specifies a 1% accuracy in the measurement of the of the thickness of test piece at five locations, one in the centre and 4 at the edges rotating 90° degrees each time. For the 0.5mm thick sample, this requires measuring ±0.005mm This level of accuracy can be achieved with some micrometers such the Mitutoyo MDH Micrometer Digimatic ABSLUTE which has a stated 0.1μm (0.001mm) resolution measurement. The same 1% accuracy of the disc thickness is required for the measuring of the deflection/displacement.

2.5 Shear Punch Testing

The Shear Punch (ShP) test is an evolution from the SP test where the key differences are the use of a flat ended punch rather than a hemispherical punch use in SP testing [40] and the geometric changes made to have shear dominant deformation in the former [30]. It too is a technique that allows for the testing of small amounts of metallic material. This is of advantage when developing new steel alloys where only limited quantities are available. This has created interest in the ShP test as a relatively large number of tests can be performed using small quantities of material. The ShP test rig consists of four main components shown in **Fig. 3**, being the sample disc (specimen), an upper and lower clamp, and a flat ended punch. Whilst ShP testing is more established with working groups having concluded what standards should be used for testing [16].

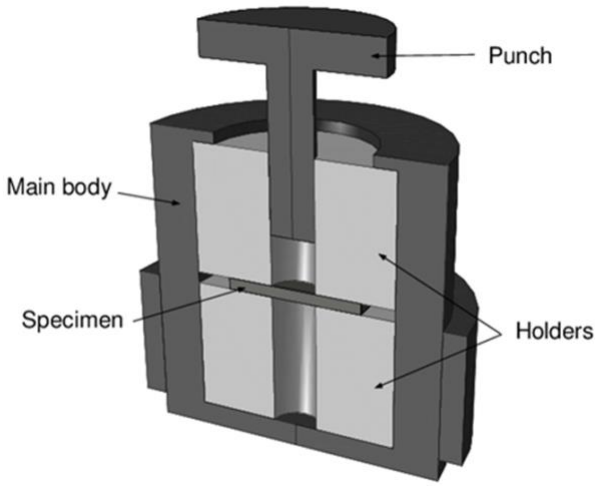

Fig. 3 – Shear Punch Test setup [41]

A 2D schematic of the ShP test with dimensions in mm in shown in **Fig. 4** below. This additionally shows the dimension for the radial clearance in the setup, highlighting the small distances use.

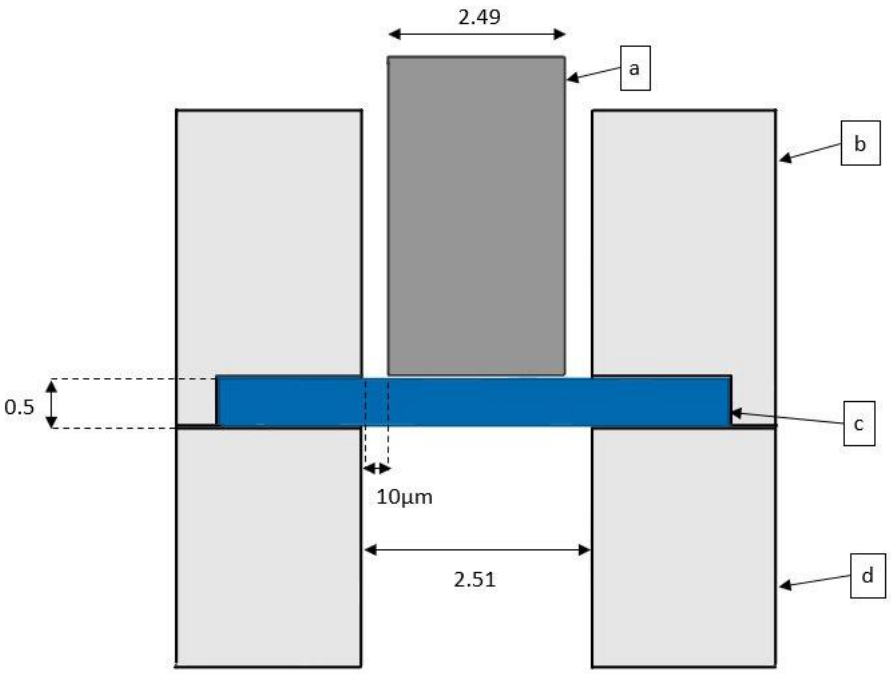

Fig. 4 – Schematic of the Shear Punch rig (in mm) with dimensions shown. a) punch, b) top holder, c) sample disc, & d) lower die

A specimen shaped into a small disc is clamped in place between an upper and a lower die to prevent sliding or any other movement. A flat ended punch pushes against the test piece at a constant displacement rate causing a shear dominant deformation of the test piece. Key setup parameters of the ShP test are the punch radius, the radial clearance (dependant on the punch a lower die radius), the specimen thickness, the radius of the lower bore, the punch corner radius and the corner radius of the lower die. The outputs obtained from the ShP test are Punch Load and Punch Displacement which are ultimately used determine the tensile properties of the test alloy using empirical corelations. The Punch load is converted into the shear stress using the following equation this has been derived by multiple authors [41–44]:

$$\tau = \frac{P}{2\pi r_{avg} t} \quad (4)$$

Where P is punch load, t is specimen thickness and r_{avg} is the average radii of the punch and the lower die receiving hole. This is method for determining the shear stress is widely used [43–45]. There are however differences in how the displacement data is changed to use either radial clearance or the sample thickness. The first method is converting the punch displacement into shear strain γ with the following equation:

$$\boldsymbol{\gamma = \frac{d_c}{c}} \tag{5}$$

Where d_c is the punch displacement and c is the radial clearance. This method has been used by [46,47]. However, it has been observed that the specimen thickness has an impact on the output of the ShP test, with increasing thickness resulting in an increasing punch load for a given displacement. The effects of specimen thickness and radial clearance were investigated in [48]. Which proposed an alternative conversion for the punch displacement using:

$$\boldsymbol{\delta = \frac{d_c}{t}} \tag{6}$$

Using specimen thickness (t). They were able determine a method for determining the shear yield strength (τ_{ys}) that is thickness independent. This method has also been used by [49,50]. The normalized displacement for this research is favoured when examining the ShP test, but both shear strain and normalized displacement will be compared in the simulation results.

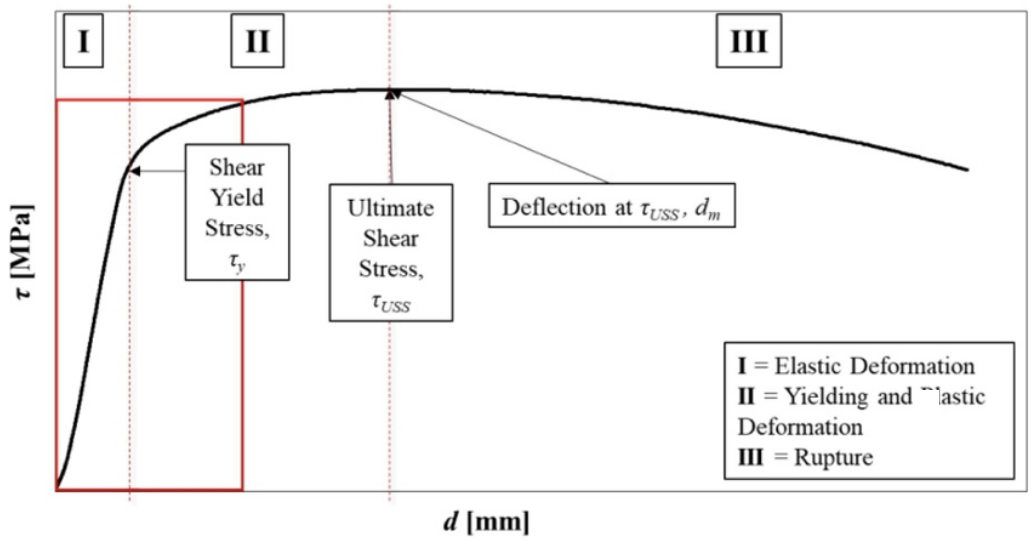

Fig. 5 – Schematic of the Shear Punch Test Output [51]

Fig. 5 shows the typical load distribution for the ShP test carried out at Swansea University and was provided for this thesis. As there is no standardized method for setting up the ShP test rig. There are differences in how researchers performed their experimental setups and interpret the ShP test curve. A variety in specimen diameters is used ranging from 4mm to 10mm and thickness in the range of 0.48mm to 0.8mm [46,47,50,52–54]. With varying setups in the punch and lower bore diameter varying from a low combination of $\emptyset = 1.59\text{mm}$ and $\emptyset = 1.61\text{mm}$ [53] respectively with higher values for punch $\emptyset = 3.00\text{mm}$ and lower die $\emptyset = 3.04\text{mm}$ [49]. When reviewing the radial clearances, again a variety of values are used with 10µm [53], 15µm [50], 20µm [49], 25µm [46,52], 50µm [54] and a high value of 125µm [47]. With regards to some of the smaller clearance values used is the repeatability of the setups. Given that typical machining cutting tolerances for Computer Numerical Control (CNC) is ±0.005mm or 5µm [55]. The method for manufacturing parts of the test rig and the repeatability of these manufacturing techniques must be considered for the outputs to be considered valid. Another parameter is the speed of the punch as it drives down against the punch, due to the low thicknesses on the disc impact forces want to be reduced to ensure that loading rates are applied consistently throughout the test procedure. Typical punch speeds vary between 0.1mm/min [50] to 0.25mm/min [47,53]. The criterion for determining the speed is to have an equivalent strain rate as would be found in a standard tensile test. For a 0.5mm thick specimen with a punch

speed of 0.25mm/min, this results in a strain rate of 0.008/sec. Determination of the shear yield point is done via a linear offset method relative to the test piece thickness *t* that is 100th its initial thickness, this is shown in **Fig. 6** below.

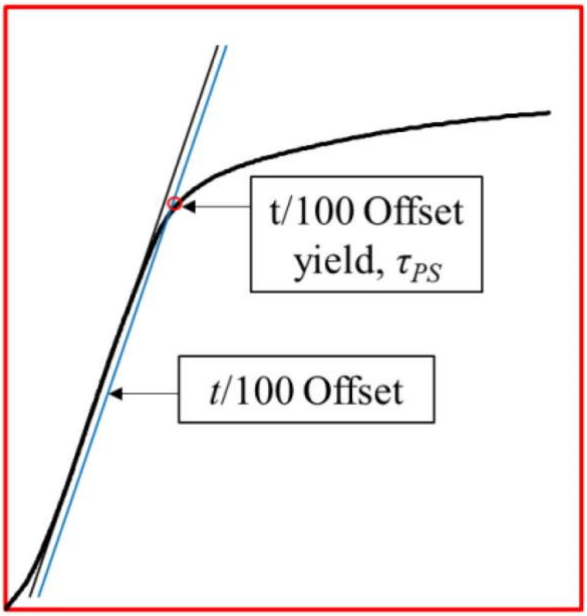

Fig. 6 – Offset methodology for determining yield load for ShP test [51]

The ShP test data is, once converted to Shear Stress-Normalized Displacement, used to determine the tensile yield stress for a tested material. Empirical correlations have been [40,44] developed that relate the shear stress (τ) to an equivalent tensile stress (σ):

$$\boldsymbol{\sigma = 1.77\tau} \tag{7}$$

This equation was proposed by Guduru [53] and is value is close to the von Mises criterion for pure shear stress of [45]:

$$\boldsymbol{\tau = \frac{\sigma}{\sqrt{3}}} \tag{8}$$

The von Mises criterion works best for polycrystalline materials provided that the deformation is shear dominant during the testing process. The 1.77 value (slightly

higher than the $\sqrt{3} \approx 1.73$) suggests that that whilst the deformation is shear dominant, other deformation processes are occurring. These include bending and compression.

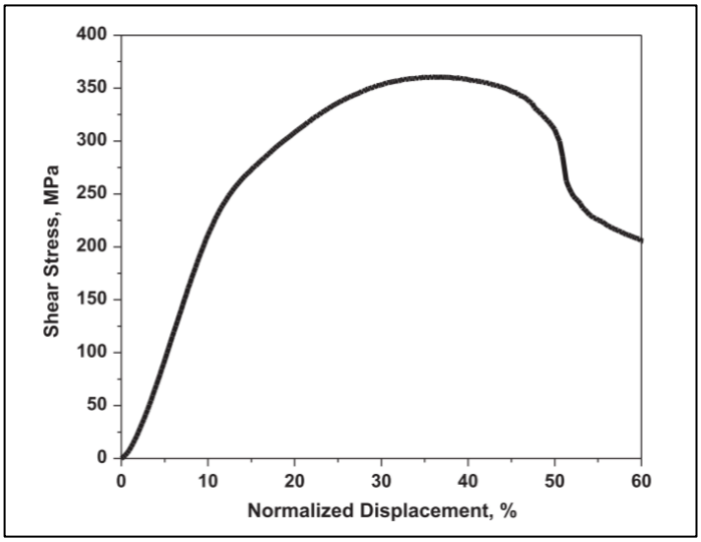

Fig. 7 – Typical ShP Test curve with Shear Stress-Normalized Displacement [50]

A final Shear Stress Stress-Normalized Displacement curve is shown **Fig. 7** above, this shows the typical output for a ShP test of a metallic material. Several researchers in ShP test have commented in the compliance effects from the test rig setup. This is because the test rig will not be completely rigid, during the experimental procedure causing some deflection of the punch and clamping surfaces. However, in FEM modelling the analytical surfaces are completely rigid and will not deform resulting in a steeper elastic region than in experimental setups. Due to this, a 0.15% offset of normalized displacement is proposed by Guduru et al [43] whereas a 1% offset of normalized displacement is used in the experimental setup by several other researchers [48–50,53]. Finally, whilst the ShP has been used to validate strength properties from known alloys by means of conversion from shear stress to an equivalent tensile strength. Comparatively little work has been done for the ShP test as a means to support the development of new high performance steel alloys, particularly as means in the RAP route.

2.6 Nakajima Test

The procedures described for SP and ShP tests, where a metal disc is clamped in place has a spherical or flat-ended punch driven against it respectively have some similarities

to the Nakajima test. Nakajima also uses metal discs and have a hemispherical punch driven against it until failure occurs. Where is SP and ShP tests the discs have a typical diameter if 5mm [16,25,56–58], in Nakajima the discs have a typical diameter of 245mm [59–61]. Meaning that larger geometries are used. The Nakajima test is used to characterise sheet metal during forming processes. This is of particular relevance for applications where deep drawing of structural components is used [59], such as in the automotive sector where high strength-to-weight ratios are wanted [61] where there are non-linear strain paths in a drawbed [62]. Knowing how much a given metal can be drawn without cracking is key when developing parts. The concept of sheet metal forming limits was first introduced in the 1960s by Keeler [63] which developed into the Forming Limit Curve (FLC). The FLC expressed in major and minor strains, is one of the widest used methods for determining the forming limit of a sheet metal during modelling and design stages. The FLC is the point at which localised thinning initiates in a metal sheet during the forming process and leads to splitting, a typical FLC for DP800 is shown in **Fig. 8**.

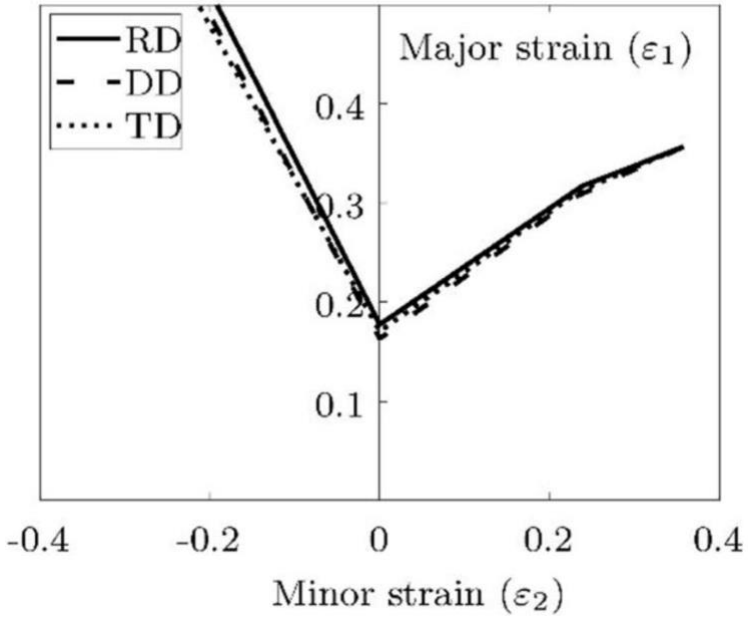

Fig. 8 – Forming Limit Curve for DP800 [61]

The two key identified differences of the SP and ShP versus the Nakajima test are; 1) SP and ShP use smaller geometries, particularly in the radius of the disc giving them smaller aspect ratios compared to Nakajima test. In SP and ShP the samples have a

thickness of 0.5mm and diameter of 5mm, with Nakajima samples usually having a thickness of 2mm and diameter of 245mm for biaxial condition or full Nakajima specimen [59,60]. As an expression of thickness to width ratio this would be a 2/20 vs a 2/245 for SP ShP tests and Nakajima tests respectively. And 2) the former used a means to determine yield and ultimate strengths of an alloy, whereas the latter is a forming test that allows for analysis of stretching in different stress conditions [60] and determine FLC of a metal sheet. While there are some surface similarities between the tests in terms of setup and procedures, the outputs of the tests are different and can therefore not be directly compared.

2.7 Small Scale Tensile Tests

One of the other issues that arises from the RAP [9] process is the small volumes of material produced by the nature of this downscaling. This means that standard tensile tests such as ISO/EN A80 cannot be performed as it is too large to be extracted from a strip of material produced by the smaller end RAP processes. Therefore, non-standard Miniaturised Tensile Specimens (MTS) need to be used for these routes. The questions that arise from non-standard MTS is the replicability of yield strength, tensile strength and uniform elongation values compared to traditional. Additionally size effects need to be considered when extrapolating results from these miniaturised tensile tests. With further reductions in specimen dimensions to less than 10 times average grain size [64], results from these tensile can no longer be considered representative of the bulk material properties.

2.7.1 Miniaturized Tensile Bar Tests

Zhang et al. [64] investigated the suitability of small-scale tensile tests for characterization of mechanical properties of DP600 and DP800 steels using RAP process routes. For this they generated small scale tensile bars called Mini1 and Mini2. The areas of interest in their investigation was the measurements of ductility, forming limits and r-values when compared to standard tensile tests. These miniaturised tests were compared with standard ISO/EN A80, ISO/EN A50 and ASTM25 tensile test techniques. The dimensions for the Min1 and Mini2 tests are shown in **Table. 1**, L_t, L_e, L_o, b_o, R and a_0 denote the total length of the test piece, parallel length, gauge

length, original width of the parallel length of the flat test piece, the shoulder radius and the thickness of the bar respectively with location of measurements taken shown in **Fig. 9**.

Table 1 - Mini1 and Mini2 tensile bar dimensions [11]

	L_t (mm)	L_e (mm)	L_o (mm)	b_o (mm)	R	L_0/L_c	L_o/b_0	$(L_c-2b_o)/L_0$	a_0 (mm)	K
Mini1	60	12.5	10	3	3	0.8	3.33	0.65	1.2	5.27
Mini2	41	9	5	2	1.5	0.56	2.5	1	1.2	3.23

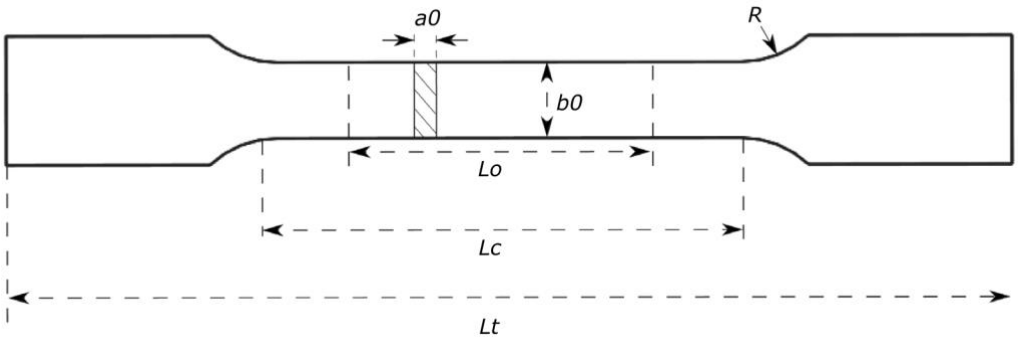

Fig. 9 – Definition of L_t, L_c, L_0, a_0, b_o and R in **Table 1** from [11]

In their study they aimed to answer the following questions that relate to the scalability of these miniaturized tensile test techniques using the Bertella-Oliver equation. The Bertella-Oliver equation is an ISO standard scaling law to evaluate the effects of different specimen geometries on tensile elongation and the cross-sectional reduction [65]. The questions their study aimed to answer were: 1) Is the Bertella-Oliver [66] equation valid for thin strip steels of less than 2mm and a tensile strength of more 700MPa, such as DP alloy grades?, 2) If the Bertella-Oliver equation is valid for DP steel, what are the specific elongation values and material constants?, and 3) How accurate are non-standard MTS in measuring the elongation and formability properties for materials produced via the RAP process route. Their conclusions were that the Bertella-Oliver equation can be used for specimens with a sheet thickness less than the critical value of 4mm and that specific elongation values remained constant but that test-piece orientation for higher strength, lower ductility DP800 had a greater impact

compared to DP600. Suggesting that anisotropy of the steel plays a greater role in these smaller geometries for DP800 versus DP600.

2.8 Finite Element Method

2.8.1 What is the Finite Element Method?

In engineering there are many complex problems where understanding the properties of a system is necessary. This may be understanding how a building behaves under different loading conditions, the flow of fluids through a pipe, the thermal conductivity for fire safety applications, or electrical conductivity in circuits [67–70]. Today, many of these problems are so large that they cannot be done without the aid of simplification and the of computational methods. Additionally, in a complex a structural problem it would not be possible to find an exact analytical solution as the number of degrees of freedom that need to be solved for are too many to be done either by either humans or modern computers. This particularly true for complex physical phenomena where there are geometrical and material non-linearities [71]. What the Finite Element Method (FEM) does is convert a large problem for which large partial differential equations would be needed and reduce it smaller algebraic ones where an approximate solution can be found. The reduction is done by breaking the problem into many smaller ‘elements’, this process called discretisation [72].

Instead of one large exact complex numerical solution the problem is broken down into many discrete problems that have known simple mechanical formulas. The Finite Element Method (FEM) is such a technique that can numerically solve complex structural mathematical problem by discretising a structure into many individual components, finite elements. This allows structural problems to be solved relatively quickly whilst maintaining a high level of accuracy [73].

The first step in a FEM model is defining the component geometries as these form the foundation of accurate analysis. These need to be able to accurately replicate the loading paths and deformation that occur in the test that is being simulated [74]. This often involves simplification of some components parts to reduce the computational requirements. In cases where is symmetry in either the deformable part or in the

loading directions, it may be possible to further simplify the model by cutting the deformable part and applying symmetry boundary conditions.

The deformable parts are then discretized into a mesh using N_e element and N_n nodes. The number of elements and nodes will depend on 1) the element edge length (L_e), 2) the size of the part being meshed, and 3) any areas where a higher mesh density has been applied.

Abaqus [75] is a widely used FEM software tool used for the modelling of deformation of complex systems to aid in design work and understand how objects deform particularly in punch testing. Whilst other commercially available software packages use similar principle, this project primarily uses Abaqus for the design of parts and exclusively for modelling the deformation.

2.8.2 Implicit vs Explicit Time Integration

For the ShP tests two modelling approaches can be considered for 3D analysis, those being "implicit" and "explicit" analysis. As the modelling of such tests is highly non-linear in the shear zone of the test piece an analysis cannot be performed in a single step [76]. The simulation must iterate through many steps as the elements undergo displacement and the evolution of their stress responses calculated. Displacement steps must be added that break down the physics/time relationship into many smaller parts to solve the problem. Which approach is better can broadly based on if the transient loading conditions though the structure must be considered for solving the problem. If the effects of an applied load to a structure are considered to act immediately the problem is time-independent, such as in static loading or slowly applied loads. A problem is time-dependant if the acceleration effects of the applied load must be considered for the solution, such a drop test. Hence which type of loading is modelled on a structure will determine what type of analysis should be done. Where there is a smooth non-linear problem, implicit analysis is generally more efficient. In high-speed dynamic analysis, explicit solvers are the more efficient solution to solving the problem. However, there is some overlap in "Quasi-Static" ($\sum F \approx 0$) where either can be used and the best approach will become problem specific. Such as where problems

have complex contact interactions or have large deformations, there may be issues with convergence resulting in a large number of iterations.

In the explicit scheme values at a time t are used to obtained dynamic quantities at $t + \Delta t$. With the central difference operator only being conditionally stable. As explicit accounts for the finite propagation speed (speed of sound through a given material) of a dynamic analysis. The stability limit is dependent on the time needed for an elastic wave travelling across the smallest element dimension in the model. Therefore, the time step is limited by the smallest element in the whole model and the global average element size, limiting the upper bound time step available for a simulation. This therefore requires a mesh that is fine enough to represent the spatial effects and the time steps need to be in the same order of magnitude as the transit time from one element edge to the other. This means that each step increment is small with many (over 1million, problem size dependant) increments needed to complete a simulation. Implicit schemes can overcome the time step boundary by solving the dynamic quantities not only at time t but up to 2 orders of magnitude greater than that of an equivalent explicit scheme. However, as the time step Δt increases relative to the total time T, a deterioration in the response prediction will occur. This is because for implicit analysis, the propagation effects are controlled by the part mass inertia and not the elastic wave speeds (load effects being applied immediately to the entire structure) [77]. This also means that the mesh in an implicit analysis does not to be as refined compared to an equivalent explicit analysis [75]. Having only to capture the overall deformation of the structure and the time steps to be small enough to capture the spectrum of the deformation response desired. This can be specified in the Field Output request having output data points at every n^{th} time step or step increment. For larger models where many time steps will not be necessary to capture an output at every increment. In the implicit scheme, all non-linear equations must be solved before the next step can begin as these will be used input for calculations in the following dynamic quantities at $t + \Delta t$ [76]. The relative economy of each modelling approach will be dependent on factors that are problem specific based on the prescribed loading scenarios. Such as the stability time limit in explicit analysis, the size of the model (how many elements does the structure have), how big of a time step can be used in

the implicit analysis and how quickly the non-linear equations can be solved. The non-linear equations will come in 3 forms; Material Non-Linearity (present in the current modelling), Geometric Non-Linearity (not a main concern) and the Boundary Conditions such as those from contact. In simulations with large numbers of elements and complex damage mechanisms means these considerations are more relevant to 3D modelling rather than 2D modelling where the smaller computational requirements means that this does not need to be considered to the same extent.

2.8.3 FEM in Punch Testing

Due to the complexity of both SP and ShP testing with many deformation mechanisms happening during a loading test, FEM has been identified as a key tool for understanding these tests [43,58]. The main issue with punch testing techniques is the understanding of load paths that occur during deformation [43,78,79]. It worth seeing what has been done in standard tensile tests and where its differences mean that typical evaluation of load paths is not possible. In tensile tests it is possible to perform tests in-situ, that is performing tests while observing the material under a microscope. It therefore possible to see how the specimen is deforming at both the macro- and microscale. Making it possible to how grains deform, where voids form and how the sample fails [80–83]. This is typically done with interrupted tensile tests and can be view under Scanning Electron Microscope (SEM). For metals this typically done using Electron Backscatter Diffraction (EBSD) as it allows analysis of the microstructure of crystalline materials. EBSD technique works by moving a probe that emits a series of electron over a grid area. These electrons interact with the surface of the crystalline material and scatter. A detector collects a sample of these electrons and forms a backscatter diffraction pattern [84–86]. For both SP and ShP tests the sample encased in a holder, making it not possible to view what is happening to the disc during deformation, only after failure has occurred. Additionally, in ShP the area of interest is confined to a central area. This requires cutting of the sample along its though thickness to analyse the sample. Therefore, FEM has been a tool that has seen widespread use in punch testing [26,28,30,34,87–91] showing the validity this approach has at the macroscale and is often coupled to experimental testing to obtain reliable mechanical data from samples. This is done by comparing experimental results

with those obtained from FEM simulations but typically requires advanced material models and optimization techniques for effective results [92].

Whilst FEM is widely used for the obtaining of mechanical data in SP testing, namely yield strength, ultimate tensile strength and elongation on ductile materials with established methods used. There has been less work done with ShP testing. This is in part due the relative novelty of this technique in comparison to the SP test technique, the complexity of accurately modelling deformation over such a narrow area (particularly in the narrow shear zone) and the relative lack of a standard for testing geometries used. Therefore, the modelling of ShP tests has limited the focus to the geometries and setup of the parameters [44]. During the punch testing multiple deformation mechanisms occur within the test piece as the punch is driven down. These include tension, bending, compression as well as the dominant shear deformation desired from the ShP test process. As such it is not sufficient to only examine data from experimental results to analyse the stresses that occur within the shear zone of the specimen as these cannot be examined in real time and see how stresses initiate and evolve.

It has been reported in literature that test piece thickness affects the output parameters of the ShP test [32,40,45]. For a given punch load, displacement, and average radius for the punch & lower die; the shear stress and normalized displacement will decrease and test piece thickness increases. Due to the test pieces being relatively thin (0.5mm), controlling the effective thickness is a key parameter when performing experimental testing. In the CEN/ASTM [93] test method for metallic materials undergoing SP testing, the allowable tolerances are ±1% deviation of the specimen thickness, measured at 5 points on the disc, one centre and 4 on the edges. As test piece thickness is accounted for in the shear stress and normalized displacement, it would suggest that when known it should not have a significant impact. However, if the manufacturing tolerance are either outside of the permitted variation or are not accounted for when analysing the outputs. Understanding what impact this has on the punch load and shear stress outputs is of interest for future preparation of specimens for ShP testing as part of RAP.

The impact of friction has not been widely investigated in many research papers, with the focus being on creating a model that closely represents experimental setups [27,40,43]. When contact surfaces interact with each other, there will be friction between the elements. The friction will vary depending on the types of alloys being modelled. When the assembly is in contact, as the punch moves it will transmit shear and normal forces across the interfaces. The relationship between the two forces is called the friction between the contacting bodies. As the displacement rate of the punch is relatively small. This is done recreate the effective strain rate of a standard tensile test. Thus, the impact of the friction may not be significant. Starting from a typical steel-to-steel under partial lubrication [40,43,94] and then varying by lowering and raising from the baseline set up. It is expected that the punch and lower die chamfer radius will have an impact on the output of the ShP test. Contact interactions are modelled using Surface-to-Surface contacts and is described in further detail later in Part Interactions.

Modelling a right-angle corner in Abaqus can present issues due to node snagging [95], particularly with non-linear deformation and where friction effects will play a more significant role. Whilst it is possible to minimise these impacts by using surface-to-surface contacts, they still be present during the simulation. Additionally, in most experimental setups the machined surfaces will have a chamfer on the corners. If this is not present from the start, then over time with use a chamfer will wear in. A larger chamfer radius is easier to model as the shear zone on the deformable part does not require as fine of a mesh. The stress region will be distributed over a greater area onto the test piece, reducing localization of stress on one element. However, increasing the radius of the punch and/or the lower die increases the effective distance between the contact corners of the punch and lower die. As has been mentioned, when the test piece is undergoing deformation there will be bending and stretching. Correctly defining the radial clearance has been identified as an important parameter when controlling the mode of deformation. A clearance of 0.05mm or 10% of the specimen thickness is applied for all three simulations. The initial contact points change depending on the corner tip radius of the punch and lower die. The initial contact points will move further apart from each other as the chamfer radii increase. This increases the effective

radial clearance, introducing additional types of deformation. If the effective gap increases too much, then the deformation may no longer be shear dominant. For shear dominant deformation of the test piece it must be held firmly in place, without any movement allowed vertically or sliding. This is achieved by the clamping of the top die onto the test piece and limiting deformation to the region at the hole of the lower fixture as set out in [93] which was used as a baseline for determining the required parameters of the ShP test geometries. This is why the radius of the upper die should not influence the deformation of the rest of the sample and is considered a non-critical dimension provided the test piece remains clamped in place. This is set out in the CEN workshop agreement for testing of metallic materials by SP test [93] and principles for which the ShP test have been applied as well [51].

There are many engineering problems for which an exact solution cannot be found. FEM is a process that allows you to break down a complex system by dividing the problem region that needs to be analysed into smaller finite elements of a specified shape. Different problems that are being modelled require different approaches to get a result, this will be a balance between accuracy and time efficiency. The challenge in punch modelling is the low punch head velocity meaning that it sits in an area that can be considered “Quasi-Static” where either explicit or implicit modelling can be used. The other challenge arises from the non-linear deformation of the sample during the ShP test that happens in a highly localised area. This creates challenges around defining the contact between deformable and non-deformable parts, and the meshing of the sample where a fine mesh is needed in the deformation zone but a coarser mesh in areas that aren’t being deformed simplifies the model.

2.8.4 Small Scale Modelling in FEM

Many papers have commented on the macroscopic properties of DP steels being dependant on the microstructure properties [96–107] . Therefore, to encapsulate the material properties at the macro- and meso-scale it necessary to model at the micro-scale too. This is to find the local deformation mechanisms, strain partitioning and strain localization in DP steels. Better understanding the local deformation mechanisms allows for the manufacture of DP grade alloy with an optimized microstructure. This can be done alternating parameters such as the Many

investigations have been made to better understand and quantify the effects the microstructure has DP steels. The most common approach is to the Representative Volume Element (RVE) or also called a Unit Cell (UC). It is the smallest volume for which physical measurements can be made that is representative of the entire microstructure. These include for example, Young's Modulus or Thermal Expansion.

The major benefit of RVE numerical analysis is to have a real time view of what happens to the microstructure during deformation. As mentioned, studies have been done where DIC has been performed on mini tensile tests. As these have tended to be interrupted tests, certain deformation features may be missed and the loading-unloading cycle would is unrepresentative of a standard tensile test.

Larger RVEs will be more accurate but have a greater complexity requiring more computational power. Having a too small RVE which does not include the significant primary feature will produce unrepresentative results. Ramazani et al [108] investigated the minimum parameters needed to generate an accurate RVE. Concluding that the RVE edge length should be at least 24μm and contain a minimum of 19 martensite grains.

2.8.5 Dual Phase Steel Alloys

Dual Phase (DP) steels are a type of advanced high strength steel (AHSS) that was first developed in the mid-1970s [109] and has since gained a great amount of use within certain sectors, such as the automotive industry [110]. DP steels composed of a ferrite matrix with between 5-20% martensite content and typically have a tensile strength in the range of 500MPa to 1200MPa [111], depending on martensite content within the microstructure. The word "dual-phase" is used to describe ferrite-martensite structure that is typical for this kind of steel although there is usually lower bainite and retained austenite in the structure [112]. These alloy grades combine specific material properties that had historically proven difficult to obtain. Namely high strength with good levels of formability, high strain hardening and energy absorption [113], allowing for the manufacture of lighter weight structural components with more complex geometries. This has also allowed for an improvement in the passive safety features in vehicles [113], and due to reduced weight providing improvement gains in

fuel efficiency. DP steels show an improved combination of cold formability when compared to other low carbon and High Strength Low Alloy (HSLA) steels ([114]. DP steels are a low to medium carbon steel that is produced by the inter-critical annealing ferrite-austenite. The steel is then quenched transforming the austenite to martensite, with some retained bainite present. This process results in a microstructure which consists of a comparatively softer ferrite matrix with harder martensite islands distributed throughout [115], typical DP grade steels have in the region of 5%-35% martensite content by volume (V_m). The benefit of such a microstructure is the good global ductility due the softer ferrite phase with strains initially concentrated in the ferrite that surrounds the martensite. With the martensite providing additional strength to the alloy [116–119]. This gives DP ad

Chapter 7 draws on the on the major academic conclusions and insights that were drawn from this body of work. It highlights the major academic conclusions that were drawn from the research around th, whilst martensite is produced by the rapid quenching of austenite [120]. This can be seen in the steel phase diagram in **Fig. 10** – Phase Diagram for steel [121]where steel held temperature to produce δ-ferrite, and the temperature lowered to transform some of the ferrite into austenite before then being quenched to produce the final ferrite-martensite microstructure.

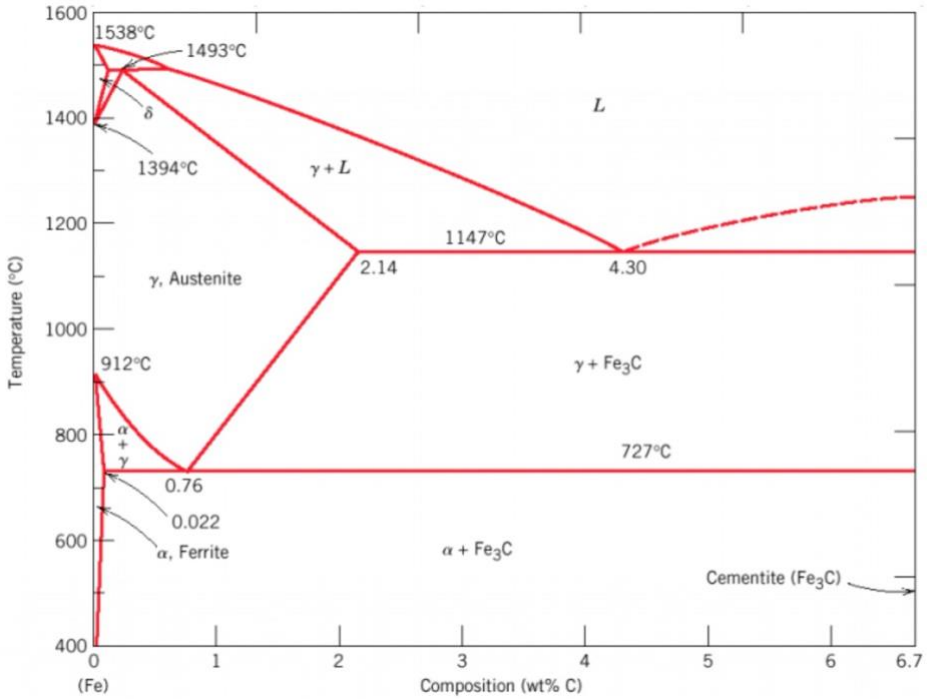

Fig. 10 – Phase Diagram for steel [121]

The ferrite gains additional strength from the initial dislocation density due to austenite to martensite transformation during the cooling process deformation [122–125]. **Fig. 1111** below shows the Global Formability Diagram (GFD) for different types of steel grades, it can be seen from that DP has for an equivalent tensile strength a higher elongation when compared to conventional HSLA. Hence their use in components that are produced by deep drawing [113,126]. Due to these properties much work has been done investigating and describing the deformation characteristics of DP steels for greater optimization in the manufacture and control of the alloy [107,110,127,128].

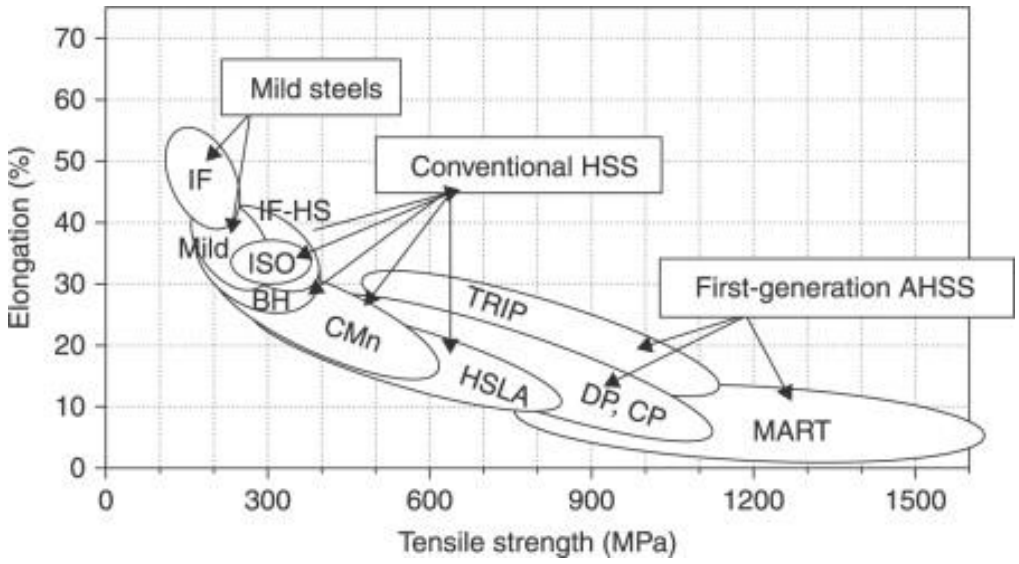

Fig. 11 – The Global Formability Diagram (GFD) of different steel grades showing typical elongation and tensile strengths [111]

Different methods have been used to describe and quantify the deformation in DP steels. One of the most popular is the composite model approach [129,130] to describe how DP grade steels obtain their combination of strength and ductility. In this description the harder martensite can be thought of as a reinforcing mechanism to the entire steel. Stresses are transferred through the ferrite matrix and interrupted by the martensite, effectively interrupting the load paths within the alloy. In this approach most of the stresses will be concentrated in the harder more brittle martensite phase with strains occurring predominantly in the softer more ductile ferrite phase. Whilst this approach greatly simplifies many of the mechanisms that occur during deformation, yet the composite model has been highly effective in describing the material hardening will good levels of accuracy [97]. DP steels come in a range of relative strengths depending on the use requirement. With more ductile alloys but a lower yield strength available. The strength of DP steels can be varied by altering V_m of martensite, by increasing the relative V_m of martensite a greater yield & ultimate strength can be achieved but with lower total elongations before failure when compared to DP steels with a lower martensite V_m. This is achieved by increasing the annealing time before quenching. Other factors that influence the tensile strength of DP steels include the grain morphology (i.e. aspect ratio), grain distribution, grain size and carbon content. The strength of martensite depends primarily on its carbon content

(wt%) [124,131,132], with a linear relationship in the yield strength and C wt% with other alloying elements being secondary. The control of phases present in DP alloys had been a challenge in the early generations of DP steel, with retained bainite present and the inclusion of weakly interconnected carbide particles present. These would reduce the strength of DP, causing early failure. This was particularly problematic for the carbide particles as they are weakly interconnected, during deformation they would de-bond from the metallic grain edges causing decohesion.

It is worth discussing the effects the secondary factors have on DP material properties. Grain morphology will impact on the concentration of stresses within each individual grain. It was found in [133] that the morphology impacted overall ductility more than the strength in DP steel. However, in [134] a simulation model of 3D periodic unit cells was used to investigate the effects of martensite morphology and grain orientation. They concluded that whilst these two factors had impacts at the local level leading to differences in strain hardening behaviour. Once results were homogenized/averaged to the macro level, these effects were negligible up to necking. And [135] it was found that fibrous martensite was more prone to cracking at low volume fractions.

In general elongated grains arise from the cold rolling of steel. The impact of that is known as the tensile loading with the rolling direction versus normal to the rolling direction will have a higher yield strength and greater elongation than loading in the transverse to the rolling direction. Hence why grain morphology will impact the performance of DP alloy. This is why manufacturers have spent considerable effort in obtaining equiaxed grains that have consistent properties throughout. For optimum strength of the global DP alloy, an even distribution of the reinforcing martensite phase is desired. Clustering will cause areas that are relatively weaker with others being stronger but much more brittle. This results in a discontinuous material property throughout and lead to early failure. This is a particular issue for DP steel with their use in deep drawn components. The effects grain size has can be explained via the Hal-Petch relationship, as grain size decreases yield strength increases. This is due to grain boundary strengthening, with dislocation propagation impeded from one grain to the other. As the adjacent grain will have nucleated and a grown at a different orientation

relative to a neighbouring grain. This different grain will have different preferred deformation direction. Causing a deformation of the following grain requires a greater activation energy. With smaller grain sizes, there is a greater number of grain boundaries that will dislocations propagating throughout the material.

2.8.6 Deformation of DP Steels

The method in which DP steels fail is an area of great interest. Due to the complexity in the microstructure [96,136,137] it is necessary to know how these alloys deform and fail. At the macroscopic level DP steels exhibit a uniform and homogenous behaviour during deformation. Where there is linear deformation in the elastic regime, followed by a transition into the plastic regime, work hardening of the alloy and then weakening followed by failure. In this regard DP steels behave similarly to other steel alloys. When observing down to the micro scale, the plastic deformation of the grains is inherently inhomogeneous due to its microstructure. DP steels have been reported to fail in the 3 following stages: 1) Void Nucleation, 2) Void Growth & 3) Void Coalescence, resulting in dimpled fracture surface [96]. With the formation of voids appearing to be dependent on the size, distribution, and morphology of martensite grains. Coarse grains deform via cleavage whereas in globular and more finely distributed grains voids occur at the martensite-ferrite interface rather than in martensite particles. This is true for DP steels with a low martensite V_m but at higher V_m fractions cracking of the martensite is the main failure mechanism. With a DP alloy with a more refined microstructure will have improved strength and formability compared to a coarse microstructure.

The martensite phase has been considered as the main source of failure in DP steel, with Ramazani et al. [96] finding that martensite cracking is the main failure mechanism in DP steel. Additionally, void initiation mechanisms have been associated with martensite islands. Observed modes of failure include decohesion at the interface between ferrite and martensite, fracture of the martensite islands, and deformation and ductile failure in the martensite phase. In [108] it was found that void initiation takes place in the vicinity of the martensite, with the subsequent growth and coalescence occurring due to ferrite failure.

Another study found that voids initiate by the failure of the ferrite grain boundaries. This has been explained as being due to the mismatch in deformation between grains of ferrite and martensite that are in the vicinity of each other. In [100] stress triaxiality, defined as the ratio of mean stress to the von Mses stress, was studied to see its effect on DP steels. They found that strain incompatibility during tensile testing comes from the difference in the flow characteristics of the ferrite and martensite phases. This results in strain partitioning, inhomogeneous deformation and finally deformation localization. Additionally, ferrite grains that are within the vicinity of martensite have their deformation constrained. The stress triaxiality can be varied by altering the martensite V_m. This showed that increasing martensite V_m causes an increase in the stress triaxiality with a reduction in the total elongation and higher UTS. Labinot et al. [118] found that due to the incompatibility in stresses of the two phases, the mean-stress in DP600, DP800 and DP1000 was significantly lower than in the martensite phase. With martensite being subject to much higher stresses when large plastic strains are applied. Additionally, most of the stress was observed in larger martensite grains than in the smaller ones.

Scanning Electron Microscope (SEM) analyses coupled with tensile testing by [107] have been done examining DP undergoing interrupted tensile deformation. They showed that ferrite would deform immediately and at a higher rate compared to the martensite phase. Martensite would show a delayed and comparatively lower strain rate. Additionally, DP steels with low martensite V_m deformation occurred almost exclusively within the ferrite matrix. Concluding that lower martensite V_m provides little strengthening of the DP alloy. Strain localization is the stage in the failure of DP steels with high levels of strain localized in a relatively small area of the microstructure. Voids grow and failure occurs at the ferrite-martensite interface leading to fracture. With the grain morphology playing a significant role in the failure mechanisms of DP steels [138]. Within the microstructure different failure mechanisms have been observed. Ductile failure occurs in the ferrite phase, brittle fracture in the martensite and interface debonding between the ferrite-martensite islands. When large strains are applied two effective localizations are observed 1) interface at the martensite and ferrite grains and 2) ferrite grains that are trapped

between martensite grains, for which the strain localization is much higher than ferrite grains surrounded by other ferrite grains. When investigating the fracture of tensile test specimens. Failure was affected by shear banding, strain localization and damage. With types of failure observed in DP steels. Ductile failure in the martensite grains, brittle fracture in the martensite phase and debonding between the ferrite-martensite interface. This type of failure can be explained by the flow strengths of the ferrite and martensite phases, with the ferrite flow strength weaker than that of the martensite. Plastic deformation will begin in the ferrite whilst the martensite remains in the elastic regime. The ability of the ferrite to continue deforming plastically is constrained by the martensite. This causes a build-up of the stresses within the DP, mostly concentrating in the martensite, but also within the ferrite. This concentration leads to a local concentration of stress resulting in failure of the DP alloy.

The effect of the microstructure cannot be ignored on the performance of DP steels. As mentioned, the carbon content (wt%) has been identified as one of the key strengthening mechanisms of martensite [132,139]. Other features such as the grain morphology, grain size and alloying content of martensite also impact the performance of DP steels. It can therefore be concluded that two DP grades with the same volume fractions of martensite and ferrite but either different grain sizes, shapes and alloy content will impact the overall performance of that DP steel. Kadkhodapour et al. [97] found that the shape of the martensite displacement is affected by the ferrite matrix. With martensite being displaced due to ferrite matrix deformation. With This displacement is not uniform throughout the microstructure and that those martensite grains not contributing to the global strengthening of the DP.

Despite the amount of research that has been performed on DP steels over the decades since they were introduced there are still gaps in understanding of DP steels in ShP testing. This shows that that much is still to be learned and the optimisation of material properties in DP steel is to be realised. This in all areas from initial production, through-processing, development of microstructure, deformation and failure of DP alloys. Much of this comes down to the complexity of the DP microstructure and the multiple elements that go into it [116]. DP may contain retained austenite, pearlite, bainite, carbides and needle-shaped (acicular) ferrite grains, depending on the

manufacturing route used. Significant complexity exists solely from the secondary martensite phase, the main reinforcing mechanism in DP alloys. Such as the martensite volume fraction (V_m), the martensite grain size (S_m), the martensite carbon content (C_m), the morphology of both the martensite and ferrite grains, the distribution of martensite grains, whether there is clumping or banding of martensite grains as has been found in some of the RAP DP800 steel [10,11,118,140,141].

Lastly, as deformation is dependent on the microstructure when deforming DP alloy over such a small area it can no longer be assumed that the results are representative of the bulk material. It is therefore necessary to simulate the deformation at the microscale, as material properties can no longer to assumed to be isotropic throughout. This is true where martensite particles may be elongated, clustered or form a banded a microstructure as in the RAP material [11,140].

2.9 Summary

This literature review has highlighted some of the challenges of using RAP for developing novel alloy grades, describing the challenges of downsizing test techniques, the history and use of novel test techniques for material property evaluation, DP steel grades particularly for the smallest RAP 40g samples, and the motivation for this thesis. The review has demonstrated the utility and importance of using FEA techniques for evaluating small scale testing, such as the punch style tests where evaluating stress evolution is key to understanding deformation of DP alloy grades and as a validation tool for physical experimentation and look evaluating the deformation at the microstructural level. The remainder of this thesis will explore major steps completed for this investigation.

3 Experimental Shear Punch Testing

3.1 Introduction

ShP test is recognised as a supportive means for the development and monitoring of structural materials, particularly for situations where only small volumes of material are available. This is true when safety concerns are present such as radiated materials or when wanting to evaluate ageing effects of in-service structural components. This chapter describes how metallic materials underwent ShP testing, two steel alloys of different strengths were tested with one being used for subsequent investigations but used to validate the testing technique. This chapter will then conclude how the results of DP800 alloy will be used for the following modelling work.

3.2 Materials Selected

Two materials were tested for the experimental setup. A softer, relatively more ductile DX57 and the DP800. These materials were selected to get two range of values for how the ShP test performs on different alloys depending on their relative material properties. The alloying composition of the two alloys is described in **Table 2** below. This material was obtained from Mach1 lab at Swansea University, the samples were pre-cut into 1mm thick discs of 0.5mm di3meter. A more detailed description of the material preparation is described in the following sections.

Table 2 - Composition for DP800 and DX57 provided by the Mach 1 lab in Swansea

Alloy	**Content (wt.%)**							
	C	Si	Mn	P	S	Ni	Cu	Cr
DP800	0.136	0.249	1.77	0.011	0.0027	0.018	0.024	0.558
	C	Si	Mn	P	S	Ti	/	/
DX57	0.12	0.5	0.6	0.1	0.036	0.5	/	/

3.3 Experimental Test Setup

Experimental setup followed a standard procedure as has been found in literature [30,40,43]. **Fig. 12** below shows a schematic of the ShP test setup, cut along the

centreline. Key components are shown with Pr being punch radius, Hr is the radius of the receiving hole for the lower die, Tr is the total sample radius, t is the sample thickness, R1 is the lower die & top clamp chamfer radius, R2 is the punch chamfer radius and c is the radial clearance between punch wall & top and bottom clamp wall.

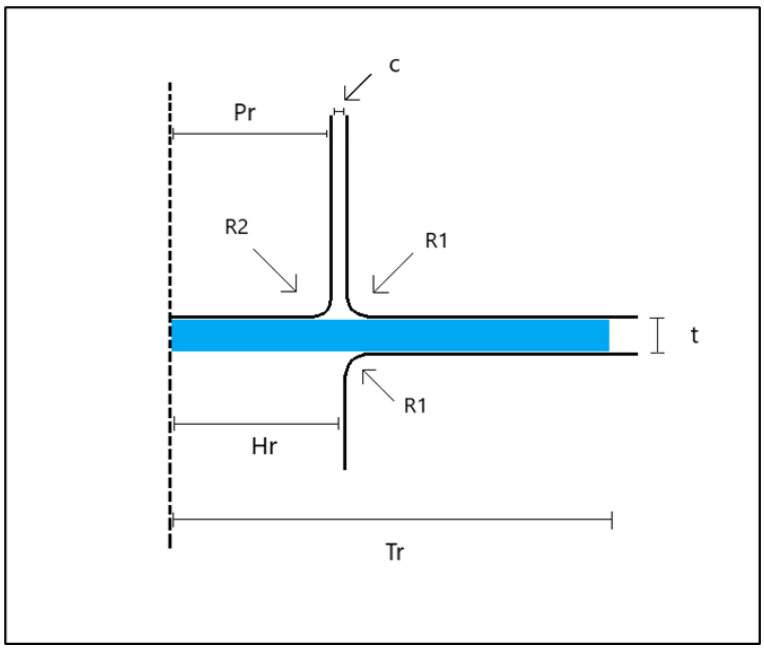

Fig. 12 – Schematic Diagram of Shear Punch Test setup, vertical axis is cut along the centreline. Pr is the punch radius, R1 is the fillet radius of the lower and upper clamp, R2 is the fillet radius of the punch, Hr is the radius of the receiving hole of the lower die, c is the radial clearance and is the difference in the length between Pr and Hr, Tr is the radius of the sample disc, and t is the sample disc thickness

3.4 Sample Preparation

Discs of material were provided; these were cut out from sheets of material produced at the MACH1 Lab at Swansea University. The initial thickness for both the DP800 and DX57 material were 1mm thickness. The CEN ASTM standard [93] states that thickness measurements of the discs should be taken at 5 positions, 1 at the centre and 4 at the outer edges. To prevent there being any chamfers on the disc that would affect the punch results. Here a Mitutoyo Digital Micrometer with a stated accuracy of 0.001mm was used to measure the disc thicknesses. The surfaces area of the clamping component of the micrometer itself was 5mm in diameter. Meaning that it was not possible to measure the disc as outlined in ASTM [93][[93]. Instead, when the samples were measured the micrometer was rotated 90° degrees and the edges measured to

account for any variation in the thickness. All the disc thicknesses were measured and recorded before being prepared for grinding.

The discs were placed onto a steel mount and stuck on using a thermosensitive wax. This wax is solid at room temperature but will melt into an adhesive liquid at temperatures above 50°C. This was chosen as a method to quickly mount a reasonable number of samples for preparation. The mount was paced onto a heat plate heated up to a temperature of 60°C. Once the mount had reached the required temperature a small amount of wax was placed onto it. The discs where then mounted 5 at a time on the outer half of the mount. This was to make sure an even pressure is applied to the discs whilst their thicknesses are being reduced. The combined thickness of the discs, adhesive wax and mount was measured and recorded to measure how much material was being removed during the grinding process without having to remove the discs. The mount was fixed to an automated rotary grinder, a silicon carbide disc was used as the grinding surface and water used as lubricant.

A initial grinding programme was used that specified how much material should be removed from the discs. This proved to be unreliable as the amount of material removed did not correspond to the program setting. Instead, a grind rate was determined for each material and then timed. No complete explanation could be found, but it was reasoned that due to the relatively small amounts of material that was ground away combined with the compliance in the system false displacement values were recorded which were not related to material being removed. Between each interval the thicknesses were recorded. This process was repeated until samples were within the 1% (0.005mm) tolerance, results are shown in **Table 3** below.

Table 3 - DX57 and DP800 Thicknesses

Specimen ID	Thickness
No units	[mm]
DX57-1	0.522
DX57-2	0.498
DX57-3	0.502
DX57-4	0.486
DX57-5	0.501
DX57-6	0.495
DP800-1	0.504
DP800-2	0.505
DP800-3	0.5
DP800-4	0.505
DP800-5	0.502
DP800-6	0.533

For the DX57, 2 samples were outside the 1% tolerance. With DX57-1 and DX57-4 being too thick and too thin respectively. For the DP800 only DP800-6 was thicker than the required tolerance. This sample was still tested in ShP to evaluate thickness effects on results. These sample were used assess the impacts of being outside the permitted tolerances.

3.5 Results

Punch loading was performed on two steel grades, stronger harder DP800 and softer more ductile DX57. Tests were performed on the two different steels to evaluate the impacts of different relative material properties on outputs from the ShP test. **Fig. 13** below shows the average of output curves for DP800 and DX57. The DX57 alloy validates the testing procedure as the expected results for those steels are that DP800 would be a stronger alloy compared to the DX57, which can be seen. The DX57 is also known for its good formability which also shows here with its greater deflection up to

failure compared to the DP800. From those two comparative curves it can be seen that DP800 is stronger with a higher peak punch load of 2500N. But has a lower ductility with a reduced specimen deflection and the sample failing at 0.21mm. The DX57 has a comparatively lower peak punch load of 990N, but with a greater ductility with the specimen failing at 0.48mm, more than double than for DP800.

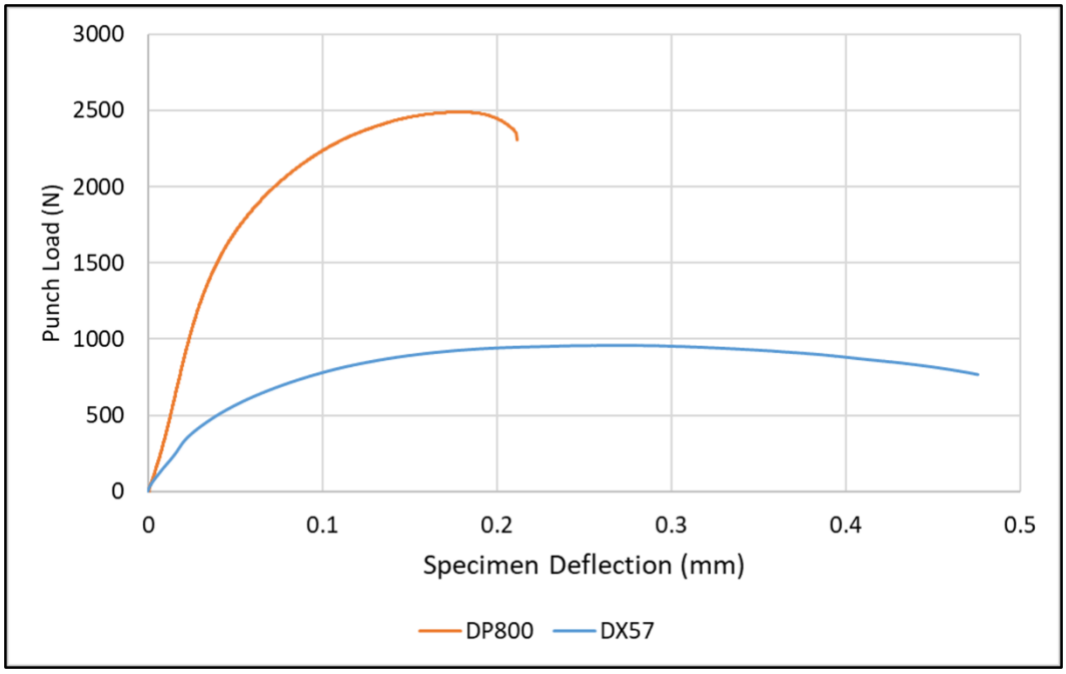

Fig. 13 – Mean Load Deflection curve for typical DP800 and DX57 alloy undergoing Shear Punch test. The curves show mean curves for the DP800 and DX57.

These results show the general applicability of the ShP test for steels with relative properties. That that the DX57 has a much higher ductility is expected with it being a type of Interstitial Free (IF) steel [64. With IF steels characterized by very high levels of formability and have been widely adopted to fabricate car body parts [142].

Fig. 14 shows the total force deflection curves for all DP800 samples tested in ShP testing. This demonstrates the general repeatability of ShP testing technique. It can be observed that the alloy material responds in the following way; First there is an initial linear elastic deformation of the steel, this is then followed by a reduction in the angle of the load deflection curve. This is the point at which plastic deformation is taking place. This is followed by work hardening and continued plastic deformation until the sample reaches its peak load. At this stage damage has built up to the point where the

sample is weakening. This weakening continues up to the point of failure. Only DP800-3 stands out as an outlier for which no explanation could be found. Microstructural analysis of the sample could elucidate the reasoning for this but is outside the scope of this research project.

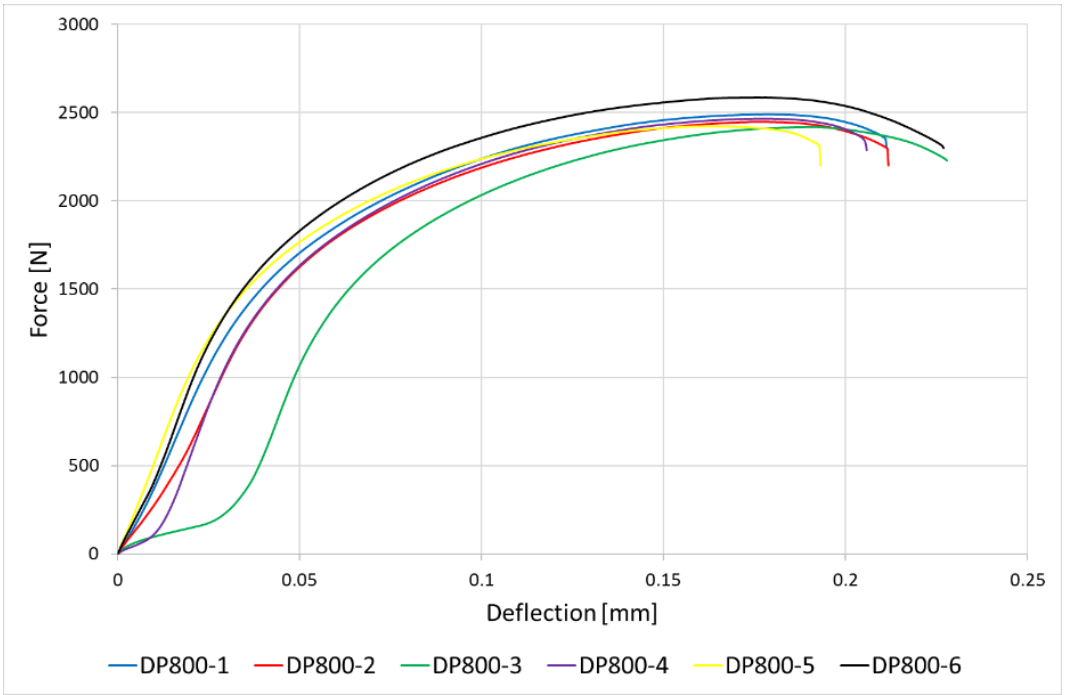

Fig. 14 – Force Deflection curves for DP800 alloy, note the variation in the curve for DP800-3 showing an initial higher amount of deformation for a lower punch load

3.5.1 Thickness Effects

Thickness effects were investigated for both DP800 and DX57. It is expected that an increased thickness results in an increased load for a given displacement. However, as the shear stress (τ) equations account for sample thickness these factors should be mitigated, this is can be seen in **Fig. 15** for DP800 when converting the peak punch load to peak shear stress and plotted against sample thicknesses. A regression line has been used to show the relation the initial sample thickness has on the output of shear stress when it is accounted for in the load to shear stress conversion using equation **(4)**. To what extent this can compensate is not fully explored. For DP800 the thickness varied from 0.5mm to 0.533mm (6.6% thickness deviation) exceeding the 1% tolerance permitted in the CEN ASTM [93] .

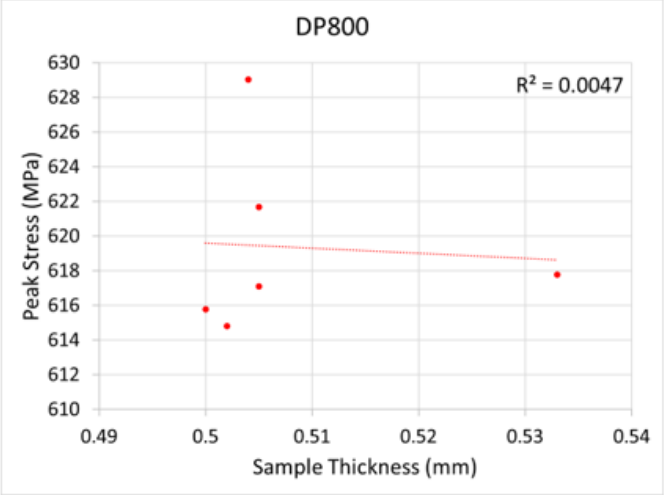

Fig. 15 – DP800 Peak Stress when accounting for sample thickness

3.6 Summary

Two different alloy grades were tested under ShP testing technique. Those being a relatively softer but more ductile DX57 and a stronger but relatively less ductile DP800 which has not been performed until now. The two different grades were tested to validate the testing on steel alloys with different strength characteristics. It was expected that a more ductile material would generate results which follow known trends. That DX57 performed in such that it was stronger but failed at a lower sample deflection shows that the ShP test produces different outputs depending on material properties. This allows for the generation of models the ShP test which can be validated against experimental results. Thickness were also investigated which validate that the applied conversions for obtaining stress values accounts for the sample thickness when known inputted into equation (4).

4 Axisymmetric Modelling & Parameter Study

4.1 Introduction

This chapter presents the main conceptual thinking about process steps involved in developing the axisymmetric model of the ShP test. Due to the tests relative novelty for the development of novel steel grades there are no established testing standards or explanations for why certain steps are used. The aim of this part is to determine the impacts different setups have on the ShP test before more complex 3D models are developed. This will be done in 2D axisymmetric as a method to develop multiple models that can be run in short order. The methods for obtaining material properties from standard tensile tests results that are then put into the Abaqus model is also discussed. At the end of this chapter the main geometric variables in the ShP test setup will have been outlined and discussed which will be key for developing future 3D models with more complex damage mechanisms.

4.2 Parameter Study Objectives

The objectives of the parameter study were to investigate and quantify the effects varying key geometries has one the ShP test setup. It is known that the radial clearance plays a key role in ensuring that the specimen will deform in a shear dominant manner. If there is an excessive clearance and the effective shear zone area is too great, then potential excessive bending will cause the other deformation mechanisms to become dominant. Previous studies have not commented on the corner tip radius of the either the punch or the lower die [40,43]. However, both these corner tip radiuses can be expected to have an impact on the deformation of the sample. With a greater radius it can be expected that more of the sample will deform around the corners with a greater distribution of stress around those areas. For the purposes of FEM modelling, corner radius must be prescribed to prevent a stress singularity in the simulation. Additionally, the appropriate mesh size needs to be used, with a finer mesh required for a smaller corner tip radius. The friction effects on ShP test setup have not been widely reported. Standard lubricated steel on steel friction has been used as this most closely replicates the test setup. Due to limited sliding in the test rig from the clamps holding down the

test piece, friction effects are expected to have limited impacts on the deformation response of the test piece. The final parameter investigated is effect of sample thickness on simulated results. A thinner sample will be expected to have a reduced resistance to load for a given amount of punch displacement. Following CEN ASTM [93] standards there should only be a 1% variation in thickness from the prescribed 5mm. But as shear stress is a function of the sample thickness it can be expected that some of these thickness effects can be accounted for.

4.2.1 Parameters Investigated

The table below shows the main parameters that were chosen for the study and what the different variations if each parameter. It should be noted that **2)** Radial Clearance was altered by varying the Punch radius. The figures in bold show the standard setup that was used for the ShP test; Sample Thickness 0.50mm, Punch Radius 1.2mm, Friction 0.1μ, Punch Corner Tip Radius 0.05mm and Die Corner Tip Radius 0.05mm. When one variable was varied all the variables were kept in the standard setup. These variables are shown in **Table 4** below.

Table 4 - Variables in Parameter study going from lowest setting to highest, standard measures are highlighted in bold

	Setup Parameter	**Variables**
1)	Sample Thickness (mm)	0.45, 0.47, 0.49, 0.495, **0.50**, 0.505, 0.51, 0.53, 0.55
2)	Radial Clearance, Punch Radius (mm)	1.10, 1.15, **1.20**, 1.25
3)	Friction (μ)	0.05, **0.1**, 0.2, 0.3, 0.5
4)	Punch Corner Tip Radius (mm)	0.01, 0.03, **0.05**, 0.1
5)	Die Corner Tip Radius (mm)	0.01, 0.03, **0.05**, 0.1

4.3 Model Set-Up

4.3.1 Primary Geometry of Master Parts

The master geometry for the model was based on experimental results that were performed on prepared samples and what has shown to be some consensus within known literature. The samples were modelled on tests done by Guduru [40,43].

A sample thickness (t) of 0.5mm was selected for the sample. As the deformation is highly localized within the shear zone, the sample was partitioned into 3 parts, 1) Inner Zone; 2) Shear Zone; 3) Outer zone. This is to allow an easier creation of a structured mesh. The sample thickness was chosen as the reference length for the width of the shear zone. This created a square segment where a structured could be applied. An initial punch radius (r_P) of 1.25mm was chosen with a die radius (r_D) of 1.26mm, giving a radial clearance (c) of 10µm. For both the punch and the die a corner tip radius of 0.05mm was selected. On the top clamp smaller 0.02mm corner tip radius was used. As little deformation is seen in that part of the sample arising from the clamp, this was maintained constant throughout the study. The disc is defined as a deformable solid and the tools are defined as analytical rigid surfaces. The clamp surface's main purpose is towards holding the sample in place and prevent any uplift of the part whilst the punch is driven against it. The model setup, including partition of the mesh is shown in **Fig. 16** below. This shows the cross-sectional setup of the axisymmetric ShP model. As the deformation occurs predominantly in the shear zone which lies in an area between the punch and lower die the test piece is divided into three sections.

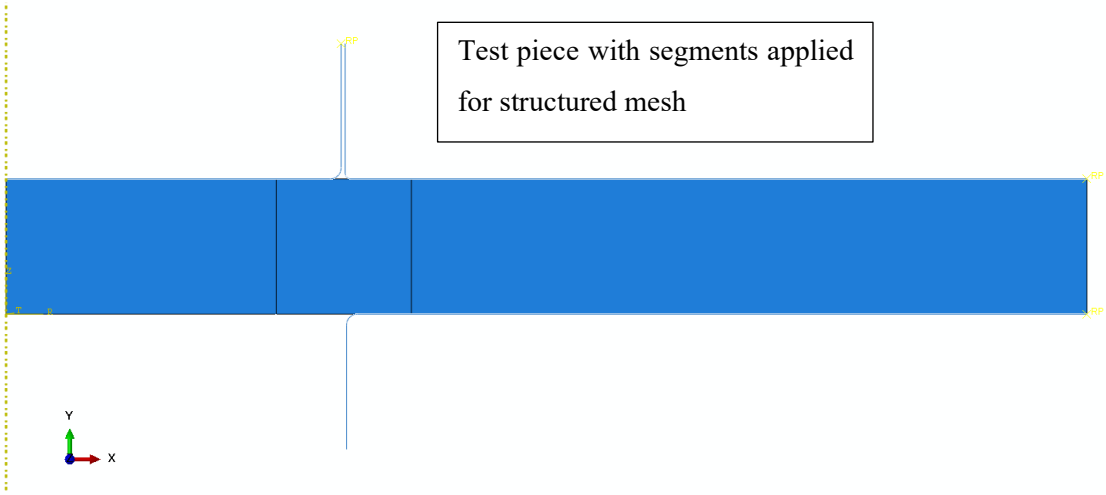

Fig. 16 - Cross Sectional Diagram of parts in ShP Test setup for parameter study

Owing to the large deformations in the shear zone of the sample during testing non-linear material properties were applied. For this a DP800 high-strength low-alloy (HSLA) steel with a 70%$_{Vm}$/30%$_{Vm}$ Ferrite-Martensite was used for the modelling of the axisymmetric ShP test. The DP800 was produced via a process of hot and cold

rolling, and heat treatments mentioned in previously. Samples obtained for the tensile material properties were taken from production material, with multiple sampling in the coil to minimize property variation, same preparation methods used in [11]. The material properties were obtained via previous work done in MACH1. This was completed using tensile testing following ISO and ASTM [143] techniques on standard full-size specimens.

From these tests a true stress-stress strain curve was obtained from the engineering stress-strain curve. The initial stages of plastic deformation were considered key for evaluating the simulated deformation responses in this section. Particularly with what are potentially minor changes being made to the setup of the rig or sample thicknesses only small variations may be observed between the different variables. It was therefore considered necessary to have many small increments in the initial plastic strain. A simplified Johnson-Cook (J-C) [141,144–146] plasticity model was chosen for this with the constants of constitutive equation determined from the stress-strain data. The J-C model, is a function of von mises tensile flow stress and consists of strain hardening, strain rate hardening, and thermal softening [147]. The J-C has been used by several researchers with good success when performing similar work on HSLA steels. The original J-C [141,144–146,148] model is expressed as:

$$\boldsymbol{\sigma = (A + B\varepsilon^{n})(1 + C \ln \dot{\varepsilon}^{*})(1 - T^{*m})} \quad \textbf{(9)}$$

Where A is the initial yield strength, B and n are flow stresses, C is the strain rate effect, ε * is a material parameter below the transition temperature, and T^{*m} is the static yield stress. As the tensile tests were performed at a standardised temperature and strain rate the J-C model can be simplified to just the first component with only the Yield Stress, Coefficient of strain hardening and strain hardening exponent needing to be determined. With the following equation used in the model material parameters obtained from [141,144–146,148]:

$$\boldsymbol{\sigma = A + B\varepsilon^{n}} \quad \textbf{(10)}$$

Results from the simplified constitutive equation were overlayed onto the plastic stress-strain curve with the coefficients varied until graphs matched with ±1% deviation in stress values for a specified strain value. These constant values were then used to determine the plastic stress as specified strains, the results for which were put into tabular form in the Abaqus model. The initial plastic strain up 0.1 had smaller intervals of 0.001 to 0.01, then followed by intervals of 0.02 up to 0.1, and then in 0.05 intervals up to 0.75 plastic strain.

Fig. 17 shows the engineering stress-strain for DP800 obtained and the converted true stress-strain from the MACH1 lab as part of Prosperity Partnership's development of RAP alloy [9,10]. This was converted to True Stress-Strain, from which the Young's Modulus was determined.

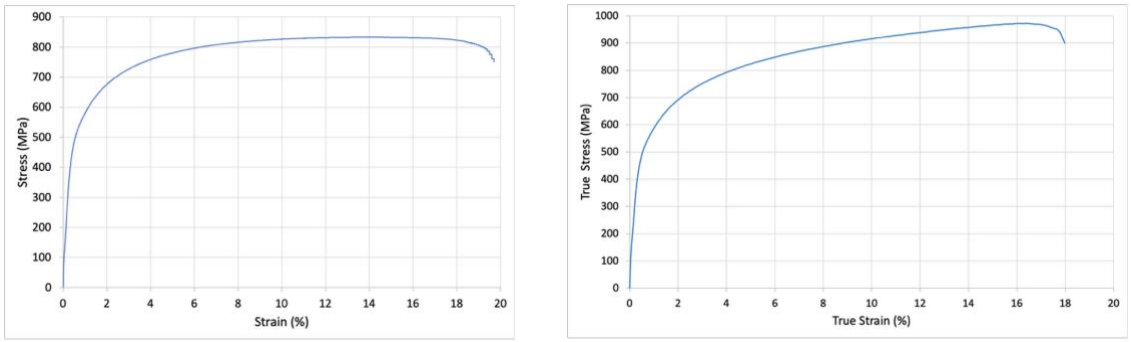

Fig. 17 – Engineering Stress-Strain and Trus Stress-Strain curve for DP800 used

This True Stress-Strain curve was then converted into Plastic Stress-Strain. These material properties property were used for all subsequent simulations of DP800 in Abaqus. **Fig. 18** shows the final true plastic stress vs plastic strain that was developed from the A B n values that were used in axisymmetric modelling.

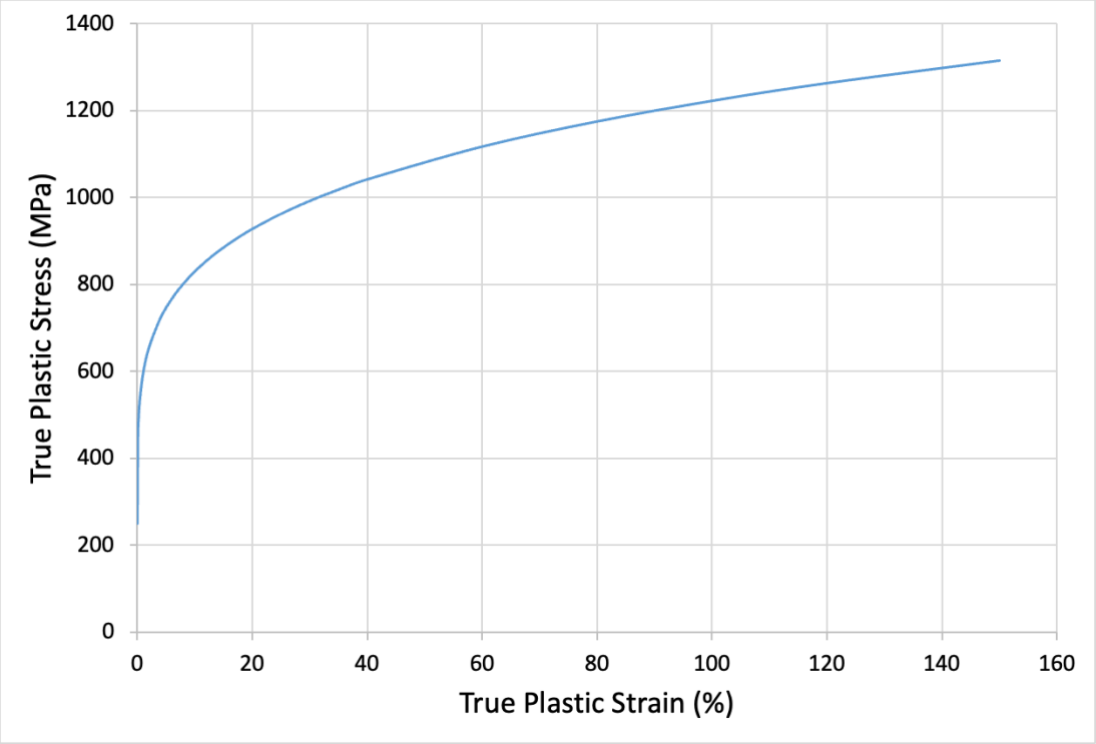

Fig. 18 – True Plastic Stress-Strain for DP800 used for the material property in the model

The other material parameters in the model include the Young's Modulus (E) at 207GPa, a Poisson's Ratio of 0.29 and material density of 7.8E-09 tonne/mm^3 is used, this are displayed in **Table 5**.

Table 5 - DP800 properties

Young's Modulus (MPa)	**207,000**
Poisson's Ratio	0.29
Density (tonne/mm^3)	7.80E-09
A	250
B	1136,14
n	0.2244

4.3.2 Part Interactions

A Master-Slave interaction was prescribed to all parts that were in contact with each other. As the sheer-zone experiences highly non-linear deformation the correct Master-Slave interaction needs to be prescribed. In this setup the sample is considered the

touched body and subject to deformation making is the slave surface. As the top and bottom clamping surfaces, and punch are analytically rigid, they were prescribed as the master surfaces. The sample was considered to have a top and bottom surface. The Top Surface was paired with the Punch Top Clamp, whilst the Bottom Surface was paired with the Bottom Clamp (receiving hole). Finite sliding with Surface-to-Surface discretisation method was used on all surfaces, and a baseline friction of 0.1μ to begin. Surface-to-Surface contact interaction enforces contact interactions over an average of the nearby slave nodes rather than individual nodes and works well with metal-to-metal contact that is being modelled in the ShP test. The friction value was alternated manually for each variable. The final assembly for the parts is shown in **Fig. 19** below. The sample top and bottom edges were considered slave surfaces in all interactions with the punch and clamping surfaces.

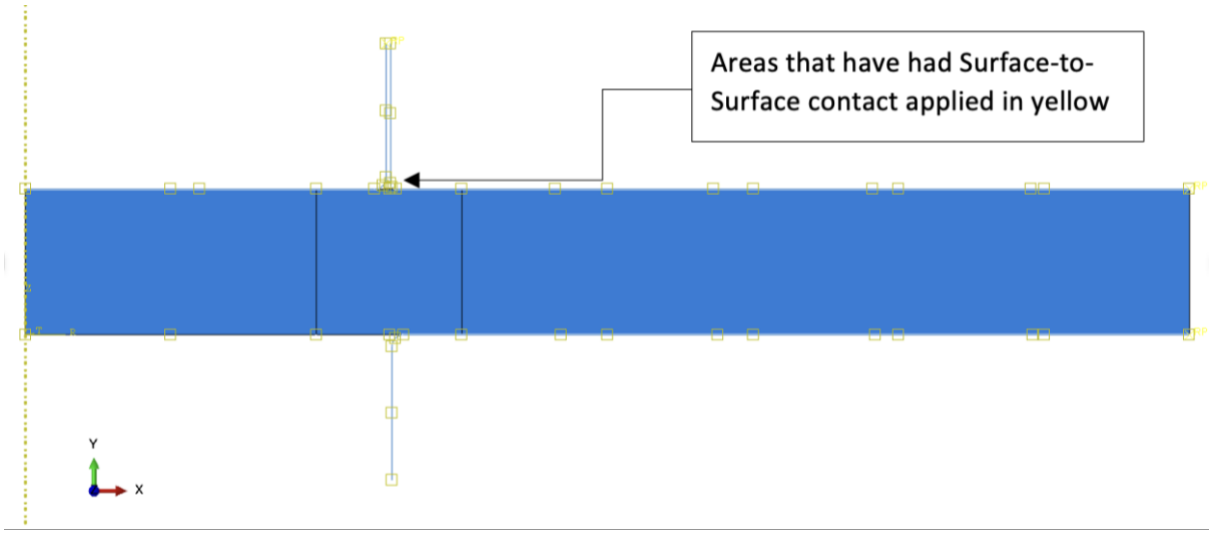

Fig. 19 – Interaction between surfaces of the Assembly

4.3.3 Meshing of Deformable Parts

The zones of high stress and strain are expected to occur at the boundary area between the punch and the lower die with an influence of the stress beyond those zones. This is therefore the area which likely to be experience the highest amounts of deformation during the ShP test simulation. In the ShP test the main area of deformation and corresponding high stress is concentrated the 'shear zone' located in the gap between the outer punch and the receiving holes of the die clamps and is the area of interest in the parameter study. Because of that a high-density mesh is prioritized in the 'shear

zone', with a lower mesh density on either side of it. This compromise allows for a faster computational speed as there are fewer elements that need to be calculated whilst still obtaining accurate results. For this a shear zone of width 0.5mm was chosen for the sample, with the centre of the zone at the midpoint between the punch and lower die. This results in a 3-part partition in the axisymmetric model. The shear zone using a structured quadratic mesh and those parts either side using a free mesh with the distance between nodes increasing the further away from the structured shear zone. CAX4R continuum elements were used to mesh the entire part, these are 4-node bilinear rectangular elements using reduced integration [149] typically used for axisymmetric modelling in Abaqus. Hourglass control was applied to the elements to prevent excessive mesh distortion. This is used to improve the accuracy of the model that has a non-linear material response at high strains. This improved accuracy does come at the cost of a higher computational cost [75]. The final cross-sectional mesh is shown in **Fig. 20** below.

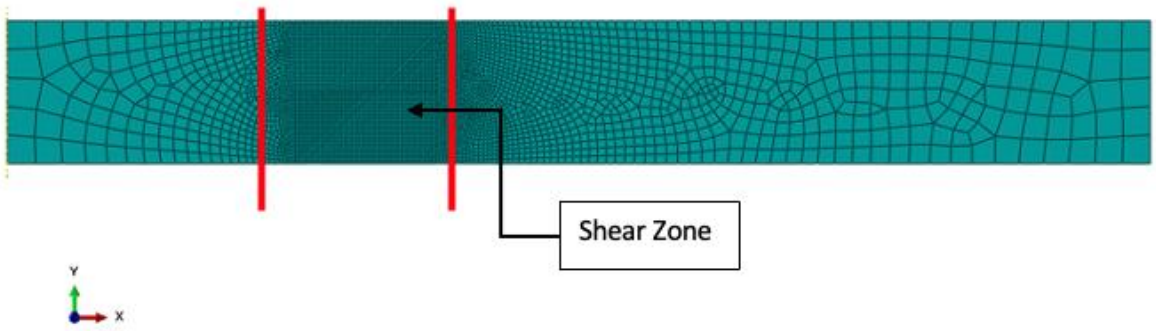

Fig. 20 – Cross sectional view of disc, a higher density mesh has been applied in the shear with coarser mesh in areas of low deformation

4.3.4 Boundary Conditions

Boundary conditions were applied to the upper clamp and lower die, and the punch. The clamp and die have encastre conditions applied to them, no having any movement allowed. As there is no movement allowed for the experimental punch setup the same has been applied to the FEM simulation. The punch has a prescribed displacement applied to it in the y-axis of -0.22mm and a 0mm displacement in the x-axis. No boundary conditions are applied to the sample, being allowed to move freely.

Conditional movement is dependent on the interaction with the clamping surfaces and the punch. Using the axisymmetric modelling approach, the centreline is the centre of the sample, no displacement boundary conditions are needed. The final assembly with boundary conditions is shown in **Fig. 21**.

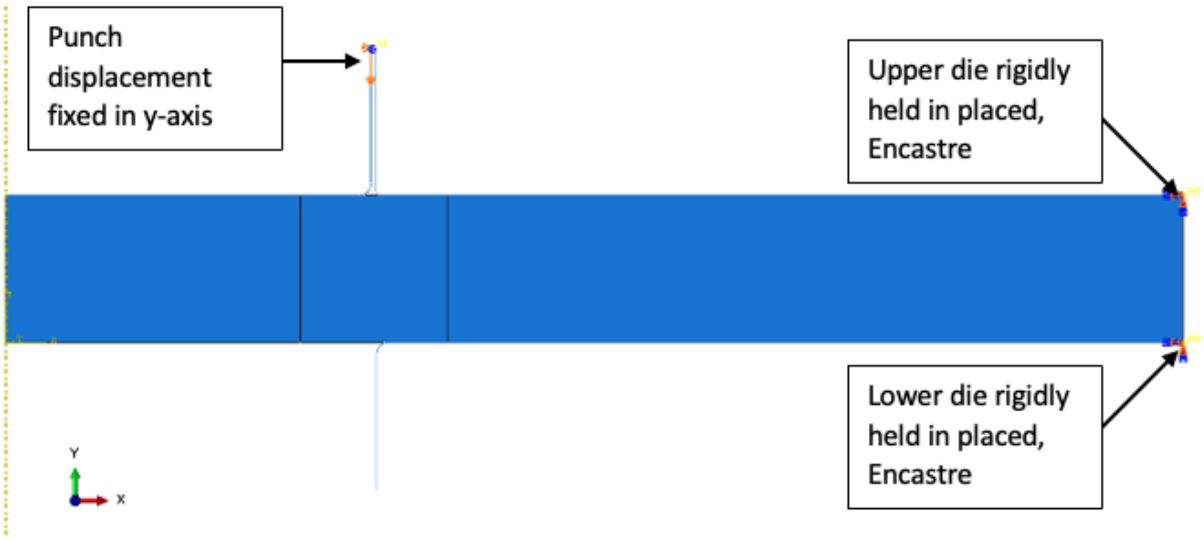

Fig. 21 – Assembly boundary condition applied to the RP in the holder, lower die and punch. No boundary conditions are applied to the test piece and is held in place through friction from the lower die and top holder

4.4 Mesh Sensitivity Analysis

A sensitivity analysis was performed within the shear zone. This is done to identify how fine the meshing approach needs to be within regions of high deformation to obtain results that can correctly predict what the global output will be. Due to the highly localised deformation within the simulation, problems can arise due to non-convergence of solutions. Smaller individual time steps would be needed for a successful analysis or a smaller mesh in these high deformation zones. Four mesh densities were chosen within the shear zone, ranging from a 0.05mm edge length to 0.001mm edge length. The node distances on the outside of the shear have a bias applied to them, with the inter-node distance increasing further away from the shear zone. This allows for a graduated mesh density, allowing for a higher mesh density in the high deformation shear and a coarser mesh in the remaining sections which do not undergo the same amounts of deformation.

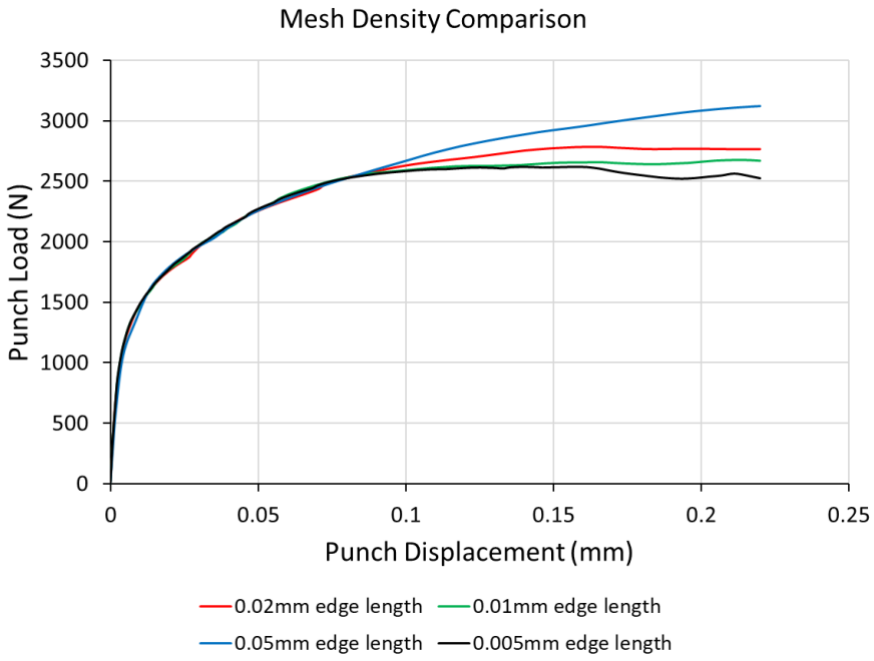

Fig. 22 – Mesh Density Comparison

Fig. 22 above shows the results the varying of mesh densities has within the shear zone of the deformable test piece. In the early stages of deformation, the linear elastic area and even significant amounts of plastic deformation up to 0.07mm displacement, there is little difference in the punch load of the simulation. Therefore, the amount of non-linear deformation within the elements does not have a significant impact on the putput results. Additionally, whilst the global punch displacement may be the same in all, with the lower mesh densities there is a higher level of deformation in each element compared to the higher mesh densities.

Whilst it is desirable to have highest possible mesh density available for each simulation run to have the most accurate results. With increasing mesh density, the number of computations required for each time step also increases. This increases the total amount of time needed to run a simulation. A comparison of the mesh densities and computation times is shown in Error! Reference source not found. below. This shows that the computation time required for an analysis increases linearly with the number of elements in the shear zone.

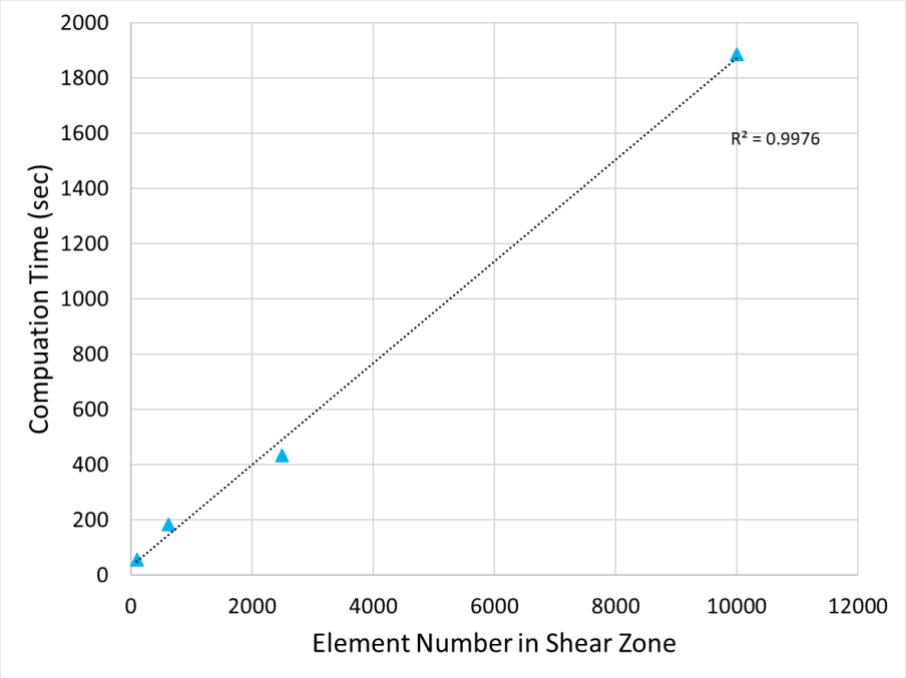

Fig. 23 – Elements in the shear zone comparison with computation time

Despite not showing a significant difference in the punch load results until much later in the simulation. It should be noted that as the numbers of nodes increases linearly the number of elements will increase by the square. This will exacerbate the time problem especially once complex damage parameters are included. For the subsequent parameter analysis an element edge length of 0.01mm was chosen. This showed good quality in terms of results being very similar to the finer 0.005mm element edge length whilst not taking an excessive amount of time to run a simulation. Punch displacement and load was limited to the point at which damage initiation would begin. Punch load was not extended as element deletion was not active in axisymmetric 2D modelling, element deletion not being an option for this modelling regime. The punch displacement was limited to the point at which damage onset would happen.

Fig. 24 and **Fig. 25** show the deformation with an element edge length 0.05mm and 0.01mm respectively and both at the same punch displacement. Whilst the von Mises stresses in the elements are similar for both mesh densities, with peak stress at 1315MPa. Additionally, the sample is not able follow the contours of the punch tip and die corner tip radius. It can therefore also be concluded that the node distance must be shorter than the corner tip radiuses of the punch and die. A smoother curve around

the lower die corner is needed to effectively model the deformation of the disc. Stresses in the area outside the shear zone are also affected by the mesh density. With higher effective stresses throughout the sample rather than the more local stress in the shear zone.

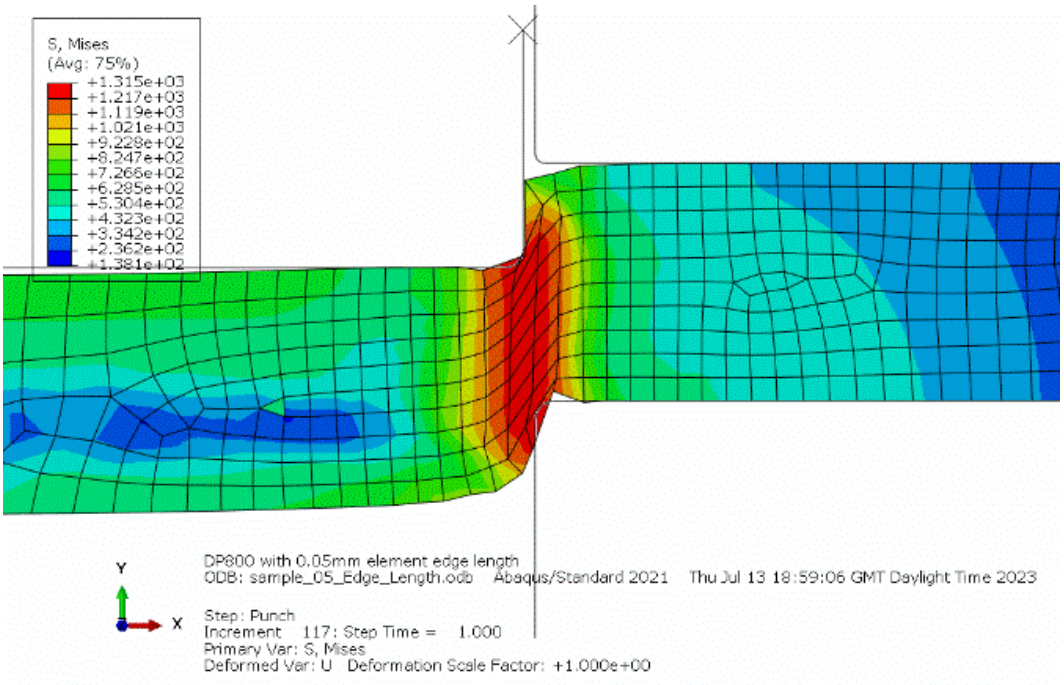

Fig. 24 – Coarse mesh in the shear zone

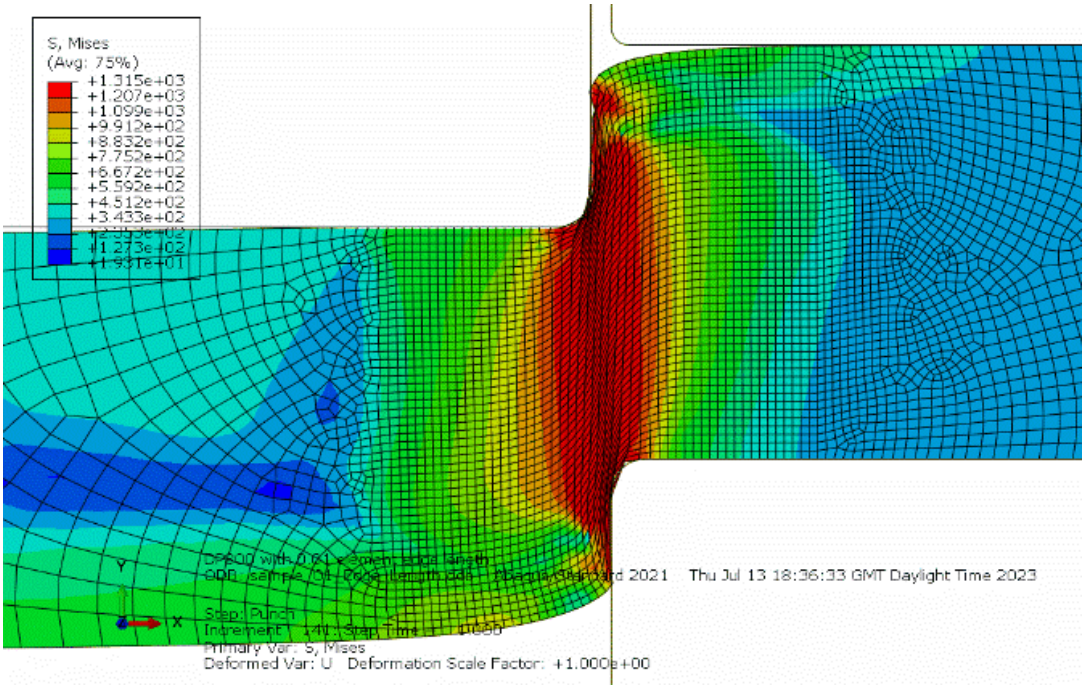

Fig. 25 – Structured higher density mesh in the shear zone

4.5 Results XY Data Plots

Simple XY Punch Force and Displacement was obtained from all simulation results. These were chosen to be the main values as this could easily be standardised for every setup parameter, streamlining analysis of results and simplifying comparisons between all the results. For that will be done with experimental analysis on ShP tests, this also allows for a more straightforward comparison of results as these will be the same outputs results.

Additional image analysis is used to view where stress initiates in the sample and how it subsequently propagates during the deformation process. Due the nature of the ShP test it is not possible to view what happens to the sample during a test. Whilst interrupted testing with image analysis has been done on standard tensile tests, the

cycle of loading and un-loading impacts material behaviour. For disc specimens where it is clamped in place this is not possible. Samples have been cut post-test for analysis

4.5.1 Friction

The effects of friction are shown in **Fig. 26** with the friction coefficients ranging from μ=0.05 to μ=0.5. A 0 value for the friction coefficient was not included for this investigation as it this was not considered comparable to real world conditions. The objective being to investigate the effects of increasing friction from a baseline that is below expected real world conditions to one that is higher than real world conditions.

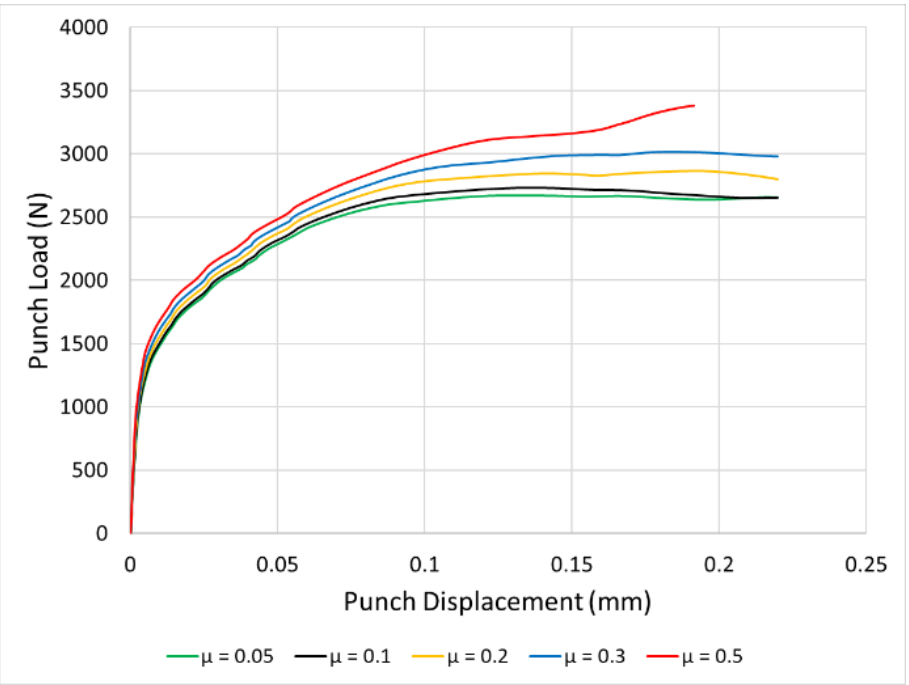

Fig. 26 – Friction effects of the ShP Test

In the early linear elastic deformation of the sample, friction has a small effect in the punch load required to push against the sample. As the deformation within the elements increases and become more non-linear friction begins to have a greater on the result outputs. There is tipping point in all cases where at first the load-displacement curves follow identically to each other before they then start diverging. This likely due to moving away from purely bending to also having sliding of the punch against the surface of the sample. As the punch continues to drive against the sample, a greater surface area comes into contact and interact with each other. With

this greater interaction leading to increased friction effects. In this case, a greater friction coefficient leads to an increase in maximum loads that will occur in the punch for a given displacement. Ripples can also be seen in the punch load curves, this likely caused by node snagging where the curvature of the punch corner tip has been caught between two nodes which results in an elevated load. This continues until the node is released which results in a drop in in the punch load.

During the elastic stage of deformation friction has a negligeable impact on the outputs for the simulated ShP tests. As the punch continues to drive against the sample and moves into plastic deformation the resistance experienced due to the higher friction causes the required load to achieve a specific displacement increase. It can therefore be concluded from the simulation results that friction will have an impact on the outcome of the ShP test.

4.5.2 Effects of Sample Thickness

When looking only at the effects thickness has on the load displacements curves, a relation can be seen between the load required to achieve a displacement. With an increasing punch load required to achieve the same displacement value. It is expected that with a greater sample thickness the load required for an equal amount of deformation is going to be higher relative to a disc with a reduced thickness. This would be due to the greater amount of material present to resist the load that is applied to it. Using the same tolerance for sample thickness of 1% the SP test, or 0.005mm, It can be seen that in the **Fig. 27** that the difference in load for a given displacement is smaller than the values that are outside the allowable tolerance. This is expected from the simulation with isotropic material properties in the simulated sample. The overlayed curves also show two distinct phases in the load-displacement of the sample. During initial deformation, the linear phase, the loads required to deform the sample are closely aligned and show little difference. It can be inferred from the modelling that during initial non-plastic deformation there is little effect of sample thickness on the simulation output.

As the punch continues moving against the sample and deformation moves into the non-linear regime a divergence in the sample behaviour start being observed. Whilst

the type and progress of deformation appears the same for all sample thicknesses, the required load to achieve the same measured punch displacement increases. It can be concluded that when measuring basic outputs of punch load, punch displacement, and sample deflection it is necessary to control the initial thickness of the sample so that it is within the allowable 1% thickness variation.

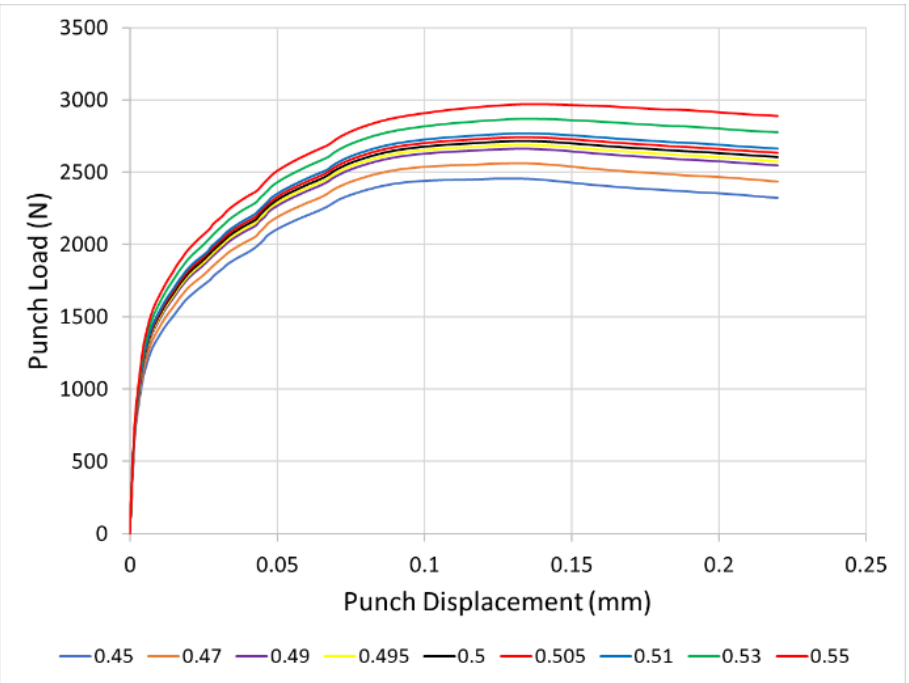

Fig. 27 – Effects of sample thickness on load displacement curves in Shear Punch test

However, as the results are not viewed in isolation the simple view how the sample would behave under load is not enough. As discussed earlier, the outputs are modified to produce a Shear Force-Normalized displacement curve. All the load-displacement curves were modified to into the Shear Force-Normalized Displacement with the varying sample thicknesses used for each corresponding simulation run. The results for which are shown in **Fig. 28** below. Once the sample thickness is accounted for the output curves come much closer together. There are still some small deviations in the output, some of this may be due to the mesh applied to the sample. As the node-to-node was standardised for sample thicknesses, some of the samples would have the same number elements throughout. This would cause some minor variations in the sample output. However, the variations are small enough that it is not affecting the accuracy of the simulation results. More variation can be expected in the results from

experimental analysis using samples from the same production batch and with identical thicknesses due to variations in localized material properties when using ShP test and other miniaturized test techniques. Therefore, once the thickness has been accounted for in the Shear-Stress, the effects from sample thickness can be accounted for.

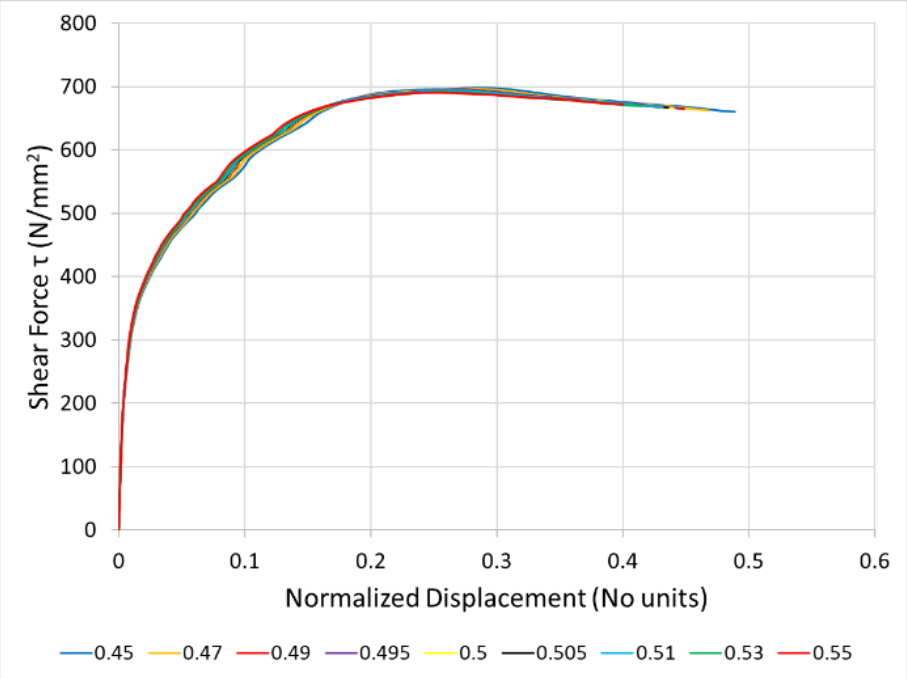

Fig. 28 – Shear punch tests results expressed as shear stress and normalized displacement. Shear stress is in part a function of the sample thickness

To further investigate the effects of sample thickness on punch load and Shear-Stress, two displacement points were chosen for all samples; a displacement of 0.05mm and 0.10mm. **Fig. 28** shows the punch load vs displacement for those two displacements and **Fig. 29**. shows those points modified to Shear-Stress vs Normalised Displacement. When looking at only the punch load, the variation in results ranges from 400N to 470N for 0.05mm and 0.10mm displacement respectively. Suggesting a uniform variation in results equal to about 20% of average punch loads.

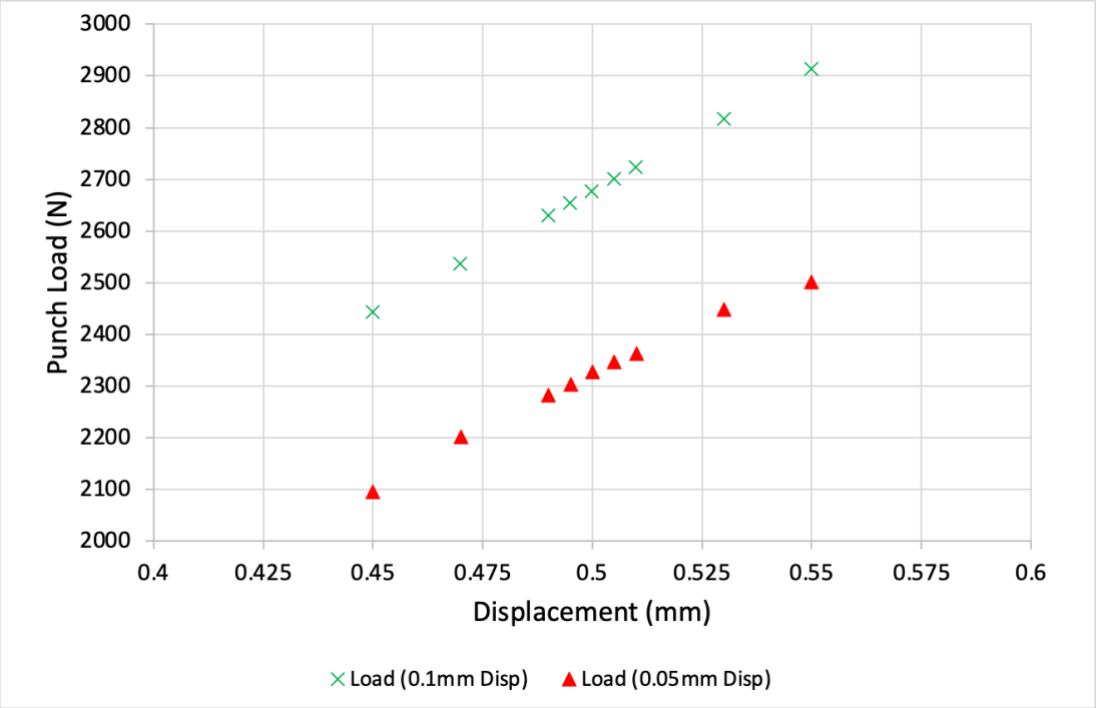

Fig. 29 – Punch load at a specific displacement of 0.05mm and 0.1mm. Increases sample thickness requires an increasing load to obtain an equivalent displacement

When looking at the **Fig. 30** for shear force vs normalized displacement the values moves significantly closer to the average. With a variation of 30μ to 10μ for 0.10 δ (normalised displacement) and 0.20 δ (normalised displacement) respectively, or 5% to 1.5% variation in stress. For the lower ND, the difference in shear force values is higher. However, this is just for the higher variation in sample thicknesses. When outlier thicknesses are excluded and sample specifications within allowable tolerances is used instead the variations in shear forces drops down to 1.5% for both 0.1δ (normalised displacement) and 0.2δ (normalised displacement).

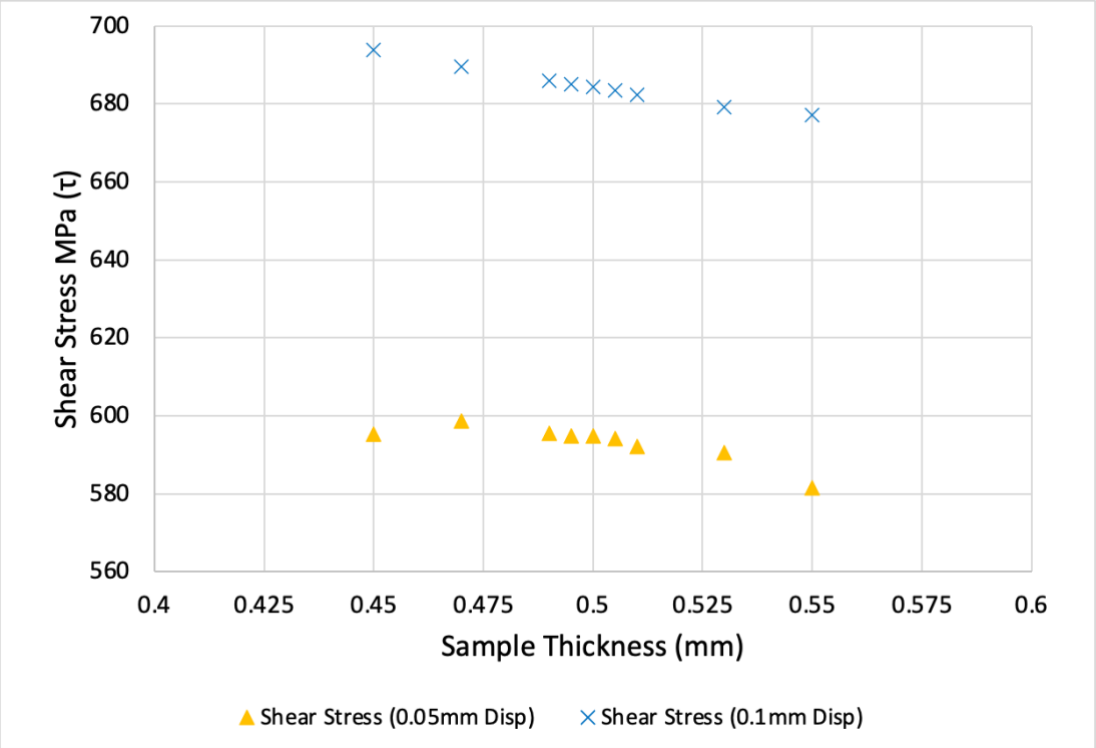

Fig. 30 – Shear stress and a specific normalized displacement. Effects of sample thickness are reduced once accounted for in stress and normalized displacement

Sample thicknesses were varied from the standard 0.5mm to ±10% as well as the allowable ±1%. Results show that as sample thicknesses increase the required load to achieve the same displacement increases. When the basic outputs are converted to shear stress and normalized displacement the effects of thickness variation are reduced. When the sample thicknesses are within the allowable ±1% variation the effects are negligible.

4.5.3 Radial Clearance

One of the key features of the ShP test is the shear dominant deformation that the sample undergoes. Limiting the amount of bending of the sample is controlled by the effective radial clearance in the simulation setup. The effective clearance was varied by altering the punch radius. Increasing the gap between the punch edge and lower die and increasing the deformable region of the sample. The parametric results cannot be compared directly to literature as this type of testing was not found to have been done on a similar steel alloy.

The punch load and punch displacement are shown in the **Fig. 31**. below. This shows that with decreasing radial clearance the punch load required for an equivalent punch displacement increase.

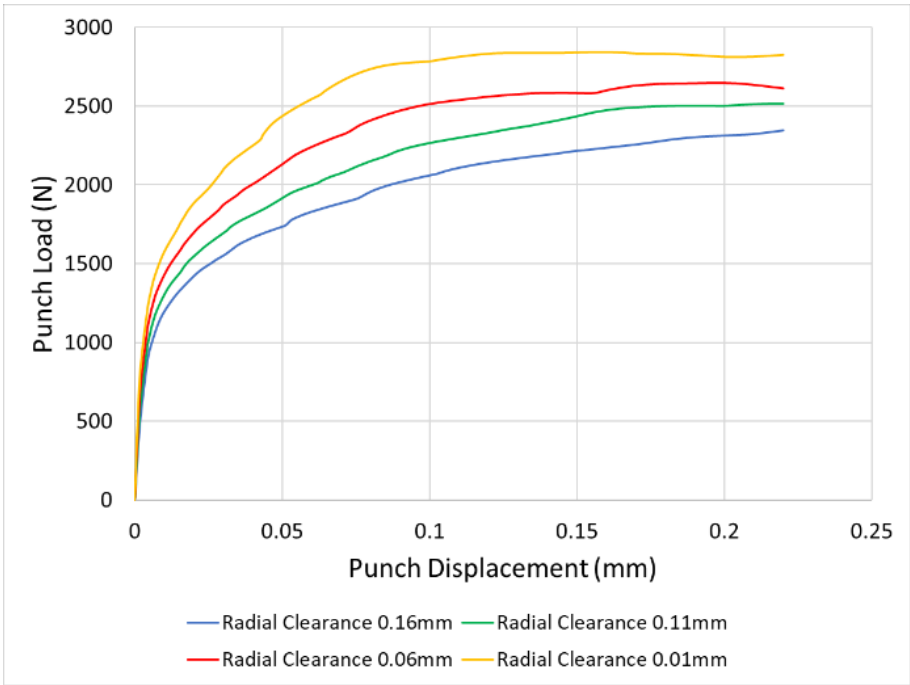

Fig. 31 – Effect of varying radial clearance on the shear punch test

This suggests a greater resistance to deformation from the punch as it continues to drive against the sample. Analysis from **Fig. 31** shows that the increasing of radial clearance effectively increases the region of the sample that is subject to deformation, effectively decreasing von Mises stress within the sample.

The method employed for increasing the radial clearance was achieved by reducing the punch radius whilst the radius of the lower die was kept constant. In this case, increasing the punch radius will increase the average radii of the punch and lower die. With an increasing punch radius the effective radial clearance in reduced. The greater average radii should reduce the average shear stress for a given load. Therefore, by converting the punch load to shear stress there should be converging of values for different radial clearances. These processed results are sown in the **Fig. 32** below.

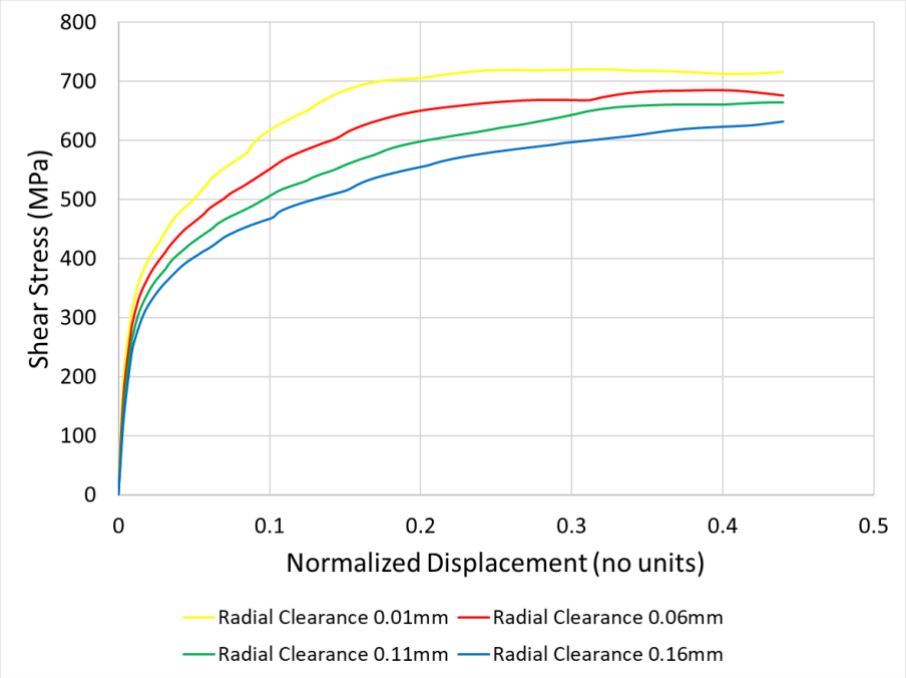

Fig. 32 – Radial Clearance Shear Stress vs Normalized Displacement

The modified results show no major difference or convergence of results when using Shear Stress vs Normalized Displacement. This suggests that controlling radial clearance of the setup is key for maintaining repeatability and when comparing results for different materials. Ensuring that the shear zone within the sample is within the desired radial circle of the punch setup.

The radial clearance was modified by varying the punch radius. Simulation results show that with a decreasing radial clearance the punch load for a given displacement increases. The way modification to simulation setup was done, the decreasing radial clearance would have a higher average radius of the punch and lower die. As shear stress τ is a function of punch load and average radius r_{avg}, a greater r_{avg} would result in a lower shear stress. This however showed no major change in results with there still being a divergence of values in the plastic deformation regime. Showing that controlling the effective radial clearance in the ShP test setup is key for repeatability in results.

4.5.4 Punch and Die Corner Tip Radius

At time of writing, there does not yet appear to be much published research into the effect of varying the radii ShP testing of the punch and lower die. Most published [43,58,150] work shows a schematic with the punch and clamping surfaces having perfect right angles, nor is there comment on it when discussing the model set-up. It is also worth investigating the impact of changing the lower die from a fillet to a continuous radius chamfer.

The results for the punch and die corner tip radius variations have been included in the same set of results in this section. It was observed that the global response was similar for both when looking at either varying punch or die corner tip radii. When looking the internal deformation of the test piece, differences can be observed in the von Mises Stresses. The initiation of high stress occurs at the start of the curved section from where the punch or die surface is no longer in contact with the punch. It can be considered that the dominant type of deformation will be dependent on the corner radiuses. Furthermore, when looking at the punch tip radiuses only, increasing the punch tip radius but maintaining the same punch tip radius has the effect of increasing the high deformation shear zone within the test piece. This will impact whether the deformation is shear type dominant. It will also increase the amount of bending the occurs within the piece before the onset of plastic deformation. Locations for onset of stress is shown in **Fig. 33** and **Fig. 34**.

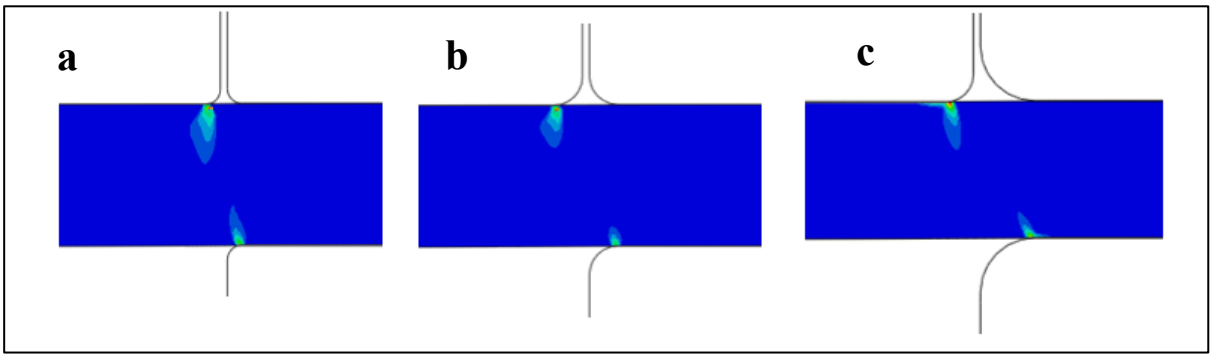

Fig. 33 – Varying of punch and die fillet radius. The clearance between the punch and dies remains constant. A) radius of 0.05mm B) radius of 0.1mm C) punch radius 0.1mm, die radius 0.2mm

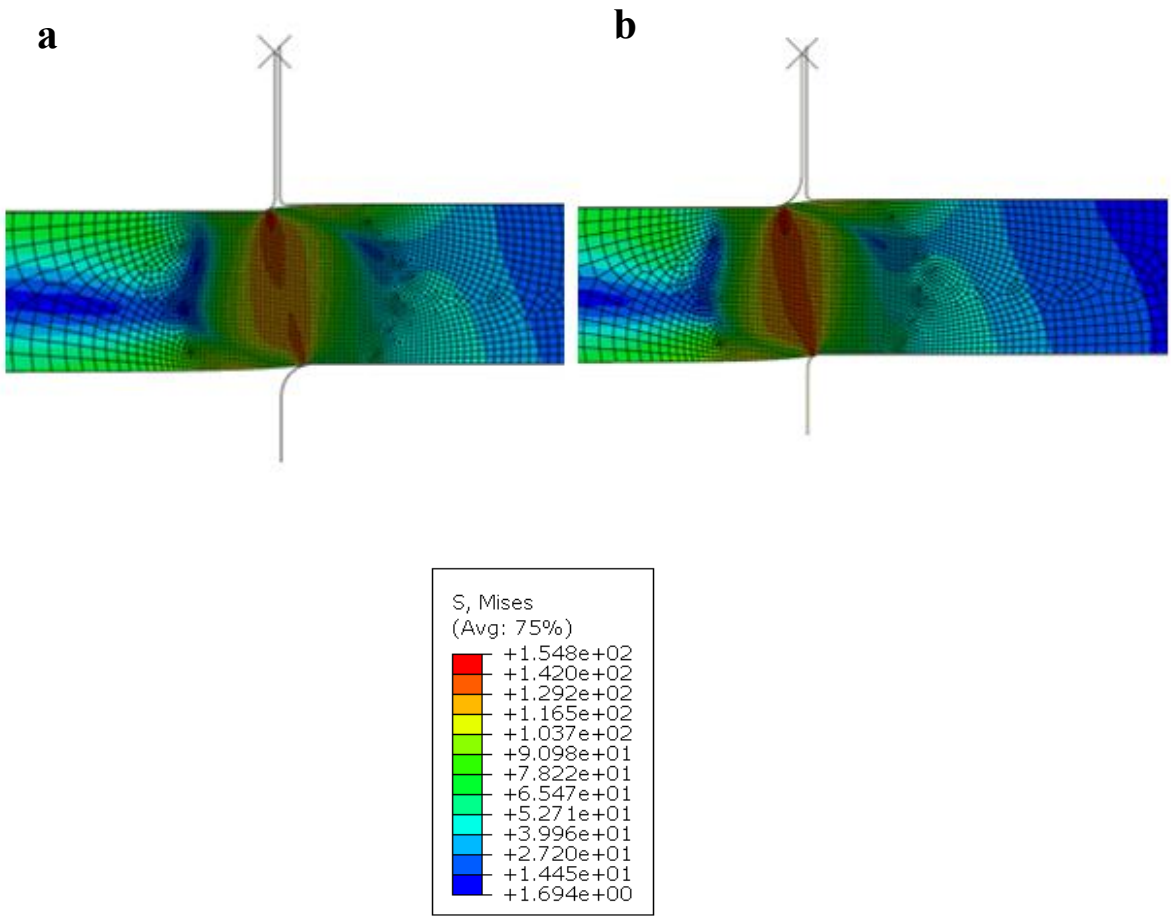

Fig. 34 – a) Die Corner Tip Radius 0.1mm & b) Punch Corner Tip Radius 0.1mm

The figure below shows the punch vs displacement results of the ShP test with the different punch tip radius. Overall, there is not a great difference in the effects that the punch corner tip radius has on the outcomes of simulations. With the exception if of a corner tip radius of 0.1mm, where the initial onset of plastic deformation occurs at lower load than the reduced radiuses. As the punch displacement increases the required load increases for the for the larger corner radius increases relative to the other three reduced corner tip radiuses. This is likely from the effects of having a greater amount of the sample interacting with the punch. As more of the sample is being deformed, the punch is effectively having to push against a greater amount of material that is interacting with it. Load curve distributions are shown in **Fig. 35**.

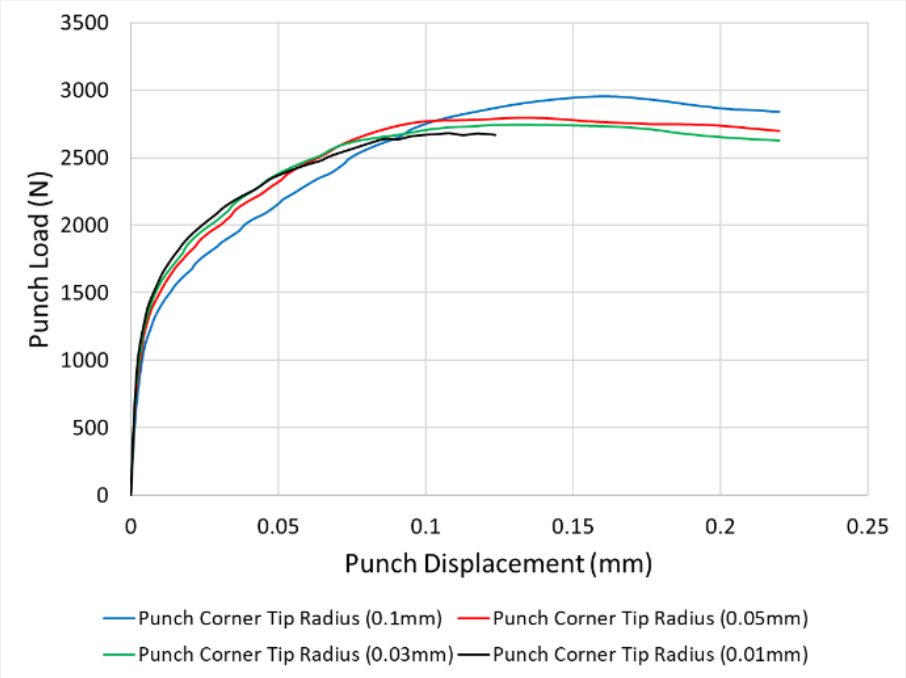

Fig. 35 – Effect of varying punch corner tip radius on load displacement curves

Fig. 36 further shows the impact that the increasing corner tip radius has on the ShP test simulation. With an increasing radius effectively increasing the radial shear zone wear deformation occurs.

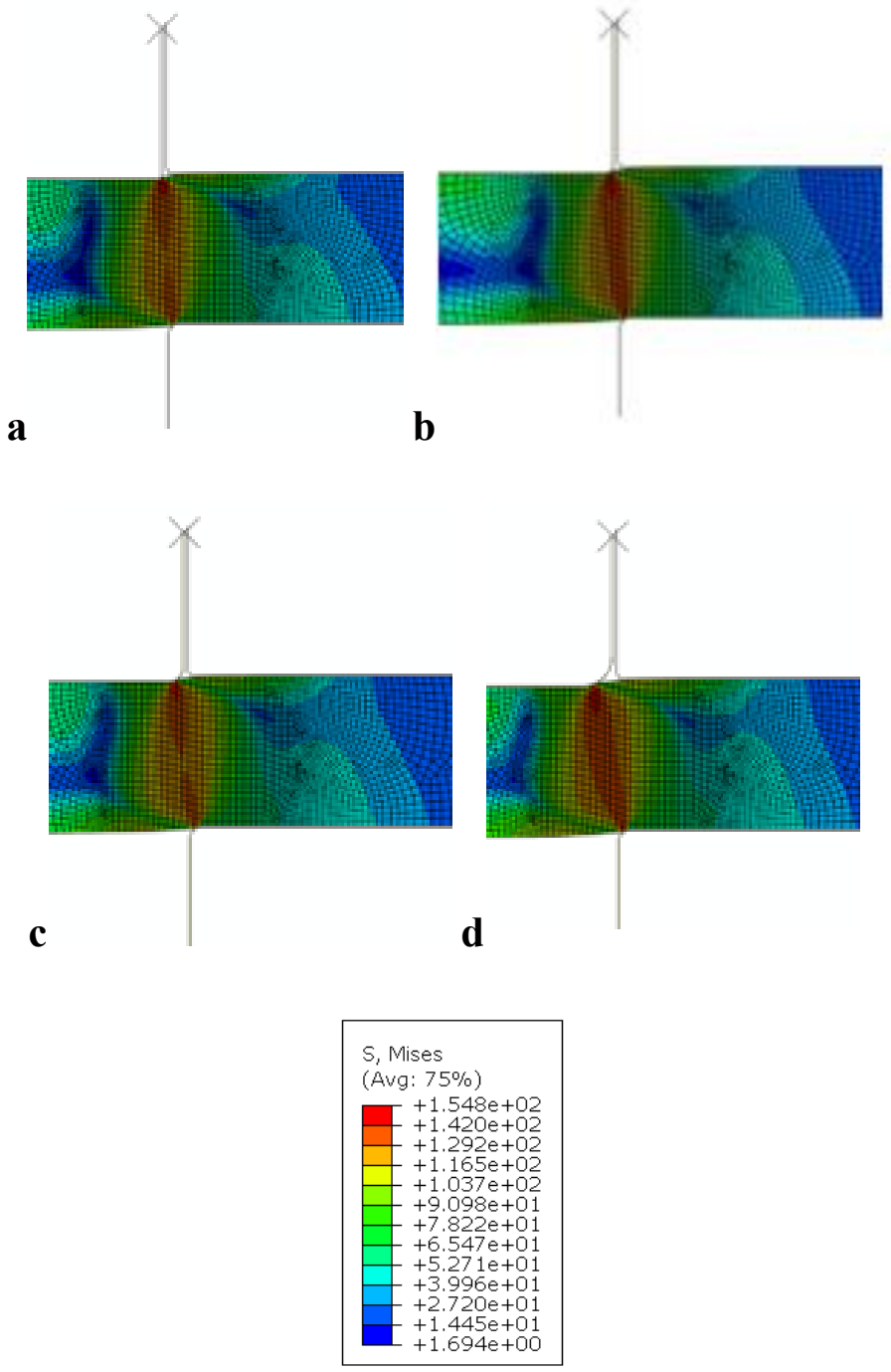

Fig. 36 – Effects of increasing punch corner tip radius from left to right: a) 0.01, b) 0.03mm, c) 0.05mm, and d) 0.1mm

4.6 Shear Yield Points

The impact of radial clearance c was investigated by varying the punch radius whilst the lower bore radius, punch chamfer radius and friction were maintained at a constant

value. This then allowed for the clearance to be altered whilst all other parameters remained unaltered, eliminating other possible impacts on the simulation results. Three simulations were run in Abaqus with the punch load and punch displacement results are shown in **Fig. 37**.

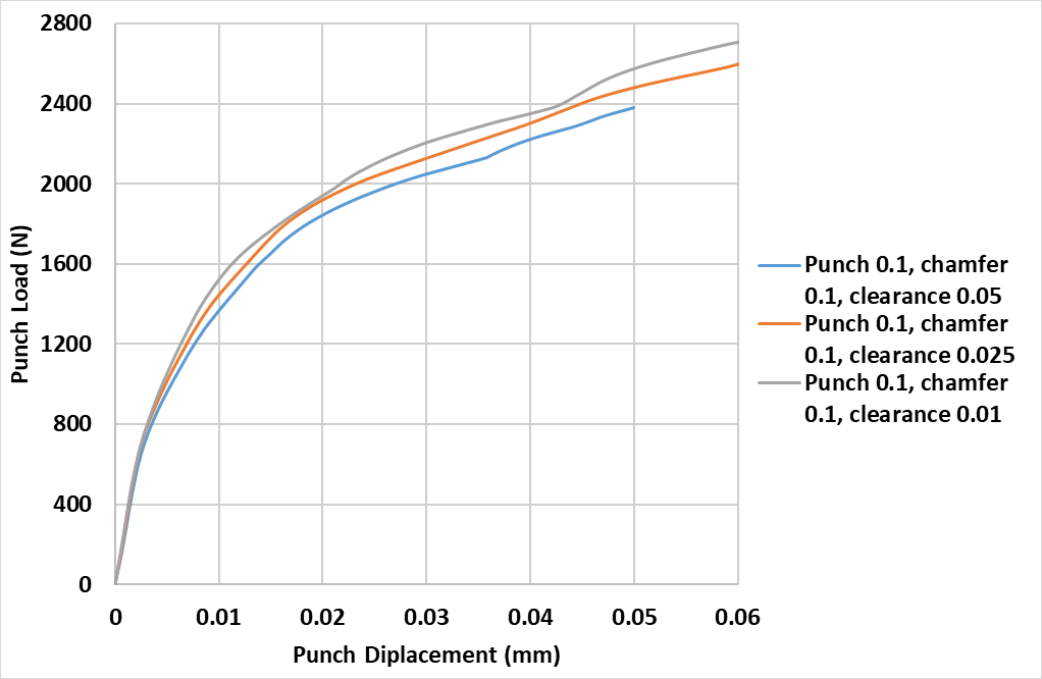

Fig. 37 – Simulation Results of Varying Clearances

The results were subsequently analysed to determine the Shear Yield Strength τ_{ys} for the three simulation runs. The 0.15% Normalized Displacement Linear offset was used for the FEM model. Briefly, the intersection point was determined by first estimating the slope of the linear elastic region in the Shear Stress-Normalized Displacement curve. A linear line of the same slope was translated along the horizontal axis 0.15% of the Normalized Displacement (or 0.0015). The intersection is the point at which τ_{ys} is estimated. A typical Shear punch curve with the intersect is shown in **Fig. 38**.

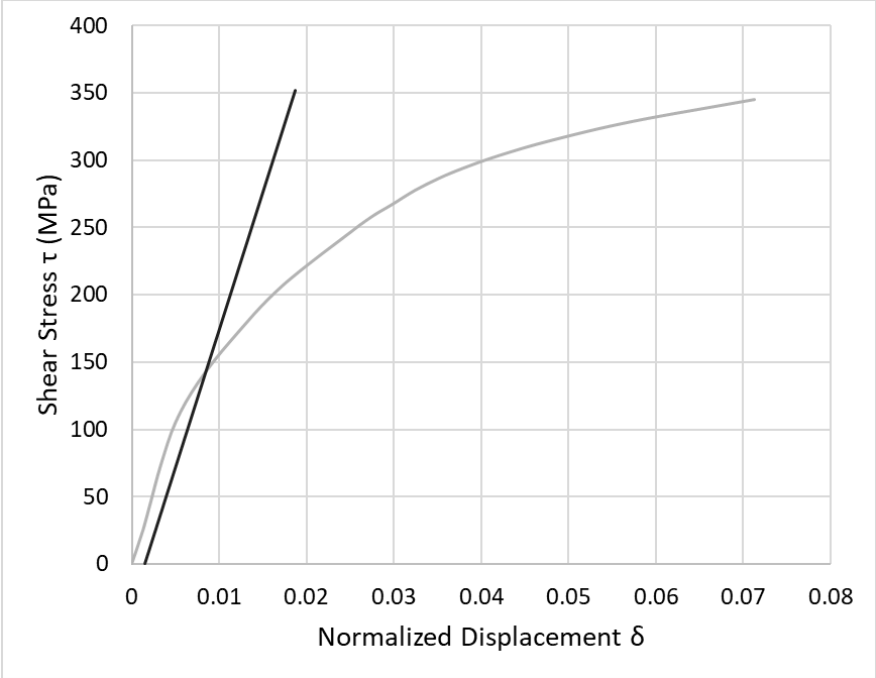

Fig. 38 – Typical Shear Punch Curve with the Intersect

The intercepts are shown for typical simulation is shown in above figure **Fig. 38**. The intercept points occur at different normalized displacements but at approximately the same shear stress. Alternatively, this is expressed as; for a reduction in the radial clearance, there is an increase in shear stress at a given normalized displacement. The slope of the linear region increases as the radial clearance decreases. And using the same offset method, all three points occur at similar locations. The values for the estimates τ_{ys} and the von Mises tensile yield stress are shown in **Table 6** below.

Table 6 - Shear and Converted von Mises Stress

Radial Clearance c (mm)	Shear Stress Intercept τ (MPa)	von Mises Tensile Stress σ (MPa)
0.05	143	253.1
0.025	144	254.9
0.01	141	249.6

A variance of 5MPa occurs between the different clearances, this can be considered within an allowable error range. This may have come from the values used to determine the slope of the linear elastic zone. The estimated tensile values from the von Mises ($\sigma=1.77\tau$) [53] criterion agree well with the 250MPa yield strength that was used in the material parameters. It can therefore be inferred that in the current setup, the clearance at these lower values does not have an impact when investigating the ShP test using the same material. The results are not clearance dependant.

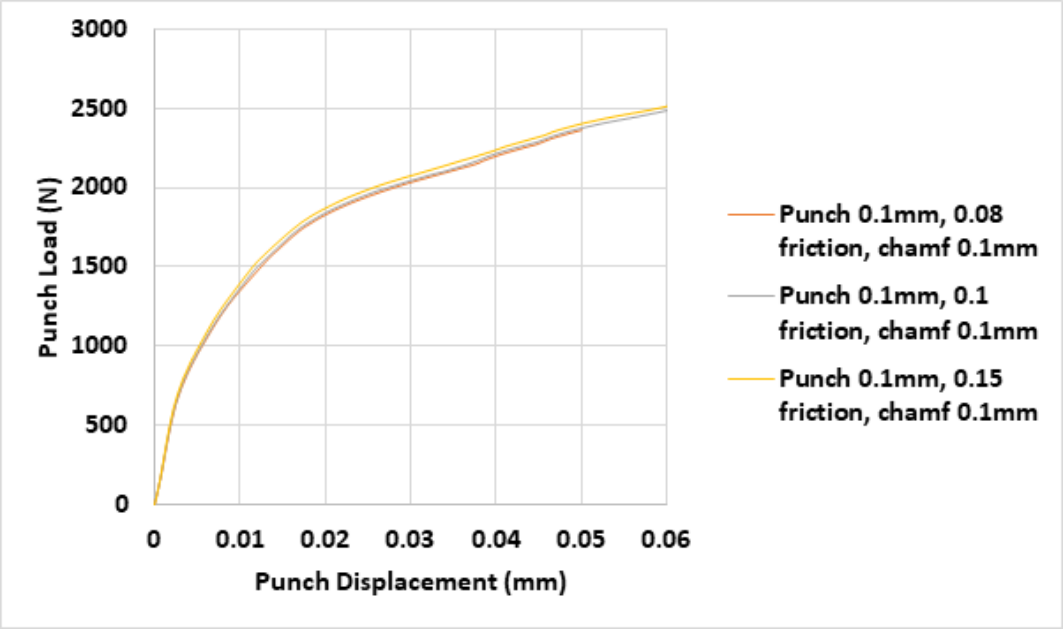

Fig. 39 – Showing the impacts of friction on the ShPT

Based on the simulation outputs from the axisymmetric modelling approach, the following results can be inferred shown in **Fig. 39**: At a punch displacement of 0.05mm with friction coefficients of 0.08, 0.1 & 0.15 are 2367N, 2364N and 2404N respectively. At a punch displacement of 0.01mm the punch loads are 1348N, 1362.5N and 1392N respectively. Whilst there are marginal increases in the punch load with increasing friction coefficient, these increases can be considered small enough not to be considered significant.

4.7 Evolution of Stress during Shear Punch Test

The below of time steps in **Fig. 40** – Evolution of stress in the sample during ShP test. Axisymmetric model with sweep applied to give a 3D view of von Mises stress evolution

These images show the distinct process of how stresses initiate and develop during the ShP test procedure. With the elements being the initial development of stress occurring on the top and bottom surfaces of the test piece at the corners of the punch and lower die. This points to the effects that clearance will have on the effective stresses within the test piece, as with a greater clearance there will be a larger volume of material than can be deformed.

4.8 Summary

While the current work cannot be directly compared and validated with equivalent experimental analysis, several conclusions can be drawn from the axisymmetric modelling work done. The information obtained serve as a guide when moving into more complex modelling work that will be done using 3D approach and the subsequent microstructure modelling. This type of research has not been previously presenting novelty and the key findings as follows; radial clearance and punch and corner lower die corner radiuses are key parameters that must be controlled when performing ShP testing.

The effects of clearance at a range from 0.01mm to 0.16mm do appear have an impact on the shear stress-normalized displacement curve. Some effects can be mitigated as the shear stress uses the averages of the radii of the punch and lower die. However, as the radial clearance inputs into the function shear stress, controlling the radial clearance is necessary for obtaining a shear dominant deformation regime. Due to the complex deformations that happen during ShP tests, bending and compression. Greater clearances will cause greater amounts of bending in the sample, reducing the amount of shear in the specimen.

The contact friction between the different surfaces does not appear to have a significant impact of the results of the ShP test in the early stages of the test. Once there is increase

in contact between the test piece and punch/lower interacting, the effects of friction become more pronounced. With an increase in the required load for the punch to drive against the test piece. Controlling the friction is necessary to closely match it with experimental setups.

Sample thickness effects were investigated. As sample thickness was increased the punch load required to achieve an equivalent displacement increased too. However, as shear stress is a function of the specimen thickness, the effects of varying thicknesses can be mitigated. Specimen thicknesses should still be maintained within permitted tolerance of 1% as set out by the CWA. Whilst in Abaqus CAE continuum material properties are assumed, there is a linear relationship between sample thickness and the peak strength. This may not be true in experimental work as the distribution of material phases may not be uniform. Resulting in spurious results that cannot considered accurate or repeatable.

Geometries will impact the output results of the ShP test. Whilst the punch radius is factored in as it is a function of the empirical conversion of punch load to shear stress, the corner tip radius of the punch and the lower die are not. It was found that having a larger or smaller corner tip radius of the punch and lower die would respectively increase or decrease the radial clearance of the ShP setup. Therefore, controlling and specifying the corner tip radius is a key factor in successful simulation of ShP tests. A smaller corner tip radium for both is preferred to decrease the effective radial clearance and maintain shear dominant deformation.

shows the evolution of von Mises stress in the ShP test in the axisymmetric modelling approach with a sweep applied around the central axis of the 2D axisymmetric model, this is to give a visualisation of the test piece as it goes through the different deformation steps. The stress starts at 0MPa and has a maximum of 0.22MPa for all six time steps, this is shown in **40 X)** of **Fig. 40**. The initial step in the model already has the punch head in contact with the test piece. In **40 a),** the punch is in contact with the top of the test piece, as it continues to drive down the first initiation points of high stress have developed around the corner tips of the punch on the top surface and the corner tip of the lower die on the bottom surface of the test piece. In **40 b)**, as the punch

continues to move further down the stresses build with the shear zone of the test piece. The growth of this stress happens from where the initial high-stress zone developed between the corners of the punch and lower die. The stress follows a path from those two points and meet in the central section of the shear zone. In **40 c)**, the stress paths have the converged with stress increasing and in **40 d)**, a 'ring-line' stress band develops along within test piece. In **40 e)**, there is an increasing deformation of the test piece with bending starting to happen on the top surface to the right of shear zone, this part is now in tension. An area of shear dominant high stress has now formed in the test piece. Finally in **40 f)**, the stresses have reached maximum just before failure. At this point cracks would start to develop, and the test piece would begin to fail. As the axisymmetric modelling was done in Implicit analysis, and advanced damage models not employed, the evaluation of failure was outside the scope of the parameter study. Damage and failure is evaluated in chapter 6 **Error! Reference source not found.**.

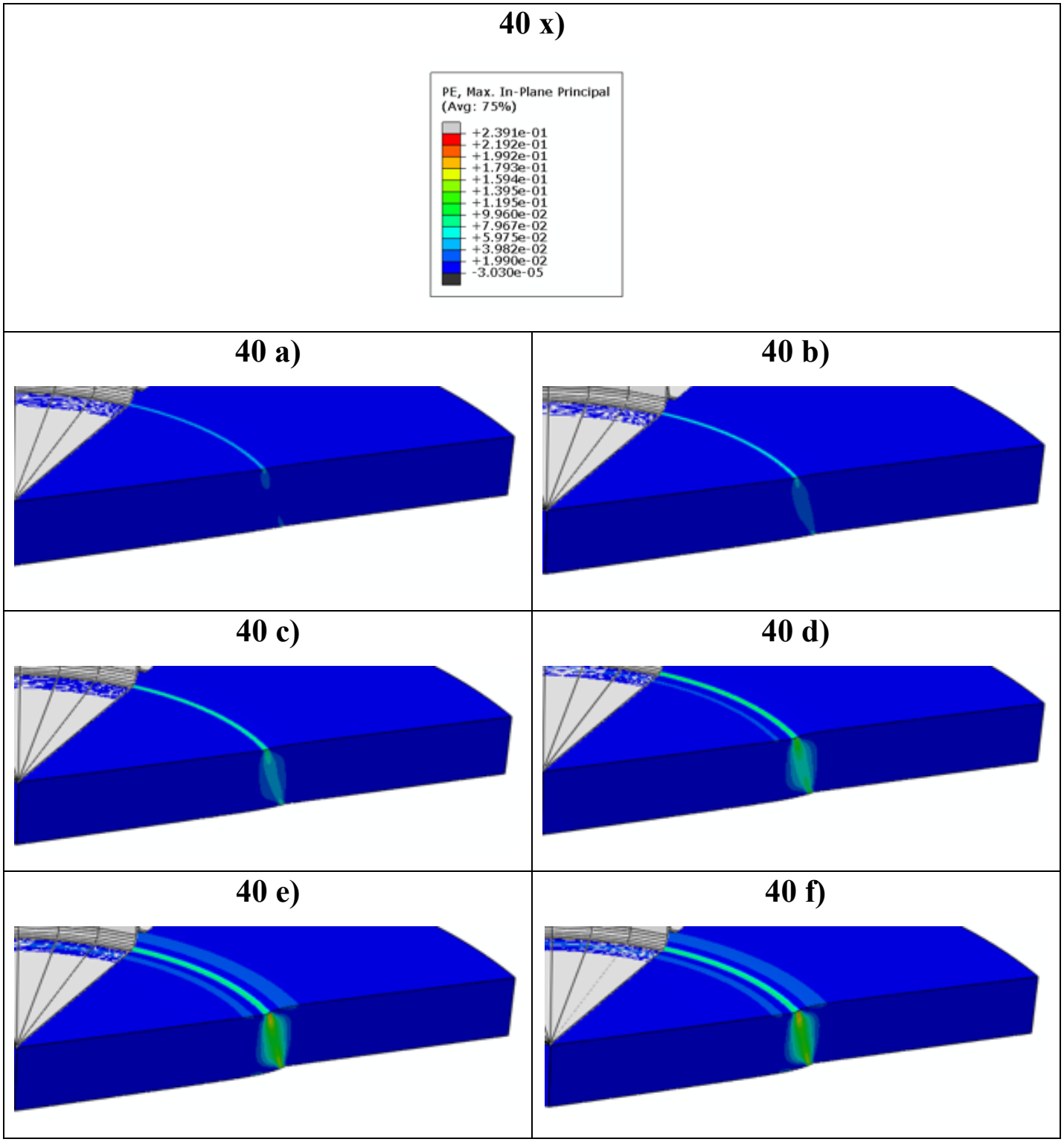

Fig. 40 – Evolution of stress in the sample during ShP test. Axisymmetric model with sweep applied to give a 3D view of von Mises stress evolution

These images show the distinct process of how stresses initiate and develop during the ShP test procedure. With the elements being the initial development of stress occurring

on the top and bottom surfaces of the test piece at the corners of the punch and lower die. This points to the effects that clearance will have on the effective stresses within the test piece, as with a greater clearance there will be a larger volume of material than can be deformed.

4.9 Summary

While the current work cannot be directly compared and validated with equivalent experimental analysis, several conclusions can be drawn from the axisymmetric modelling work done. The information obtained serve as a guide when moving into more complex modelling work that will be done using 3D approach and the subsequent microstructure modelling. This type of research has not been previously presenting novelty and the key findings as follows; radial clearance and punch and corner lower die corner radiuses are key parameters that must be controlled when performing ShP testing.

The effects of clearance at a range from 0.01mm to 0.16mm do appear have an impact on the shear stress-normalized displacement curve. Some effects can be mitigated as the shear stress uses the averages of the radii of the punch and lower die. However, as the radial clearance inputs into the function shear stress, controlling the radial clearance is necessary for obtaining a shear dominant deformation regime. Due to the complex deformations that happen during ShP tests, bending and compression. Greater clearances will cause greater amounts of bending in the sample, reducing the amount of shear in the specimen.

The contact friction between the different surfaces does not appear to have a significant impact of the results of the ShP test in the early stages of the test. Once there is increase in contact between the test piece and punch/lower interacting, the effects of friction become more pronounced. With an increase in the required load for the punch to drive against the test piece. Controlling the friction is necessary to closely match it with experimental setups.

Sample thickness effects were investigated. As sample thickness was increased the punch load required to achieve an equivalent displacement increased too. However, as

shear stress is a function of the specimen thickness, the effects of varying thicknesses can be mitigated. Specimen thicknesses should still be maintained within permitted tolerance of 1% as set out by the CWA. Whilst in Abaqus CAE continuum material properties are assumed, there is a linear relationship between sample thickness and the peak strength. This may not be true in experimental work as the distribution of material phases may not be uniform. Resulting in spurious results that cannot considered accurate or repeatable.

Geometries will impact the output results of the ShP test. Whilst the punch radius is factored in as it is a function of the empirical conversion of punch load to shear stress, the corner tip radius of the punch and the lower die are not. It was found that having a larger or smaller corner tip radius of the punch and lower die would respectively increase or decrease the radial clearance of the ShP setup. Therefore, controlling and specifying the corner tip radius is a key factor in successful simulation of ShP tests. A smaller corner tip radium for both is preferred to decrease the effective radial clearance and maintain shear dominant deformation.

5 3D Model

5.1 Introduction

This section explain how the results and findings from Chapter 4 help towards building on understanding if the ShP test and fulfilling the objectives laid out. By the end of this chapter the principles of a 3D model will have been described and discuss the difficulties in applying complex damage mechanisms to these types of punch tests for multiphase steel alloys.

5.2 Strategic Reason for going into the 3D model

As was outlined in Chapter 4 the benefits of the axisymmetric model approach is opportunity to develop models at relatively low computational cost allowing for the testing of multiple material parameters. However, for the current investigation this setup limits the detail to which ShP tests and the test piece deformation can be investigated. That being the effects of punch alignment and damage models using Explicit analysis in Abaqus. For complex damage mechanisms to be studied simulations need to be conducted in 3D.

The FE model was constructed using Abaqus 2019 [75] using standard/explicit model. The model has a half symmetry along its z-axis, as can be seen in **Fig. 41**, this is to limit the size of the overall model without losing the ability to perform the desired study. There are four components in the model setup; Punch, Test Piece, Upper and Lower Die. The test piece is modelled as a deformable elastic-plastic part. The punch, upper and lower dies are modelled as analytical rigid shells with strait and curved segments. The disc has a radius of 4mm with thickness of 0.5mm. The test piece is considered to have uniform material properties throughout (anisotropy is neglected in the material parameters). The punch has a radius of 1.95mm with a corner tip radius of 0.1mm (100µm). The radius of the receiving hole in the lower die is 2mm also with a corner tip radius of 0.1mm (100µm). This gives a clearance of 0.05mm (50µm). The upper die and lower die both have the similar dimensions but the top die having a corner tip radius of 0.2mm (200µm). The contact surfaces are defined as follows; The punch, upper and lower dies are master surfaces with the upper and lower surfaces of

the test piece defined as slave surfaces. To simulate the effects of friction that exists in the experimental setup a penalty of $\mu = 0.1$ is applied to all the contact surfaces. This simulates the contact of steel on steel that is under partial lubrication and is used as a parameter for different levels of roughness. This is a value that has been used by other researchers [20,151] when investigating SPT.

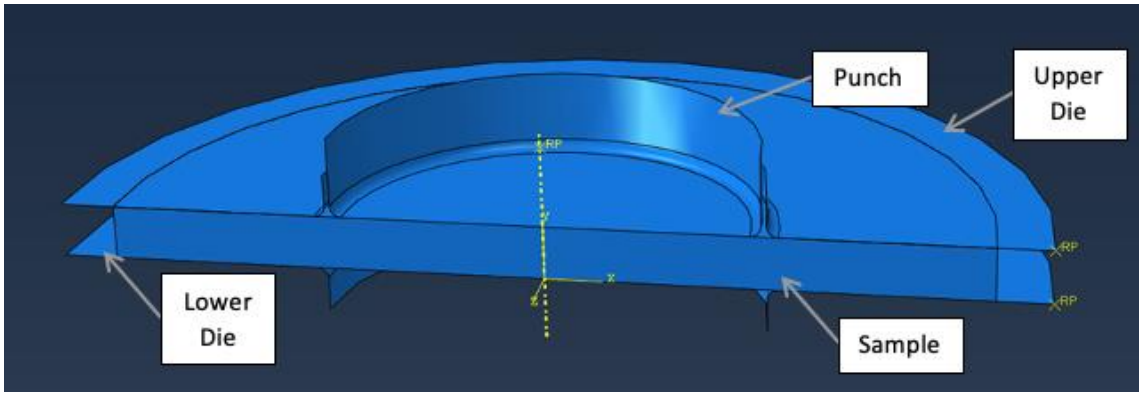

Fig. 41 – Assembly of the 1/2 symmetry FE ShP Test model

5.3 Constructing the Parts

All parts in the model were constructed individually with their geometries shown below. The model consists of four parts, 1) Punch, 3) Clamp, 3) Die & 4) Disc.

5.3.1 Punch

Fig. 42 shows the punch was prescribed a radius of 1.2mm with a corner tip curve of 0.05mm, following a similar approach to Guduru et al [43] and was assigned as an analytical rigid shell. A reference point was added in the centre of the punch which will be used when applying the boundary conditions. The punch was generated using a revolution function, but a partition was applied along the centre line for an easier navigation of the assembly.

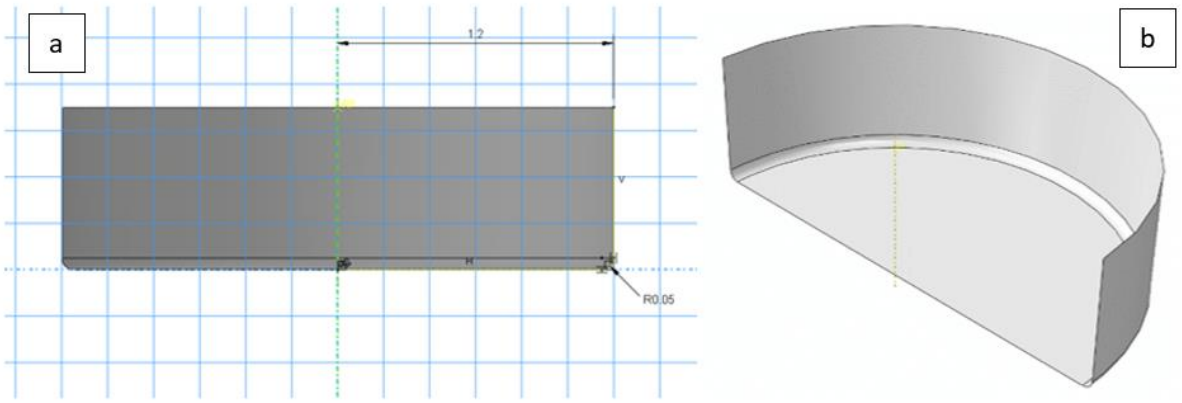

Fig. 42 – a) Diagram showing a schematic of the punch and b) the 3D analytical revolution with partition

5.3.2 Clamp

Fig. 43 shows the clamp with an internal receiver radius of 1.26mm, a height 0.35mm and a corner tip radius of 0.1mm. As mentioned previously the corner radius of the clamp does not impact the deformation response of the disc. The total radius of the clamp is 4.45mm from the centre to the outer edge, this is to make sure that the entire top surface of the disc is covered during a simulation. The clamp too was partitioned along the centreline for easier navigation of the assembly. A reference point was added to the outer of the clamp.

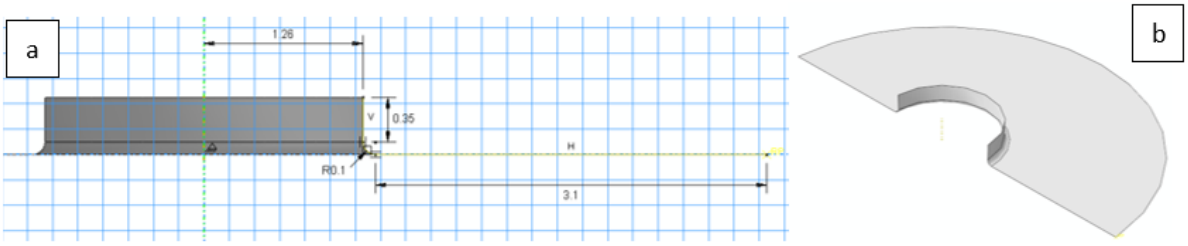

Fig. 43 – a) Diagram schematic of the clamp and b) 3D analytical revolution with partition

5.3.3 Die

Fig. 44 show the die with a receiver radius of 1.25mm with a corner tip radius of 0.05mm. The total radius of the clamp is 4.45mm, this is to ensure that the lower surface of the disc is entirely covered during a simulation. The die is assigned as an analytical rigid surface with deformation possible. A reference point is added to the

outer edge of the die to apply boundary conditions later. The die was partitioned along the centreline for easier navigation of the assembly.

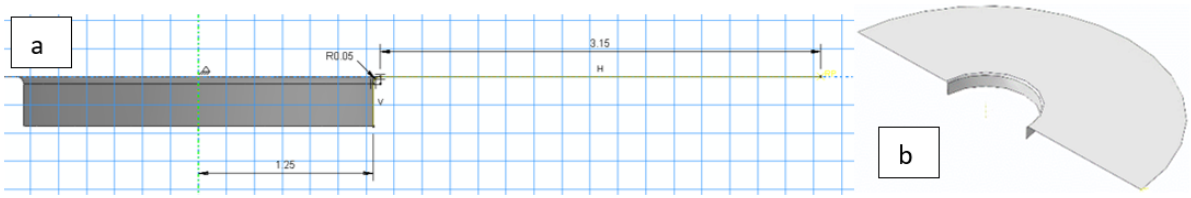

Fig. 44 – a) Diagram schematic of the die and b) 3D analytical revolution with partition

5.3.4 Disc

The disc was modelled as a deformable homogenous solid and was generated by solid extrusion. The disc has a radius of 4mm, this follows the ASTM standard for SP testing [93]. The disc was partitioned into 5 zones. The middle zone being the shear zone, either side of it being two transitions zone and outside of those being a free zone. This was done to the disc for the creation of a structured mesh to optimize the run speed without having to sacrifice output from the simulation. This can be seen in **Fig. 45** a & b.

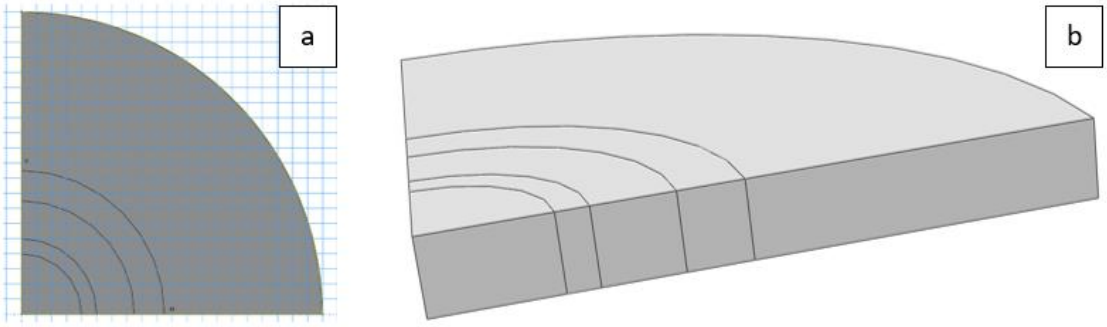

Fig. 45 – a) Schematic of the disc and b) 3D analytical part with partition

Fig. 46 shows the cross sectional a 2D cross sectional schematic of the disc.

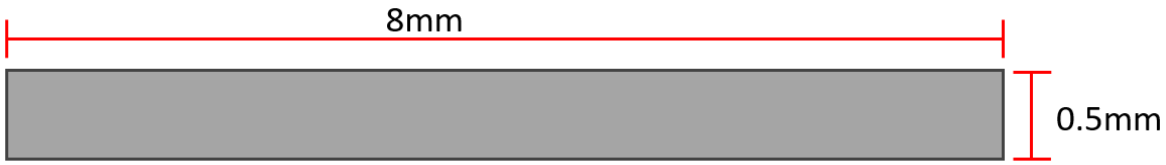

Fig. 46 – 2D schematic of the disc

5.3.5 Half-Symmetry & Quarter Symmetry

Fig. 47 and **Fig. 48** shows a blown image of the final assemblies for the half- and quarter-symmetry approaches.

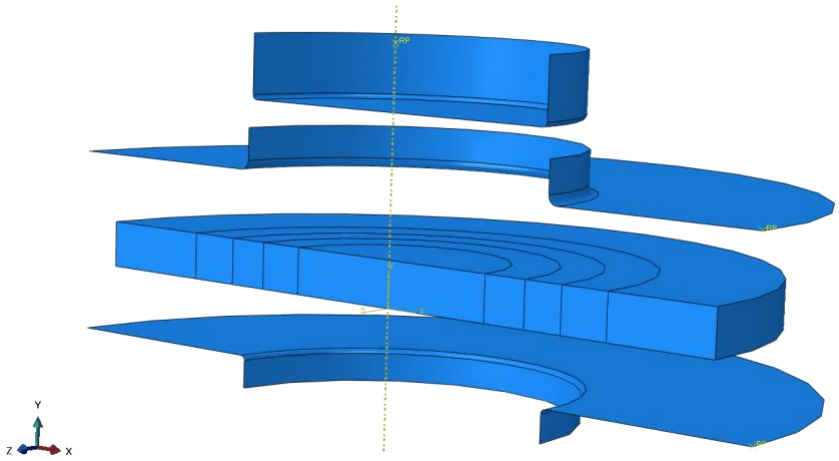

Fig. 47 – Blown-Up Schematic of the assembly for half symmetry test piece

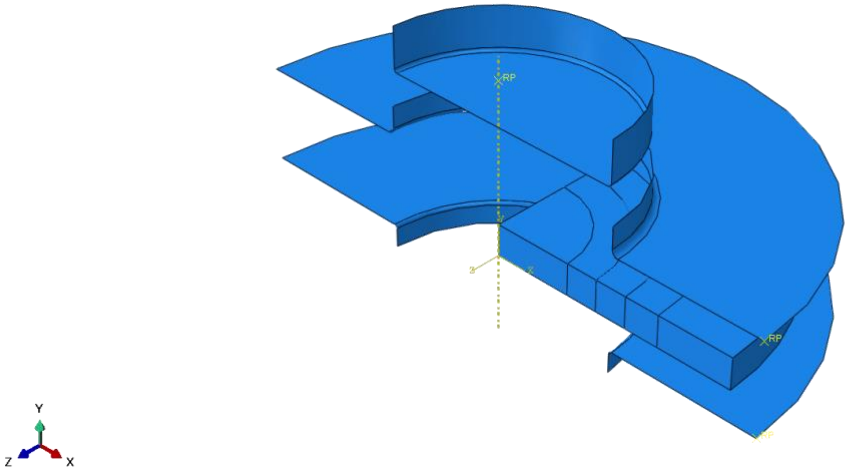

Fig. 48 – Blown-Up Schematic of the assembly for quarter symmetry

5.3.6 Mesh

A structured mesh has been applied to the test piece in the model setup. A fine mesh is used in the clearance/shear zone with square elements with lengths of 25µm on the edges. As the width of the shear zone is 0.45mm wide in the current setup. A coarser mesh is used throughout the rest of the test piece, this can be seen in **Fig. 49** and **Fig. 50** below which shows a setup for the half-symmetry and quarter-symmetry respectively. The coarse meshing region uses quad-dominant elements with the clearance/shear zone using quad elements, this can be seen in **Fig. 49**. A mesh sensitivity study has not yet been performed. It can already be considered that the mesh regions outside shear zone will not have an impact on the output of the FEA model. This is due to the deformation induced stress being concentrated around a radial perimeter that occurs between the punch corner edge and bore hole. An analysis was performed to make sure that the results are not mesh dependant. The upper and lower die are fixed into position and prevented from any movement. The punch moves -0.1mm in the y-axis and fixed along the z- and x-axis. The movement is limited as the shear yield point is the main point of interested in the study. Therefore, the punch displacement in this model does not continue up to the point of cracking and failure. The test piece is allowed to move freely (not fixed) apart from in the z-axis. This is to prevent bulging along the cut and recreate the full setup. No clamping forces are applied between the contact surfaces of the test piece and upper and lower dies.

C3D8R (8-node linear brick element, reduced integration, hourglass control) was chosen for the entire disc. Mesh size varied within the part depending on where deformation would occur within the sample this can be seen in **Fig. 49** and **Fig. 50** for half- and quarter symmetries respectively. The disc was divided into 5 parts. Starting from the centre; 1) a free mesh was applied using an approximate element size of 0.2 2) Next follows a transition zone between the free mesh and the shear-zone, a bias was applied to this region going from a 0.1 to a 0.03 element size. This is to create a mesh that becomes finer as it moves to the shear-zone. 3) In shear-zone, along the face of the disc a structured mesh with an element size of 0.01 was applied. This was taken to be the optimum compromise of obtaining a fine enough mesh that can capture the deformation around the corners of the punch and die. 4) Is a second transition zone. This again has a biased mesh applied to it with a finer mesh closer to the shea-zone with elements getting larger as they move away from the shear-zone. 5) The outer zone is a free mesh with an approximate element size of 0.2 applied.

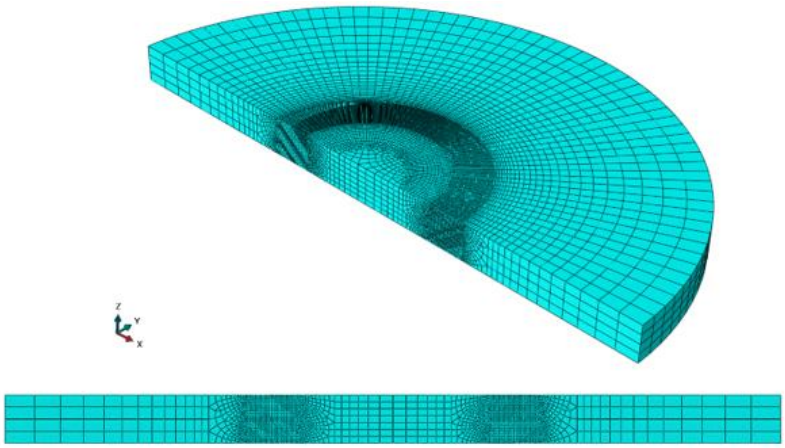

Fig. 49 – Half Symmetry Mesh, overall view and view along the x-axis

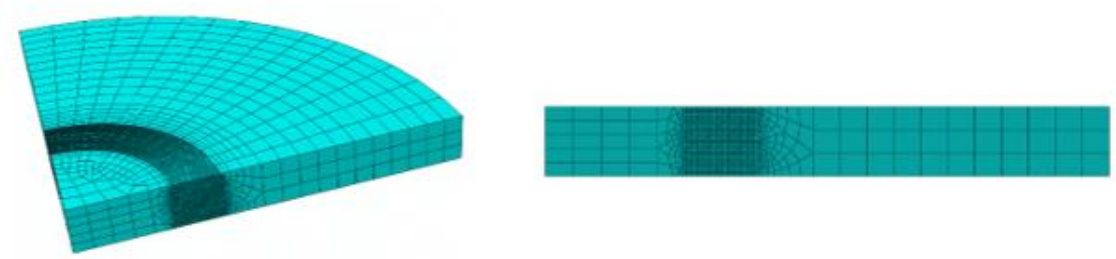

Fig. 50 – Quarter Disc Mesh, overall view and view along the x-axis

Element deletion was activated for all elements in the sample disc, the parameters for which are based on the material properties described in the next section.

5.4 Material Properties

Material Properties were obtained from material produced in the MACH1 Lab at Swansea University. Data was obtained using standard tensile testing from which the following results were obtained in **Fig. 51**, the tensile testing was performed by researchers in the MACH1 Lab. This data served as the primary source for obtaining the Young's Modulus (E), Poisson Ratio (ε) and the Plastic Stress Strain Curve.

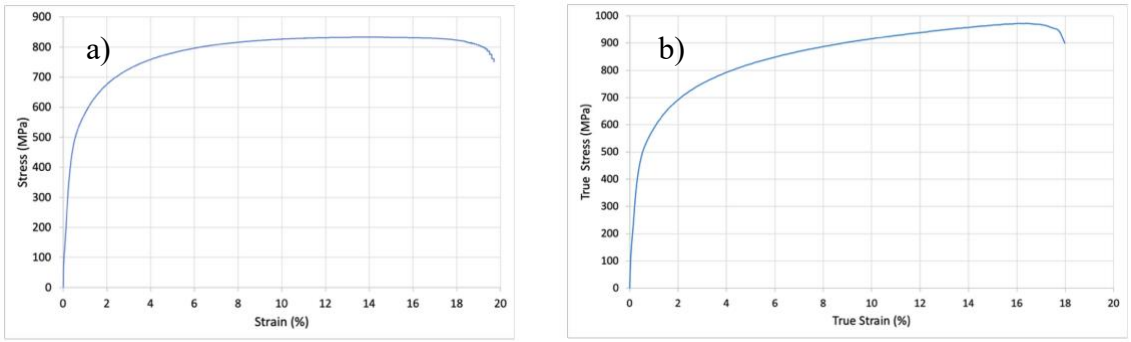

Fig. 51 – a) DP800 Engineering MACH1 Data b) DP800 True Stress Strain

The Engineering Stress-Strain was used to obtain the Plastic Stress-Strain. A Johnson-Cook plasticity regime was obtained through comparative iterative analysis. A B n parameters were altered until the graph obtained from those factors closely matched that from the tensile test. This produced a graph where the stress values would correlate with prescribes strain values with ±2% variation from the true stress value. The final

material parameters are shown in tabular form in **Table 7** which was also used in the prior 2D axisymmetric modelling but with added material damage mechanisms.

Table 7 - DP800 Material Properties used from the axisymmetric modelling approach

Property	**Value**
Material Density (Tonne/mm^3)	7.87E-09
Young's Modulus (MPa)	207,000
Poisson's Ratio	0.29
Ductile Damage	Fracture Strain = 0.18 Stress Triaxiality = 0 Strain Rate = 0
Damage Evolution	Displacement at Failure = 0.11 (mm)
Johnson-Cook Plasticity	A = 250 MPa B = 1136.14 n = 0.2244

5.4.1 Time Step & Mass Scaling

A time step of 90 seconds was used for a 0.3mm punch displacement. This is based on the experimental setup which uses a punch velocity of 0.2mm/min (0.00333mm/sec) and breakage occurred at around 0.25mm deflection.

As explicit analysis can take a long time to run with the number of time increments needed running into the 100s of 1,000s. The stable time increment Δt is dependent on the shortest element length L_e and the wave dilatational speed c_d of the material, for steel this ≈ 3000m/s [152] and is expressed as from the Abaqus user manual [75]:

$$\Delta t = \frac{L_e}{c_d} \tag{11}$$

c_d is dependent on the Young's Modulus and the material density, expressed as:

$$c_d = \sqrt{\frac{E}{\rho}} \tag{12}$$

In Abaqus it is possible to reduce the computation time needed without sacrificing accuracy by using mass scaling. This increases the effective density of the material and reducing the dilatational wave speed. This allows for a larger stable increment to be used, reducing the total number of increments need and allowing an explicit analysis to run more efficiently. However, by increasing the density of the material being modelled this will also increase the effective inertia. In cases analysis where large velocities are simulated or if too much mass scaling is applied, this can lead to erroneous solutions. Mass scaling is appropriate if the system kinetic energy and the internal energy need to be considered. If the internal energy of the system is greater than the total kinetic energy, then the simulation can be considered quasi-static.

5.5 Boundary Conditions

Fig. 52 shows the final boundary conditions applied to the test piece, punch and holder. The boundary conditions define how much freedom of movement the model assembly is allowed to have during the deformation process. The aim is to replicate the conditions experienced during a ShP test, with movement allowed in certain directions but restricted in others. These conditions are outlined below for the holders, punch and test piece. The image shows the combined boundary conditions for the assembly, with further detail for each component described in the following sections. A half symmetry was employed with a cut along y-axis. A quarter symmetry with a cut along the y- and z-axis was also considered. However, it was decided not to pursue this due to add the complexity needed for the movement restriction of the deformable solid. In addition to this was the question of if the stress/strain state in the disc would still be accurate. The deformable disc was also partitioned to allow higher mesh densities in high deformation areas whilst a coarser mesh was applied in areas of low stress and strain. This is to reduce the total computation time required.

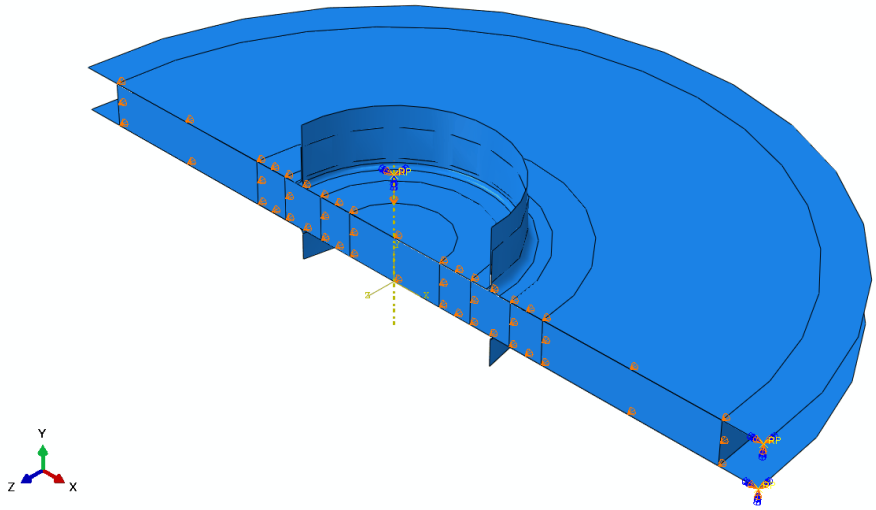

Fig. 52 – Boundary Conditions for the ShP Test Assembly

5.5.1 Boundary Conditions for Top and Bottom Clamp

The clamp and lower die are fixed in place, for this an ENCASTRE condition is applied to a reference point (RP) that is paired to component geometry. Fixing them in place and not permitting any displacement or rotation. This effectively removes any compliance that would be present during experimental testing. With some deformation in the testing rig expected. This is discussed further in the results section.

5.5.2 Boundary Conditions for Half Symmetry

With the current setup consisting of a half model, it is necessary to apply appropriate boundary conditions to the exposed section of the test piece. Without such conditions, it is expected that the exposed surface would bulge outwards, whereas this would normally be constrained. In the assembly the cut side is facing in the x-axis, a displacement restriction was applied in the x-direction, with nodes still allowed to move freely in the y- and z-axis, and the elements allowed to rotate freely.

5.5.3 Punch Displacement

A punch displacement boundary was applied to a reference point. Displacement was only permitted along the y-axis with all other displacements and rotations set to zero. A tabular amplitude was applied for a constant displacement rate at the punch with a time at the start of the model having 0 amplitude. Once the punch has completed its time step 90 seconds will have passed and when the sample should have failed, at this

point the maximum amplitude of 1 will have been reached. This is shown in **Table 8** below:

Table 8 – Punch Displacement Rate

Time/Frequency	Amplitude
0	0
90	1

5.5.4 Output Requests

For appropriate output data to be obtained, they must first be specified in the Field Output Request manager during the 'Step' stage in the Abaqus model tree. For the current simulations the following outputs were chosen:

- S; records all of stress components in the simulation, the main one being the von Mises stress.
- PE; records all the plastic strain components in the simulations.
- PEEQ; records the equivalent plastic strain. This is needed to review the sample's inelastic deformation. This will also show where the sample may be likely to fail.
- U; records the deformation in the x-, y, and z-axis
- RT; records the reaction forces for all parts. This is needed to obtain XY data for the force-displacement plots.
- SATUS; records that status of an element. Going from 1.0 to 0.0, showing if the element is active or inactive respectively. This is needed for element deletion to be active.
- SDEG; records the scaler stiffness degradation, used to measure element deletion.

5.6 Results

Once the simulation finished results are be obtained from the .odb file. Desired data such as the punch load, punch displacement and sample deflection can be obtained. These are necessary when wanting to replicate the force/displacement curves and from

which the Shear Force/Normalized Displacement curves can be obtained. The results can also be analysed visually to investigate the propagation of stress and strain during the deformation process as well as the areas where stresses are concentrated in the sample and where subsequent failure occurs.

5.6.1 Mesh Sensitivity & Corner Tip Radius

One of the main questions when performing any FEM study is whether the mesh density applied is close to the true numerical solution. For linear-elastic deformation this is less of a concern when compared plastic deformation. A mesh sensitivity analysis was done in the shear zone shown. **Fig. 53** taken form the axisymmetric work shows how small the primary deformation area is being only 400µm wide meaning that only a relatively small area requires this higher mesh density. **Fig. 54** shows a cross section of the final 3D model with its mesh applied. It can be seen that a free mesh needs to be applied in the areas adjacent of the shear zone to obtain the fine structured mesh. **Fig. 55** shows the different outputs at different mesh densities, what can be seen is that no major difference for the initial modelling could be seen. A medium mesh was still chosen as during the advanced modelling when element deletion takes place it

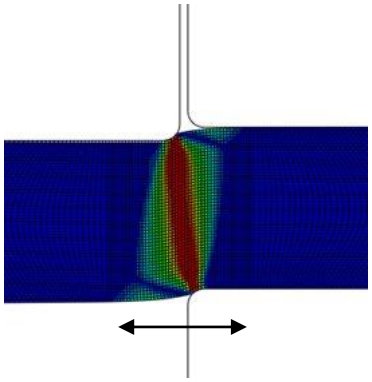

Fig. 53 – Cross section of Shear zone of Shear Punch Test. This shows development of von Mises stress and that peak stress is at the corners of the punch tip and lower die

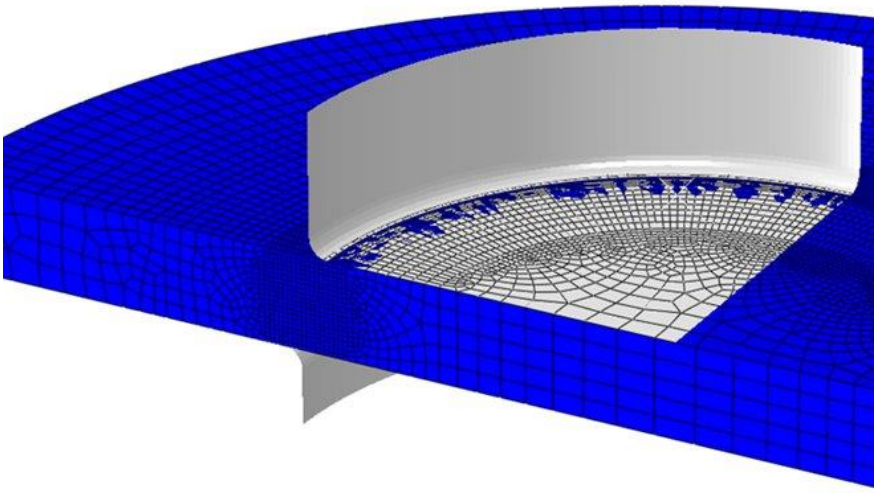

Fig. 54 – Section of 3D assembly Shear Punch Test

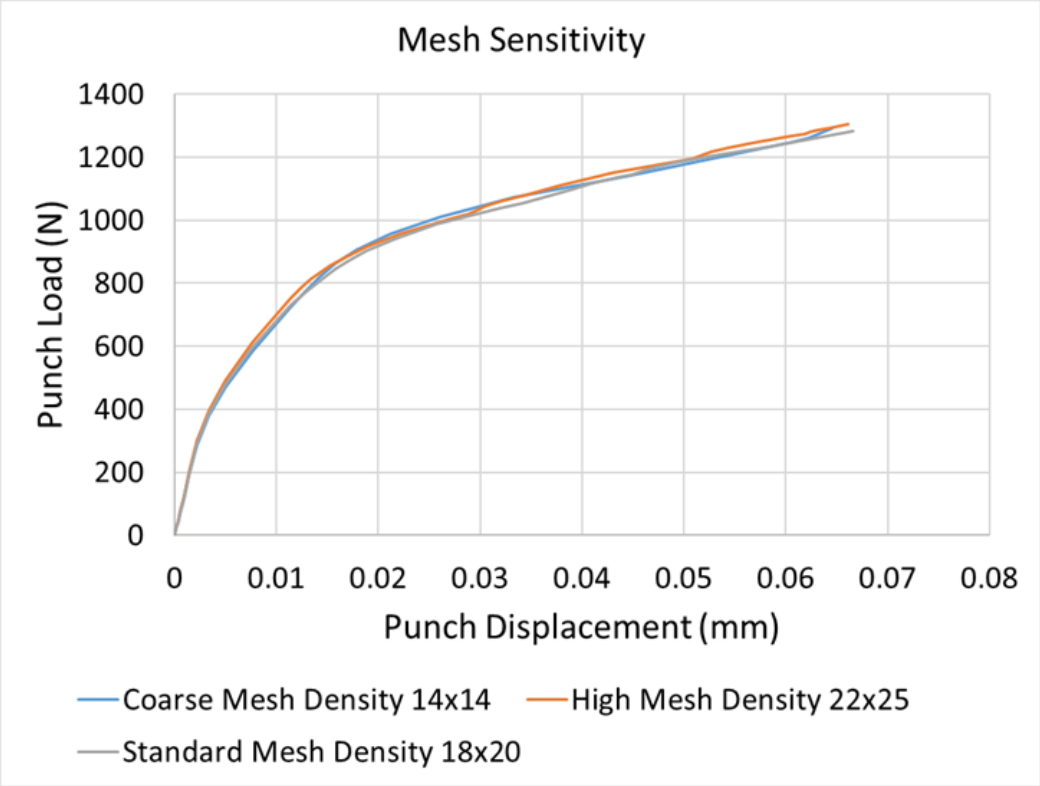

Fig. 55 – Effects of mesh density in the shear zone on the output results of the 3D model of ShP test

5.6.2 Simulation Outputs

The image below shows two steps during the ShP test simulation. **Fig. 56** a) shows the simulation roughly 15 seconds in, a radial stress zone has formed at the interspace between the punch and the lower die, clearance zone. Image b) is at 81 seconds into the simulation, by this point the sample has failed with the elements that have reached the failure criterion having been automatically deleted. These images can be used to validate some of the initial set-up parameters in the model. Making sure that the model is deforming correctly.

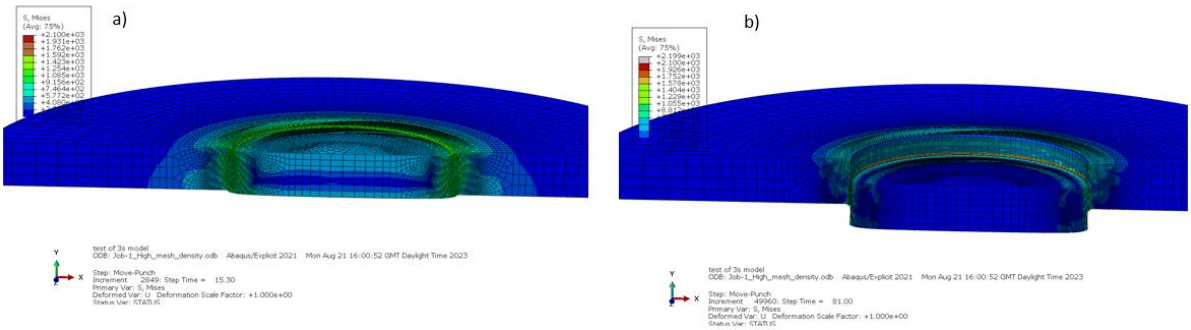

Fig. 56 – a) Sample Disc at 15sec, b) Sample at 81sec this having failed.

XY data still needs to be obtained and compared with results from the experimental results. This is to ensure that the material parameters, specifically damage, are within the same orders of magnitude.

The outputs from the ShP 3D simulation test were compared to the experimental ShP test. **Fig. 57** shows the comparison of results between the experimental results and modelling results. Whilst the magnitude of the force values for both peak strength and yield strength show good alignment, the elongation values up to failure are do not follow closely to the experimental results. Results from the experimental work shows DP800 reaching the UTS value between 0.16mm and 0.18mm sample deflection and failing at between 0.18mm and 0.22mm. By comparison in the simulation results the UTS point is reached at 0.18mm, similar to the higher value for the experimental ShP test results, but this peak is maintained longer in the simulation ShP test than in the experimental ShP test with the sample strength starting to drop at 0.21mm before then failing at 0.27mm. which corresponds to the failure point at 81sec from **Fig. 57**. Much work was done modifying the strain and failure parameters for the material properties. However, this resulted in material properties that would no longer be valid for other tests modelled in Abaqus.

What can also be seen on **Fig. 57** are ripples in the force displacement curve once the simulation enters the non-linear plastic deformation stage. These ripples are likely caused by node snagging due to secondary sliding along the node surface. Normally during node-to-node discretization small corners or protrusions are allowed to penetrate the spaces between nodes of a smooth surface. During punch displacement processes nodes can get caught between these spaces, preventing desired deformation

path of the of the material sample. The main surface contact is usually smoothed out to minimize this phenomenon. However, this process does not work where there are major issues with the geometric interactions between the teat piece and the punch head. For the setup here, where the punch head and lower die have corner tip radiuses of 5µm and even with a mesh node distance of 1µm, due to the relatively large deformation that occurs in the sample there was node sliding between the punch and top surface of the sample. As the punch kept moving downwards against the top surface of the test piece, this generates large amounts of sliding in the sample. As this sliding occurs the nodes on the top get caught along the punch corner, this increases the relative force required for the punch to continue moving downwards. Eventually, the node then slides off around the punch, this results in a corresponding drop in the force required in the punch to cause further deformation. The sample then continues along its same relative force-displacement curve. The process repeats itself during the entirety of the deformation process until failure criterion is reached, at which point elements are deleted. Causing the ripples in the deformation curve of the simulation results when compared to the experimental curves in **Fig. 57**7 below.

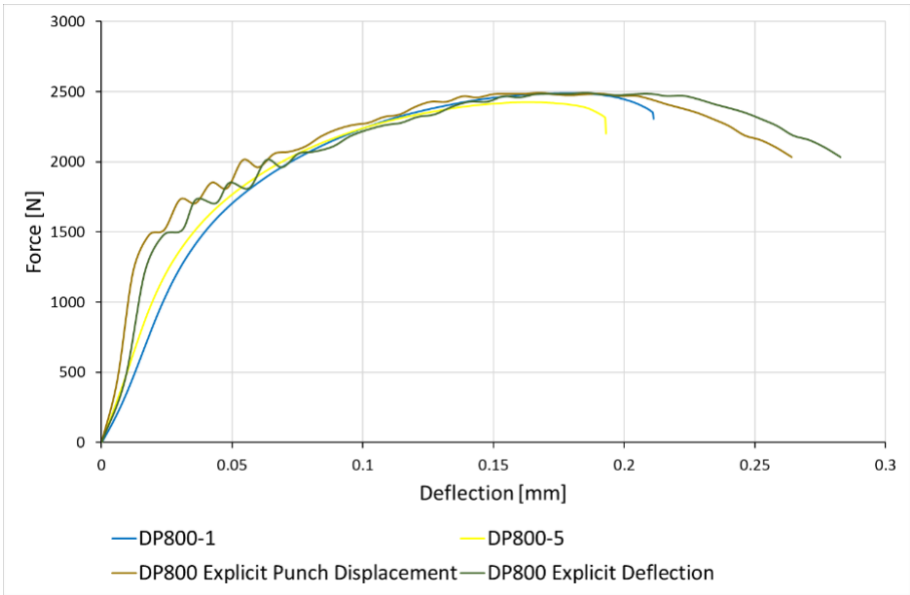

Fig. 57 – Force deflection curve of 3D shear punch test, different modelling approaches compared with experimental testing

5.6.3 Assembly Stiffness

It is known from SP testing and ShP testing that assembly interactions need to be accounted for when performing such tests. It is for this reason that deflection at the bottom of the sample is measured rather than the punch displacement [15,17,27]. This to ensure that what is being measured are the impacts of the punch on the sample rather than minor amounts of deflection in the test piece. One of the questions that arises is if the effects this known phenomenon in an experimental process also occur in a simulation process of the same test. In the simulation setup chosen for this thesis, the punch and clamping surfaces were modelled as analytically rigid surfaces, meaning there would be no bending of these parts. This eliminates the suspected compliance effects on the ShP test output. Compliance effects would manifest in the outputs of the force-displacement curve being right-shifted and the test piece having a lower Young's Modulus and therefore being a less stiff material than it would be in reality. However, there might still be some other unknown effects taking place which would impact the output in the load deformation curve. This could be bending or stretching of the sample. For this, displacement was measured at both the punch and at the bottom central node of the test piece.

Fig. 58 shows the difference between measuring displacement from using a reference point at the punch end vs measuring deflection at the bottom of the sample. The load is the same for both curves as the load was measured at the punch head, the same as in standard experimental ShP test [44,57]. The difference in the curves shows that when measuring the displacement of the punch there is less displacement for a given punch load when compared to measuring deflection at the bottom of the test piece, differences in these results was not expected. This suggests that there is more deformation manifesting which is being measured at the bottom of the sample than what is being measured at top by the punch end. This suggests that even with the tight radial clearance between the punch and die holes there is some small amount of bending going on in the test piece. This causes the bottom to the bow outward which result in a higher test piece deflection than what is measured from the punch head alone. So far, this has not been discussed by other authors. There may also be some compressing happening to the test piece at the top of the surface before the entire sample begins to

deflect. The sample therefore is indented at the beginning stages of the ShP test before the remaining elements start to deform.

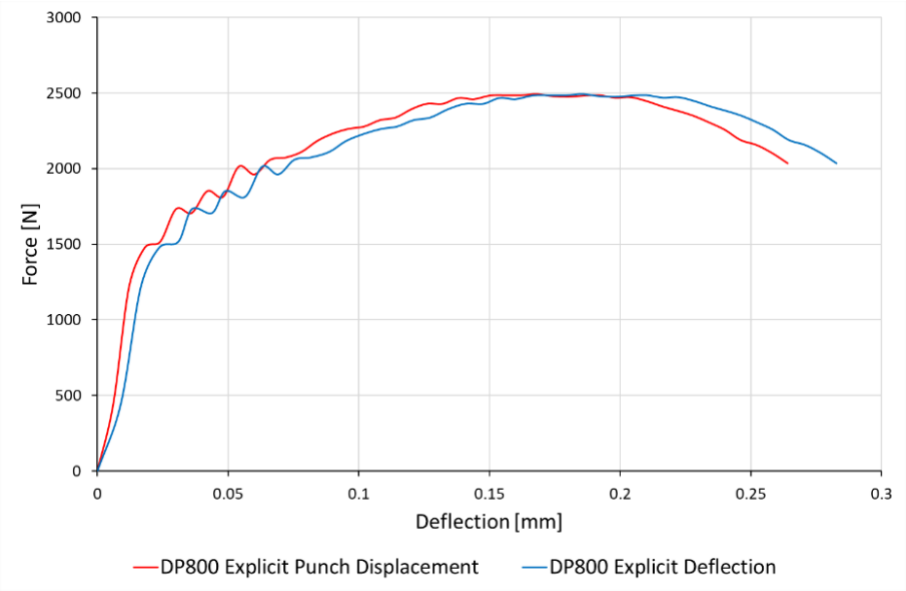

Fig. 58 – Difference of results from measuring displacement at the punch compared to the deflection measured at the bottom of the sample

5.7 Summary

In this chapter, a 3D half-symmetry model was generated to evaluate damage in the in ShP test of a DP800 alloy which could not be done in 2D axisymmetric tests. Whilst strength values showed a good correlation compared to experimental test results, the modelling showed the difficulty in producing reliable output for material elongation in. This could not be resolved in the time for this thesis, but suggests that additional deformation mechanisms are still happing which cannot be simulated using continuous material properties alone and that the different microstructural properties of both the ferrite and martensite must be considered when wanting to evaluate damage. Node snagging was also evaluated as an impact on the ripples present in the load deformation curves and the challenges in simulating this type of test when small geometries are involved at the punch corner. Lastly, a comparison of measuring the punch displacement and the sample deflection at the bottom was performed. This showed that even though only the test piece was deformable there was still a difference in the displacement and deflection values. Suggesting that there is deformation at the top of

the test piece which is not measured when only using deflection values from the bottom. This has not been found in literature or commented on by other authors.

6 Microscale Modelling of Dual Phase Steel

6.1 Introduction

This chapter explores the microscale modelling approaches for DP steels via the RVE method. RVEs are used to evaluate microstructural deformation of different materials, particularly when deformation is expected to be inhomogeneous. This is particularly relevant for DP steels undergoing ShP testing where scaling effects mean than a small area undergoes deformation whilst the microstructure remains constant. To measure deformation of DP microstructure requires the development of a model that evaluates the onset and evolution of damage in DP steel and quantify the effects of the microstructural components on the global macrostructure. This is particularly relevant where complexities in the 3D model could not be resolved from Chapter 5. To achieve first requires the setting the right boundary conditions for a RVE using the micrograph of a real DP steel. This can then be followed by development of a model which generates DP RVEs synthetically allowing the user to evaluate specific parameters themselves rather than having to always rely of actual microstructures. Lastly, an attempt at developing a 3D RVE was done to evaluate through thickness effects of martensite reinforcements.

6.2 Material Properties, Constitutive Description

Materials properties for both the ferrite and martensite phases is needed for development the RVE model. Researchers have obtained those values through single phase tensile analysis [153], this is done by testing two specimens where a ferrite specimen was hardened to be pure martensite and the unhardened specimen being ferrite-pearlite. From there testing can be one on two materials that came from the same initial production batch. Another method has been performing nano indentation tests of a DP alloy [154]. Sections of DP steel are tested using an indenter on each of the phases to obtain strength properties of the ferrite and martensite. Laboratory testing of each of the material properties was outside the scope of this thesis. Material properties for ferrite and martensite were therefore obtained from literature. The elastic

materials properties for ferrite and martensite have been obtained from [155] and [153] and shown in **Table 9**.

Table 9 – Elastic Properties for Ferrite and Martensite

Phase	Young's Modulus E (MPa)	Poisson's Ratio (V)
Ferrite	203,500	0.292
Martensite	209,000	0.289

Obtaining the flow curve properties of the individual ferrite and martensite experiment by is difficult. A dislocation density-based strain hardening model was used to quantify the plastic flow curves for martensite. These are based on empirical relations first proposed by Rodrigues [156] but have since been used by other authors [118] and are shown in **Equation 13** and **Equation 14**:

$$\boldsymbol{\sigma = \sigma_0 + \Delta\sigma + \alpha \cdot M \cdot \mu \cdot \sqrt{b} \cdot \sqrt{\frac{1 - \exp(-M \cdot k \cdot \varepsilon)}{k \cdot L}}} \quad \textbf{(13)}$$

$$\boldsymbol{\sigma_0 = 77 + 750(\%P) + 60(\%Si) + 80(\%Cu) + 45(\%Ni) + 60(\%Cr) + 80(\%Mn) + 11(\%Mo) + 50(\%Nss)} \quad \textbf{(14)}$$

Where σ is flow stress of the material, σ_0 is the Peierls stress [157] and solid solution hardening effect from alloying elements, $\Delta\sigma$ is the strengthening by precipitation of carbon content in each phase, α is a given constant, M is the Taylor Factor, μ is the shear modulus, b is the magnitude of the Burger's Vector, k is the recovery rate and L is dislocation mean free path. The coefficient values for the different constituent phases are shown in **Table 10** below.

Table 10 – Hardening Coefficients for DP800 *[118]*

Steel	Phase	σ_0	$\Delta\sigma$	α	M	μ	b	k	L
DP800	Ferrite	131.23	244.52	0.33	3	80000	2.5E-10	3 .333333	0.000003
	Martensite	758.51	244.52	0.33	3	80000	2.5E-10	25	0.0000002

The individual phases are further strengthened by the addition of alloying elements; this is included in the constitutive equations. The %wt of alloying components is shown in **Table 11** and used for Δσ.

Table 11 – DP800 Chemical composition from Mach 1 Lab at Swansea University

	C	Si	Mn	P	S	Ni	Cu	Cr
DP800	0.136	0.249	1.77	0.011	0.0027	0.018	0.024	0.558

These alloying components are based on DP800 material that was tested at Swansea University and obtained in [140][10]. It should be noted that some alloying elements such Mn are included in the constitutive equations but were not included as alloying elements for this DP800 alloy. Additionally, the DP800 material as whole had wt% of alloying composition provided for both the ferrite and martensite phase combined rather than for the phases individually. Carbon alloying content for the ferrite phase and martensite were therefore both used as equal values in the solid solution hardening component of the DP800. The flow the curves for both phases are shown in **Fig. 59** below:

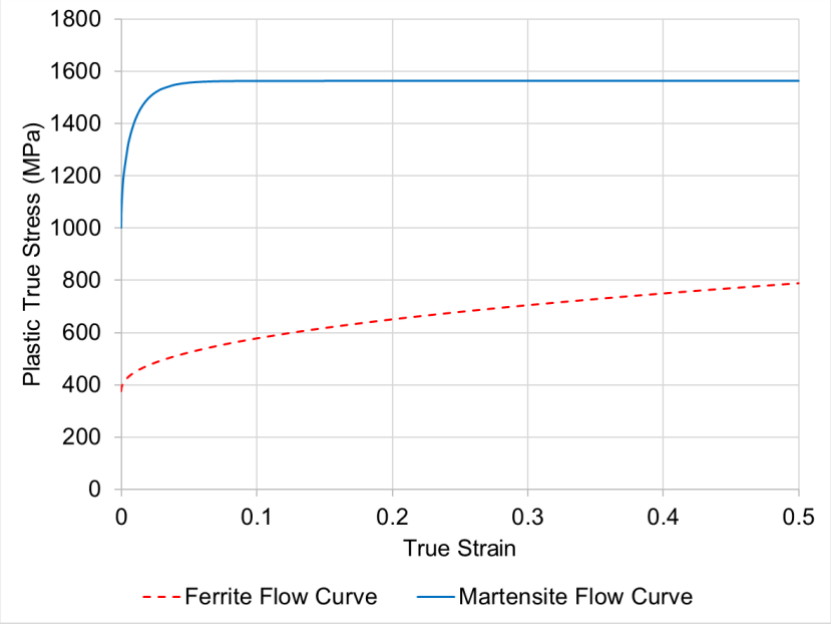

Fig. 59 – Plastic Flow curves for ferrite and martensite

The density for both phases was assumed to be the same with a figure of 7.9E-9 Tonne/mm^3, the same for a typical steel grade.

6.3 2D Microstructure Modelling of a Dual Phase Steel

6.3.1 Real Microstructure RVE

Further modelling was performed on a genuine DP800 microstructure, using an image captured from a light-microscope. This is to evaluate the modelling approached used for the RVE, specifically the application of boundary and loading conditions. Using a real microstructure should generate results that are replicable of real-world testing for a DP steel undergoing a tensile test. Results from the RVE should follow closely to actual tensile tests and provide validation that this approach is valid for microstructural modelling of DP steels.

A micrograph image of DP800 is shown below in **Fig. 60**. This was as the basis for developing a 2D RVE that could be imported into Abaqus.

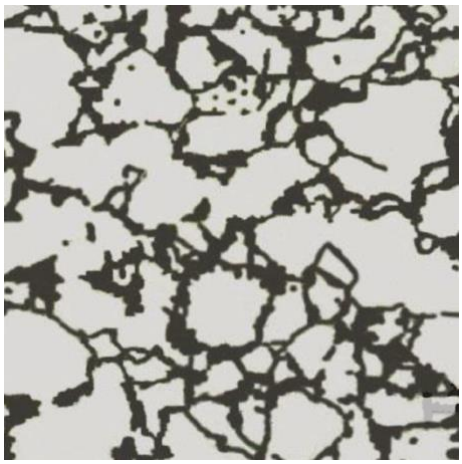

Fig. 60 – DP800 alloy with 30% Martensite content

This image was modified into a file format that was importable into Abaqus, this required reducing the effective resolution of the image and removing specific small features of the actual micrograph. This is to ensure that the image can be imported and correctly meshed without having convergence issues.

6.3.2 Applying Material Properties

Material properties had to be applied manually in this process, as with the artificially generated microstructure no preferred crystal orientation was applied to the model.

The finalised RVE with material properties applied in shown in **Fig. 611** below. The Ferrite is shown as the darker green colour with martensite in the lighter grey colour. In this it shows that ferrite is randomly distributed with a large variety in the overall size.

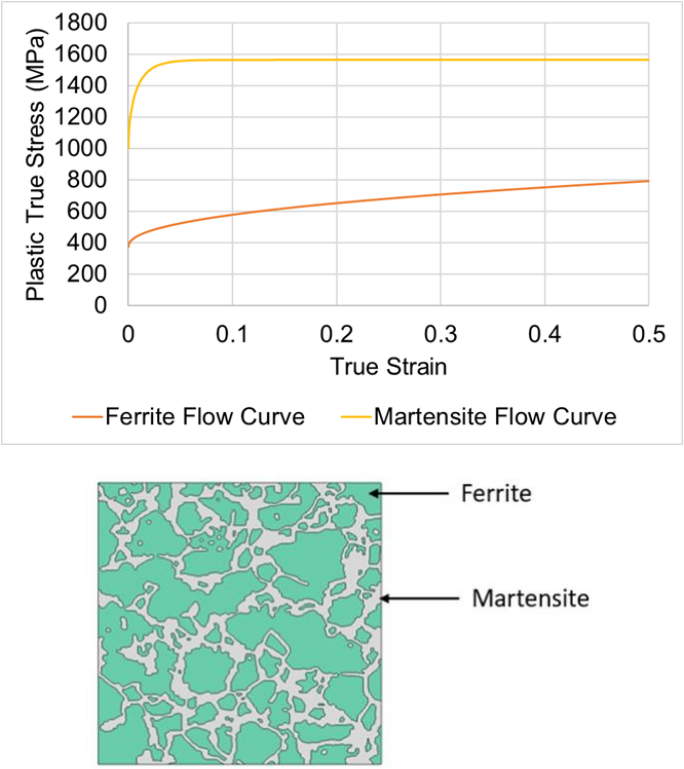

Fig. 61 – Flow curves of ferrite and martensite phase used for the RVE micromechanical model with the material strength properties applied to different segments of the RVE

As mentioned previously the application of material properties had to be done manually as there was no identified means to automate this. This presents a first limitation of using real microstructures for RVE modelling. Limitations of this approach is further discussed on the following results section.

6.3.3 Results from real Dual Phase Steel microstructure

This section discusses the results from the RVE modelling of DP micrographs. It became apparent early on that there were limitations to the real microstructures which fundamentally limited the use and applicability of this method. These findings are discussed below.

Fig. 62 – 2D RVE of real DP microstructure showing severe localised failure**Fig. 62** shows an image of the final deformation stages of the 2D RVE for the real micrograph. The image shows how stress concentrates in the martensite phase, with comparatively little stress happening in the ferrite matrix. However, the failure of the RVE has happened in a way that would not be expected for DP steels. It can be see that failure has occurred in one localised area of the martensite. Rather than failure bands forming throughout the RVE some areas of the martensite experience higher stress whilst other do not.

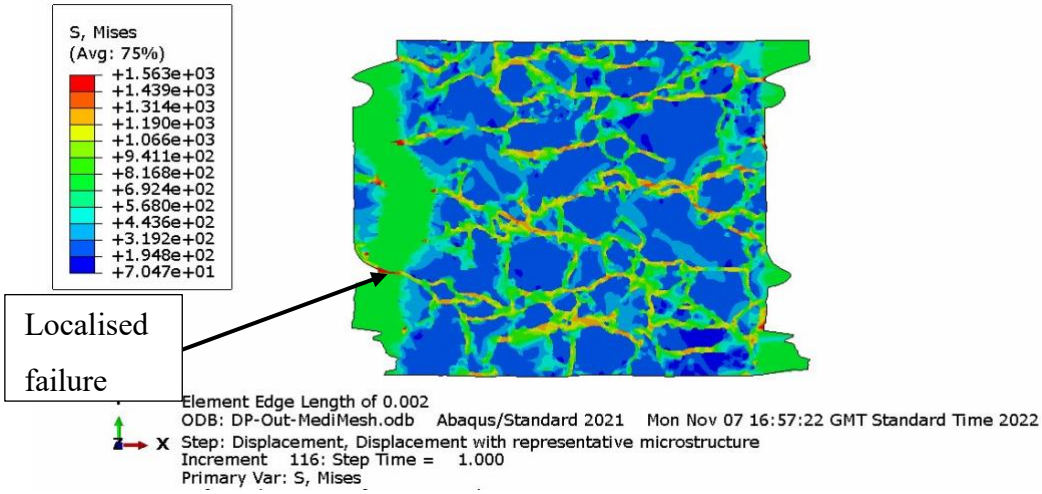

Fig. 62 – 2D RVE of real DP microstructure showing severe localised failure

It appears that what has occurred is that due to the distribution and morphology of the reinforcing martensite this failed sooner. With areas of the martensite, such as in the localised failure area, being narrow with a high aspect ratio and following the loading direction of the RVE stresses were able to concentrate in specific regions. As the loading-displacement increased the stress in that localised increased too, causing this local failure. It was also concluded that the way in which the material properties were applied played a role in the outcome of the simulation results. Whilst it commonly described that DP steels consists of a ferrite matrix with stronger martensite distributed throughout in the modelling approach the martensite is connected throughout with the ferrite being modelled as discrete island in the RVE. It can in inferred that this has had impact on the results of the RVE with one area of martensite failure having a greater impact than what would otherwise be expected. Additionally, the ferrite is prevented

from being able to transfer loading to different regions where martensite is not under load. Causing failure of the RVE as shown in **Fig. 62**.

An evaluation of the mesh density was also performed to review if alternative meshing approaches would generate improve results. Thes are shown in **Fig. 63** below where the Micro-Mesh is the highest mesh density of 1µm average node distance, the Medi-Mesh is a medium mesh density of 5µm average node distance, and the Macro-Mesh is the coarsest mesh density of 10µm average node distance. It can be seen that during the elastic deformation stage as well as the initial plastic deformation that there is no significant deviation in the stress strain flow curves for the three RVEs. There is then a divergence of results when the RVE fails, with the high mesh density showing a drop in the strength of the DP RVE before the medium and coarse mesh RVEs. This is likely due to the higher mesh density allowing for a greater fidelity in the stress distribution resulting in the earlier drop off in the stress flow curve. The next step is to develop a RVE that mitigates the effects of using micrograph images for the development of RVEs, this will be done by using synthetic randomly generated RVEs instead.

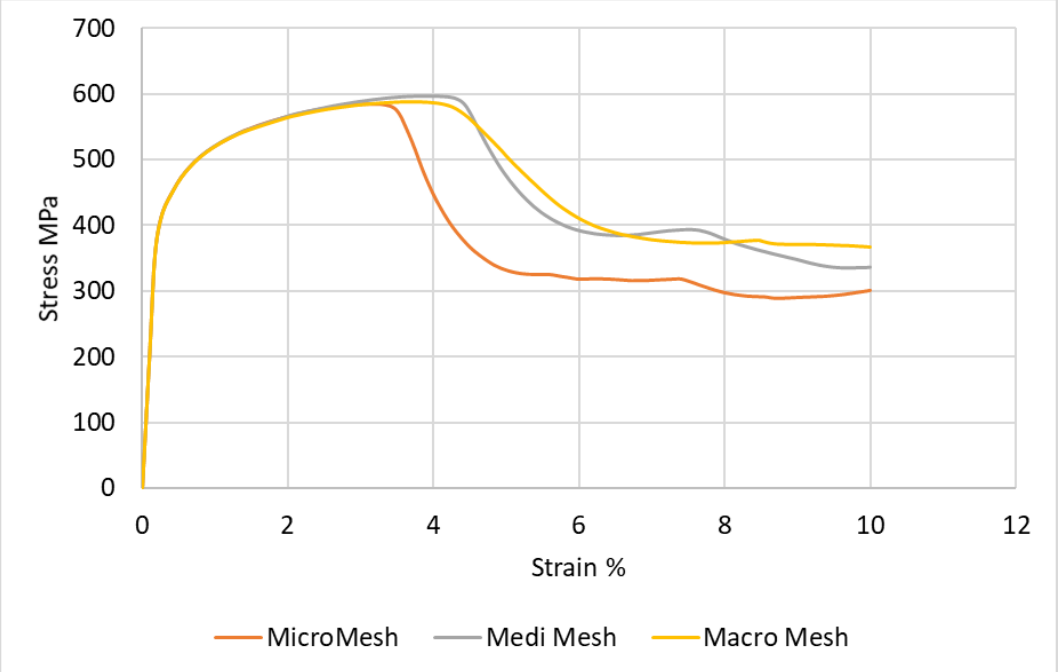

Fig. 63 – Stress-Strain distribution with different meshes of 2D RVE of real microstructure

It was however possible to analyse the elastic deformation and review if the material parameter used as well as the boundary and loading conditions generated results that

would be expected of the RVE. For the DP analysed the known Young's Modulus is 207GPa, this is the combined strength of the ferrite matrix and martensite reinforcement for real martensite. Therefore, the RVE model should produce a similar Young's Modulus value to the DP800 sample that was tested under uniaxial tensile testing.

For the RVE model this was found to be value of 206.5GPa. This shows good correlation for the modelling approach, that the material parameters of the ferrite and martensite are correct and that the applied boundary conditions are correct as well. This suggests that core concepts applied for the RVE are correct and this can be used as a foundation for other RVE models going forward. As mentioned, the limit of damage and stress concentrations in narrow bands of martensite means analysing the typical values of plastic strain is not feasible using a real microstructure. Therefore, the limit of elastic deformation and there point just after the onset of plastic deformation are considered the limit for this modelling approach.

6.3.4 Random RVE

For the 2D model of a DP alloy ad randomly generated microstructure was used as shown in **Fig. 64**. This was done using a script generated in python and implemented in Abaqus CAE. For this a simplified DP microstructure model was used, with a Ferrite matrix and discrete Martensite grains distrusted throughout. Whilst other additions such as carbide particles and alloying elements are expected to be present in DP, for this modelling work it was decided to have a simple two-phase model. With carbide particles known to strengthen DP steels.

The first RVEs generated were sone using a randomly generated microstructure. This was to quickly generate easy to RVEs for analysis. The main benefit is being able to rapidly generate many microstructures for analysis that have variations applied, such as volume fraction or grain size. This is more efficient than having to use micrographs of actual microstructures that needs to be imaged and transferred to a file type that can be interpreted in Abaqus software. As mentioned in the prior section it was concluded that there were limitations to using real micrographs, including others from literature which resulted in the decision to use virtual or synthetically generated DP steel RVEs.

Oval shaped martensite grains were used for this modelling approach. This was to replicate some of deformation that would occur in the martensite during the cold rolling process. Additionally, Nam et al. [158] found that alignment of martensite particles determined their fracture mode. With transverse grains bending and fracturing with increasing deformation in the longitudinal loading direction. Whereas martensite particles that are aligned with the loading direction would not fracture and martensite fracking not being an observed feature in the DP deformation. For this reason, orientation of martensite particles set to be the same as the loading direction. This can be seen in **Fig. 64** with discrete martensite particles randomly distributed in the RVE aligned along the x-axis. It was decided that discrete martensite distribution would generate more accurate results after using a RVE generated from a micrograph.

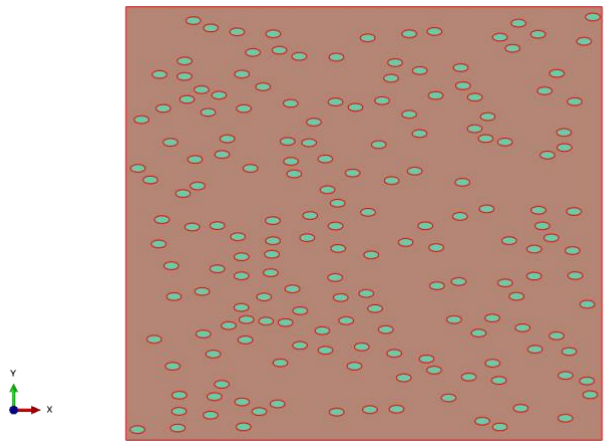

Fig. 64 – Randomly Generated 2D microstructure, discrete martensite phase distributed throughout.

6.4 Scripting and Development of 2D Representative Volume Element

Generating a RVE manually would be a time intensive process that would not be feasible when wanting to investigate a variety of parameters such those relating to the size & distribution of M-grains, and M-vf%.

To automate and reduce the time needed to generate the RVEs a python script was developed that can easily be implemented within the Abaqus software. This is described in the following sections.

6.4.1 Boundary Conditions and mesh

With sample modelled assumed to be imbedded within a larger matrix of material, it is necessary to apply the appropriate boundary conditions that recreate the equivalent deformation as if it were embedded in this larger material. For this periodic boundary conditions are applied to all the edge nodes of the 2D RVE, where a dent/bump on one edge results in a corresponding dent/bump on the other. However, Abaqus FE software does not have an automated function where RVE boundary conditions can be applied. The generation of boundary conditions and obtaining results needs to be prescribed in the model tree [159].

This can be shown in the Free Body Diagram **Fig. 65**, which describes how the 2D RVE deforms under load. For this work, Corner Node (A) is pinned to prevent any displacement in the X and Y direction. Corner node (B) is prevented from deforming in the Y-direction but is allowed to deform along the X-direction, it is from there where a displacement will be applied during the Load Step. Corner node (C) does not have any displacement boundary applied to it. And corner node D has a displacement condition applied in the X-direction but is allowed to move along the Y-direction. As this is a 2D RVE, no depth was assumed for the simulation and therefore no boundary conditions are used in the Z-Axis.

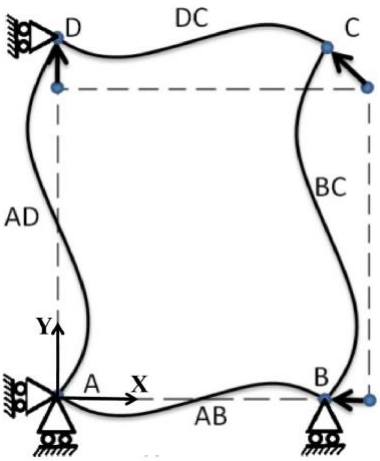

Fig. 65 – Free Body Diagram for the Representative Volume Element with boundary conditions applied

The boundary conditions for the micromechanical model were applied the following way. Two equivalent points (a) and (b) along each edge of the RVE are coupled

creating a deformation gradient between for two nodes, creating a node-edge-pair along the face of the RVE. Shown in the following equation:

$$\boldsymbol{u_i^b - u_i^a = \bar{F}_{ij}\left(x_{jo}^b - x_{j0}^a\right) - \left(x_{i0}^b - x_{i0}^a\right)} \quad \textbf{(15)}$$

Where x_{i0}^a, x_{i0}^b are the position of point pairs at initial non-deformed configuration. This is applied to all nodes along the Left-Right Face and the Top-Bottom Face of the RVE. The model is considered to have no thickness. The same process is applied for nodal displacement in the Y-direction, shown in the following equation:

$$\boldsymbol{u_i^b - u_i^a = \bar{F}_{ij}\left(y_{jo}^b - y_{j0}^a\right) - \left(y_{i0}^b - y_{i0}^a\right)} \quad \textbf{(18)}$$

And a generalised formula shown in:

$$\vec{x_T} = \vec{x_B} + \vec{x_4} + \vec{x_1} \quad \textbf{(19)}$$

$$\vec{x_R} = \vec{x_L} + \vec{x_2} + \vec{x_1} \quad \textbf{(20)}$$

$$\vec{x_3} = \vec{x_2} + \vec{x_4} + \vec{x_1} \quad \textbf{(21)}$$

This process is automated in a Python script where a non-corner node is selected along one face of the RVE, it then selects a node along the opposite edge. For nodes along the Left-Face, the script knows the Y-coordinate and uses the width of the 2D RVE to find and pair a corresponding node along the Right-Face, the same process is done with Bottom-Face known and using the height of the RVE to pair a node on the Top-Face. This is found by using a tolerated proximity of where a node is expected to be, this has to be refined to enough to not select multiple nodes for one node pair but to exclude nodes either. The script runs through until all node on the Left- and Bottom-Face are paired with a node along the Right- and Top-Face respectively. The corner nodes weren't paired to allow free movement during deformation process, discussed earlier in this section, the final RVE with paired nodes is shown in **Fig. 66**.

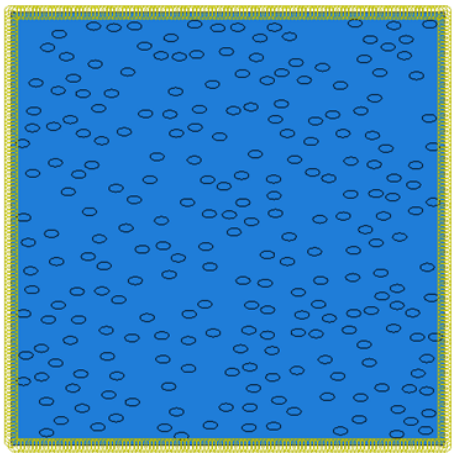

Fig. 66 – 2D RVE with all nodes paired along the edges and corners.

Displacement boundary conditions were applied to the Top-Left Corner node, the Bottom-Left Corner node and the Bottom-Right Corner node. With the Top-Left corner to move along the Y-axis, the Bottom-Left corner node is pinned allowing it to rotate but fixed in the X-axis and Y-axis, and the Bottom-Right corner node having a displacement applied to it in the X-axis.

The mesh was generated automatically in the Python script, this was based as a function of the mean grain size radius using the shorter the r_1 value for the equation of an ellipse. To generate an ellipsoid in Abaqus two lengths and a centre coordinate are needed. A shorter r_1 length, a longer r_2 length and a x,y centre. For this the average grain height, the r_1 length, was 0.0018µm. Therefore, the mean distance between nodes was set at 0.0018µm with a free self-generating mesh generated using 2D solid plane stress 4-node bilinear elements with hourglass control. Hourglass control is applied to maintain simulation accuracy by preventing deformation where no strain energy is applied to a particular element.

6.5 Results

6.5.1 Initial Results for the Boundary Conditions

Initial visual analysis was done on the 2D RVE to review the Periodic Boundary Conditions (PBC) applied on the edges of the model. A simplified model with few elements and martensite grains was used to perform a basic examination and to run a rapid simulation., this can be seen in **Fig. 67** below:

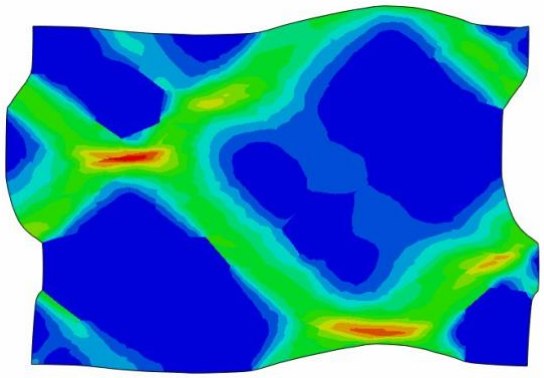

Fig. 67 – Simple 2D RVE with PBC applied, showing strain

It can be seen at deformation on the edges mirror each other. Where a dent or bump on one side corresponds with an equivalent dent or bump on the other. This shows that the periodic boundary conditions applied are effective and can be used for subsequent simulation analysis. Another characteristic of the PBC is limitations on how stresses can form within the RVE. As the sample is assumed to be embedded within a larger volume of material the stresses on the edge should match if a copy of the same RVE is placed next to it, with a Left-to-Right and Top-to-Bottom being able to match. If an individual RVE is considered as one tile. Then by placing multiple RVEs will form a repeating mosaic pattern. This can be seen in the following image with multiple 2D RVEs put together. Each RVE can be considered an individual tile forming a repeating pattern in a larger material shown **Fig. 68.**

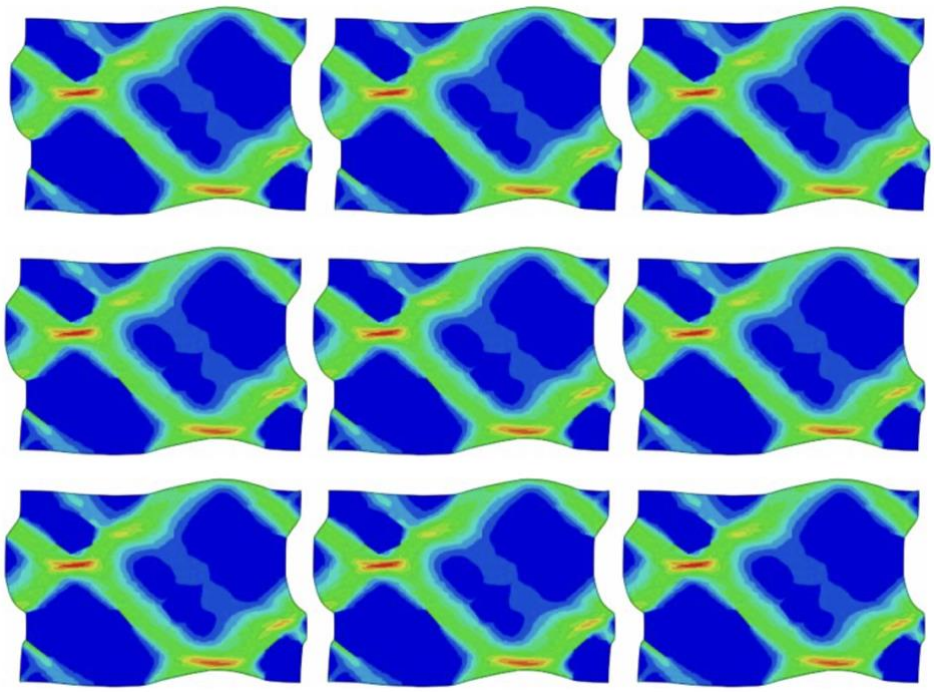

Fig. 68 – Combined deformed RVEs showing a repeating mosaic pattern.

When placing the 2D RVE into a 3x3 pattern, a repeating pattern emerges. Where stress paths on one edge matches that of the other 2D RVE on the other. From the initial analysis, what can also be seen is a preferred strain path develops in the RVE. Where the relatively weaker ferrite will undergo a greater amount of strain compared to the stronger martensite. Whereas the martensite will deform less but will undergo greater stress compared to the ferrite, this can be seen in the following **Fig. 69** and **Fig. 70** which shows the von Mises Stress and Plastic Equivalent Strain respectively. This shows in effect a composite modelling approach, similar methods have been deployed for plastic composites but not for metallic alloys.

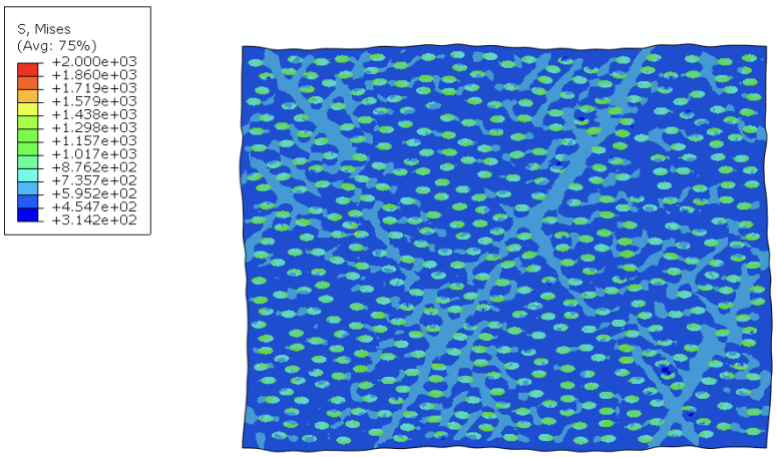

Fig. 69 – Stress Distribution in 2D RVE of DP Steel, stresses concentrate in the martensite particles with ferrite that has undergone large local deformation also showing higher relative strain

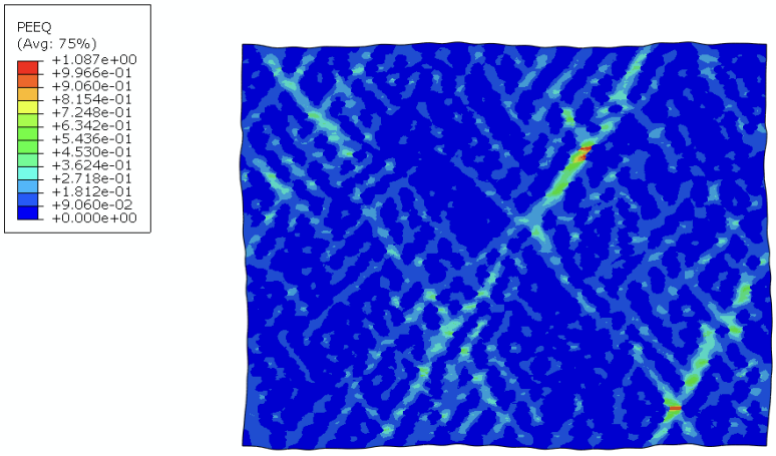

Fig. 70 – 2D RVE with 30% Martensite content showing von Mises Stress and Plastic Equivalent Stress at the same time step

This shows that the martensite acts as a reinforcing element for the DP alloy, with the Ferrite predominantly undergoing deformation. With the material undergoing a preferred deformation path via the ferrite. It can be considered therefore that a relationship exists in the between martensite content and strength of the DP alloy. This would conform to literature and be examined by varying the relative martensite content, this is discussed in the following section. Another area of interest that can reviewed with the model is the failure and how this happens during deformation. As discussed in the literature section, failure is likely to occur near the boundary between two grains with different strength properties or at the site of inclusions, such as carbides. With this simplified model only the grain boundaries can be assessed with

how this impacts the failure mechanisms. This too is discussed in the subsequent section.

6.5.2 Martensite Vm Surface Fraction Concentration

2D RVEs with varying martensite content starting at 5% V_m and increasing in increments of 5% up to 30% and a final maximum martensite content 33% V_m. 33% V_m was the maximum obtainable content in the modelled developed and a 35% martensite V_m was attempted this was not achievable with the current modelling approach, despite typical DP steels with high martensite contents of around 35% [115] and going to 40% [132,160]. However, due the spacing constraints between individual martensite grains the script used to develop the model would not exceed a 33% surface fraction without having overlapping grains or the spacing between nodes becoming too small. This therefore presents a limitation with this modelling approach in the maximum possible content for martensite achievable for the 2D RVE model. Five RVEs were developed for each martensite content. As the martensite grains were distributed randomly in each RVE, clusters may form around localized zones in the RVE when dispersed martensite reinforcement is desired. Each simulation was run and result aggregated to produce average stress strain curves for the 2D RVEs of varying martensite content. Expected results from increasing the reinforcing martensite content is that the material should be stringer with a higher yield point and ultimate strength. Additionally, as the ratio of stronger but more brittle increases relative to the weaker but more elastic ferrite the RVEs should show a higher relative strength but have a reduction in overall ductility. The combined average for the stress-strain curves are shown in **Fig. 71** below:

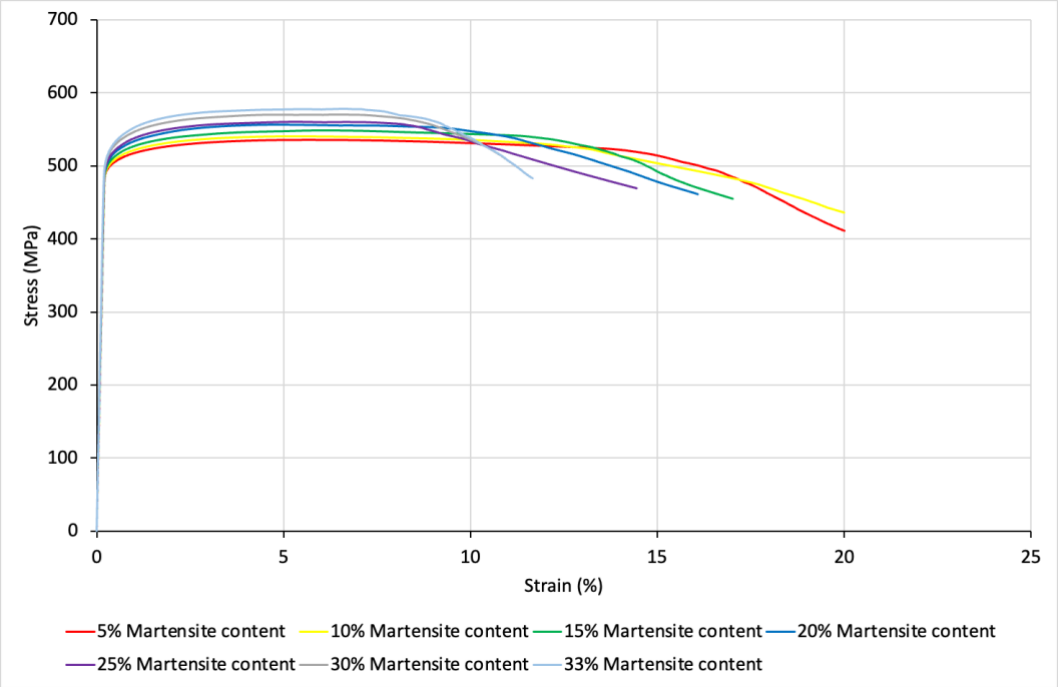

Fig. 71 – 2D RVEs Stress Strain curves with varying martensite Vm

This shows that the linear-elastic deformation of all RVEs is the same, this is because the initial deformation occurs exclusively in the ferrite matrix. As the strength properties for ferrite is the same across all RVEs, the initial deformation strains are the same. The differences in outputs from the RVEs occurs at onset of plastic deformation and up to the point where the RVEs begin fail, this can be seen in **Fig. 72** below. This is a zoomed in section that shows the yield point of the RVEs with varying martensite content and the plastic deformation of the of the RVE until a drop off in the von Mises stress values happens which is representative of material failure.

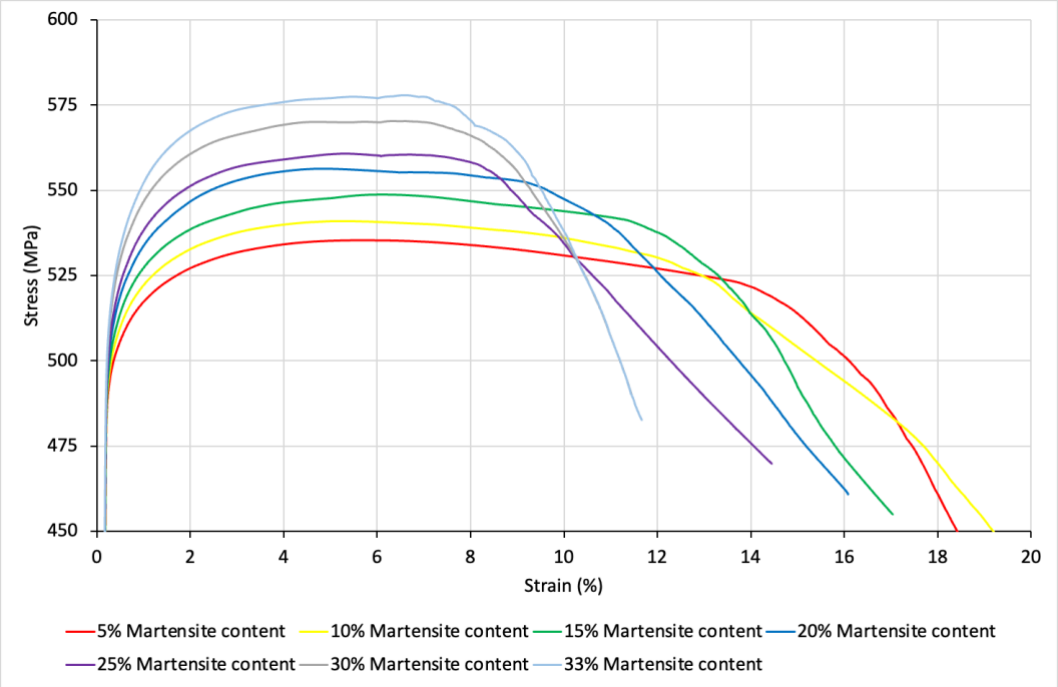

Fig. 72 – 2D RVEs Stress Strain curves with varying martensite V_m

The plots in **Fig. 72** show that with varying martensite content two trends can be observed. Firstly, as martensite content increases the peak strength, UTS, of the DP RVE increases too. This is due to the greater amount martensite acting as a reinforcing mechanism in the RVE. With von Mises Stress in 5% martensite V_m peaking at 535MPa at 6% strain and the RVE effectively failing at 14% strain. For the RVE with highest martensite content of 33% V_m the peak von Mises Stress is 580MPa and occurs at 4.9% strain. This is then followed by a more immediate drop in the material strength at 8% strain, indicating a that there is less work hardening after the peak UTS von Mises stress is reached and is therefore a more brittle material.

Secondly, as martensite content increases the fracture strain decreases which corresponds to the drop in the von Mises stress. Going from 14% strain down to 8%, additionally the UTS strain value decreases from 6% down to 4.8%. It can be concluded that the addition of martensite has made the DP RVE more brittle. This correlates with the work done other researchers [109,132] who have shown the affects of higher martensite contents increases the strength of DP alloy but also reduces the alloy's ductility with failure occurring at a lower strain values. It can be concluded that the martensite content plays a significant role in how DP steels fail. With little

martensite having a low impact on the final failure mode, whereas with higher concentrations martensite becomes the dominant factor in DP failure due to the stress incompatibilities.

This was further analysed by reviewing the strains for all DP models at which peak stress occurred and plotted to review a potential relationship. This is shown in **Fig. 73** below. Each dot represents the average for given martensite concentration's RVEs peak stress and the corresponding strain at which this occurs. The dots were also ordered in descending martensite concentration, going from the highest 33% martensite V_m to the lowest 5% martensite V_m. The figure shows that with increasing martensite content from 5% to 33% the maximum stress (UTS) increases from 535MPa to 578MPa. However, a corresponding decrease in the strain at which that peak stress is reached decreases. Effectively making the DP alloy more brittle. This follows within the similar trends that have been observed by other researchers [110,134,161].

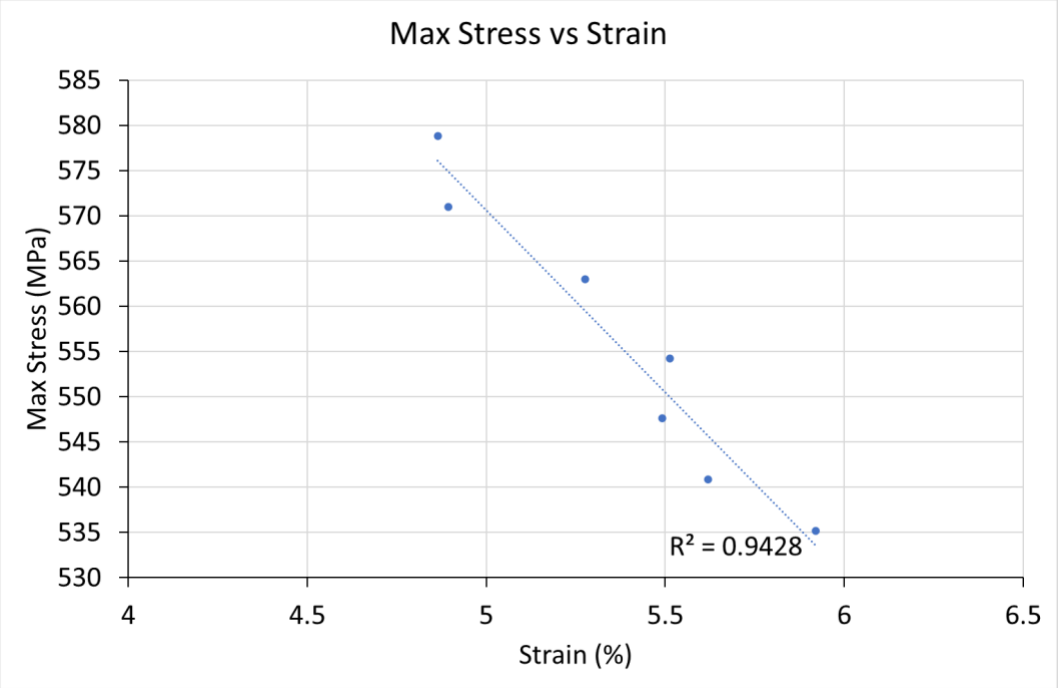

Fig. 73 – Maximum Stress vs Strain, Varying martensite content plotted against stresses and strain. Each dot represents the peak von Mises stress of a RVE with martensite Vm, with left to right having a higher to lower martensite concentration.

6.5.3 Failure mode for DP in 2D RVE

It is also worth examining what is happening to the RVE at the point of failure, this is best viewed by looking at the plastic equivalent strain. This can been seen in **Fig. 74** below, this shows a 20% martensite V_m at the point if failure. It can be observed that strain develops at a 45% angle relative to the loading direction and occurs predominantly in the ferrite matrix. That strain is predominantly in the softer ferrite matrix rather than the harder martensite grains should be expected.

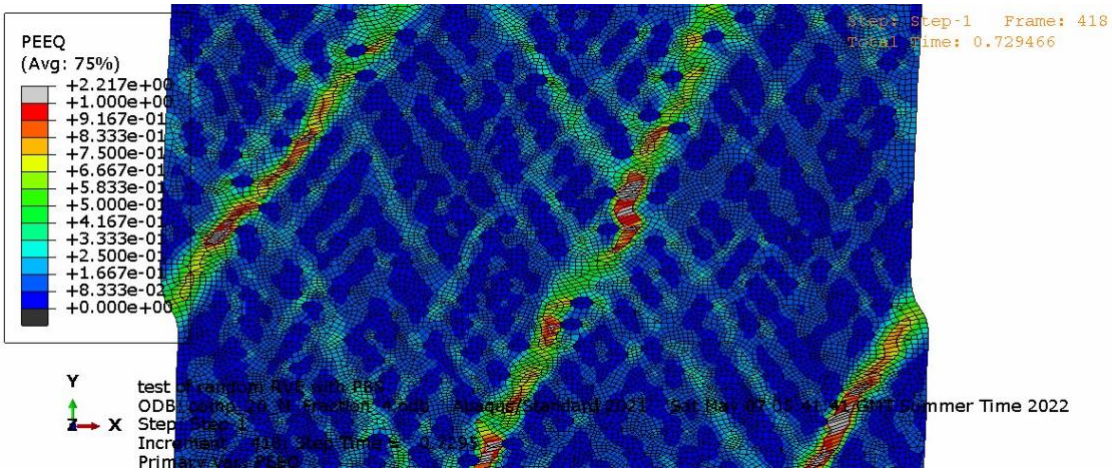

Fig. 74 – Failure along the shear strain bands in the RVE micromechanical model

Understanding the failure mechanisms of DP alloy is an area of great interest, as this allows for optimized development of future alloy grades. The benefit of the microscale modelling approach is the opportunity to perform multiple virtual tests on different grades and view this failure in real time, versus post-mortem or interrupted experimental testing.

In the 2D RVE model, strain occurs at two levels. There is the global strain, which refers to the entire model and does not account for the different phases. Then there is the local strain; this refers to the strain can happen either within a particular region of

the RVE or one of the two phases. Due do the different strengths of the Ferrite and Martensite, strain will occur predominantly within the relatively softer Ferrite. This disparity in the amounts of strain that occurs between the two phases impacts how occurs failure in the 2D RVE and what impact different Martensite concentrations will have in how strain develop. For that reason, in this section when stress and strain is discussed it refers to that which occurs at the local level in either Ferrite matrix or Martensite particles. Deformation is used when discussing the global strain in the 2D RVE.

One of the main ways DP alloys are known to fail is due to the stress incompatibilities between the two phases with failure occurring at the interface between a martensite-ferrite grain boundary [116,162]. From analysis performed in the RVE model setup, failure in the DP alloy occurs in the following way;

During the initial stages of deformation, stresses build up in Martensite phase with relatively little occurring in the ferrite matrix. As RVE deformation continues, the relatively softer ferrite matrix undergoes greater amounts of strain with the martensite having no significant deformation itself. That strain initiates at the interface between a martensite particle and the ferrite matrix. This is due to the different material strength causing an incompatibilty in the strains being able to develop uniformly. The strain continues to develop through ferrite phase at a 45° degree relative to the loading direction. However, once those strain bands flow into a martensite particle its development is interrupted. As strain can no longer develop in that region the martensite particle acts a reinforcement with stresses building up in the martensite. This process continues with new nucleation points developing where strains initiate at the interface between the ferrite matrix and martensite particles. This process in shown in **Fig. 75** and **Fig. 76** showing the development of Equivalent Plastic Strain (PEEQ) and von Mises Stress respectively up to failure of the 2D RVE. Typically, in DP alloys failure occurs due to the nucleation and coalescence of voids in the material leading to rupture in the material. Due to different Young's Modulus' in the two materials, voids form at the interface between the two phases, this can be seen in **Fig. 75** and **Fig. 76** below.

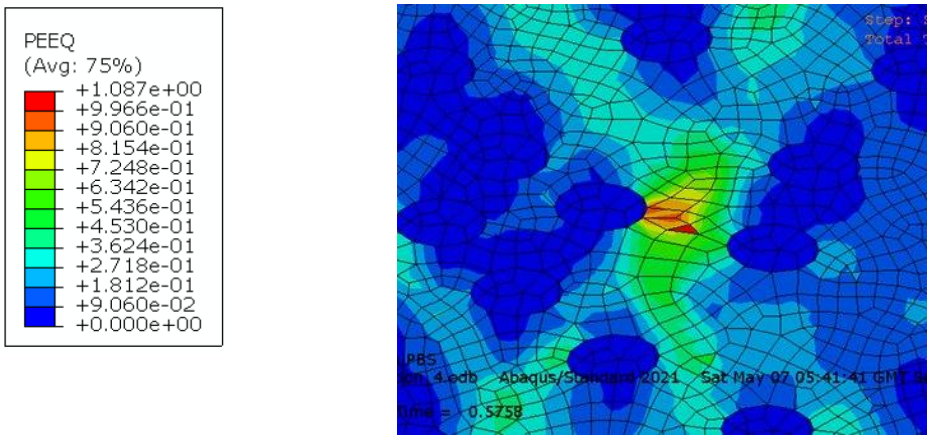

Fig. 75 – Failure of DP alloy due stress incompatibility at M-F grain boundary shows initiation of strain

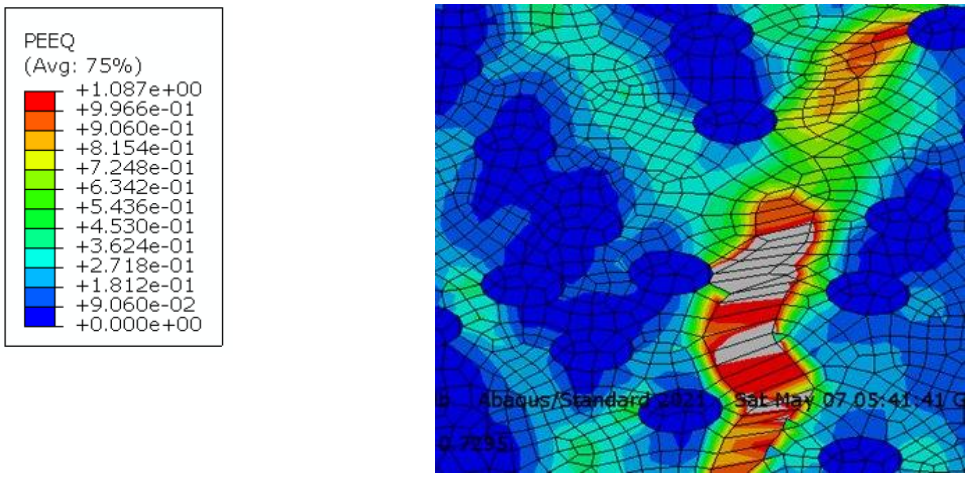

Fig. 76 – Failure of DP alloy due stress incompatibility at M-F grain boundary shows ferrite elements that are no longer reinforcing the RVE shown in grey. Elements are not deleted but do not contribute to the strength of the RVE.

Due to the ever-increasing strain in the ferrite phase, eventually a critical point is reached where the material starts to fail and no longer contributes to the strength of model. At this stage large strain bands form with relatively little further deformation having to occur to the RVE. This is considered the point where voids have coalesced, and the DP alloy has failed.

6.5.4 Stress-Strain Distributions for varying martensite concentrations

Fig. 77, **Fig. 78** and **Fig. 79** show the evolution of von Mises Stress and Equivalent Plastic Strain with increasing martensite concentrations, that being 5% V_m, 20% V_m

and 30% V_m respectively. Images were taken at the same time step for each RVE for both the von Mises Stress and the Plastic Equivalent Strain. It can be seen that stresses develop predominantly in the martensite phase with plastic strain occurring mostly in the ferrite matrix. Whilst the way stresses and strain initiate and continue to develop as the RVE undergoes deformation with stresses building up in the martensite and plastic strain occurring predominantly in the ferrite matrix.

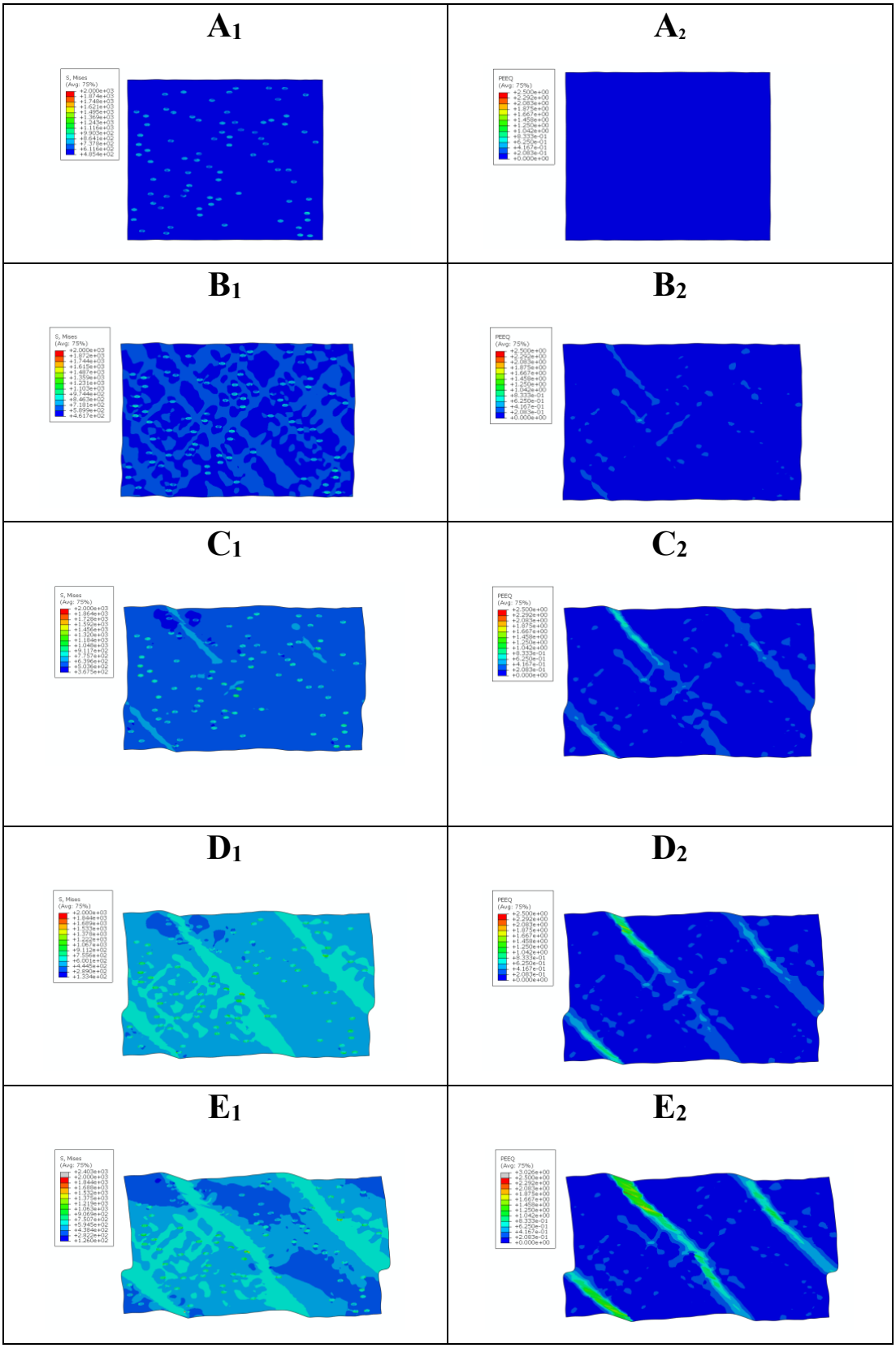

Fig. 77 – von Mises Stress A_1 to E1 and PEEQ A_2 to E_2 for 5% martensite content

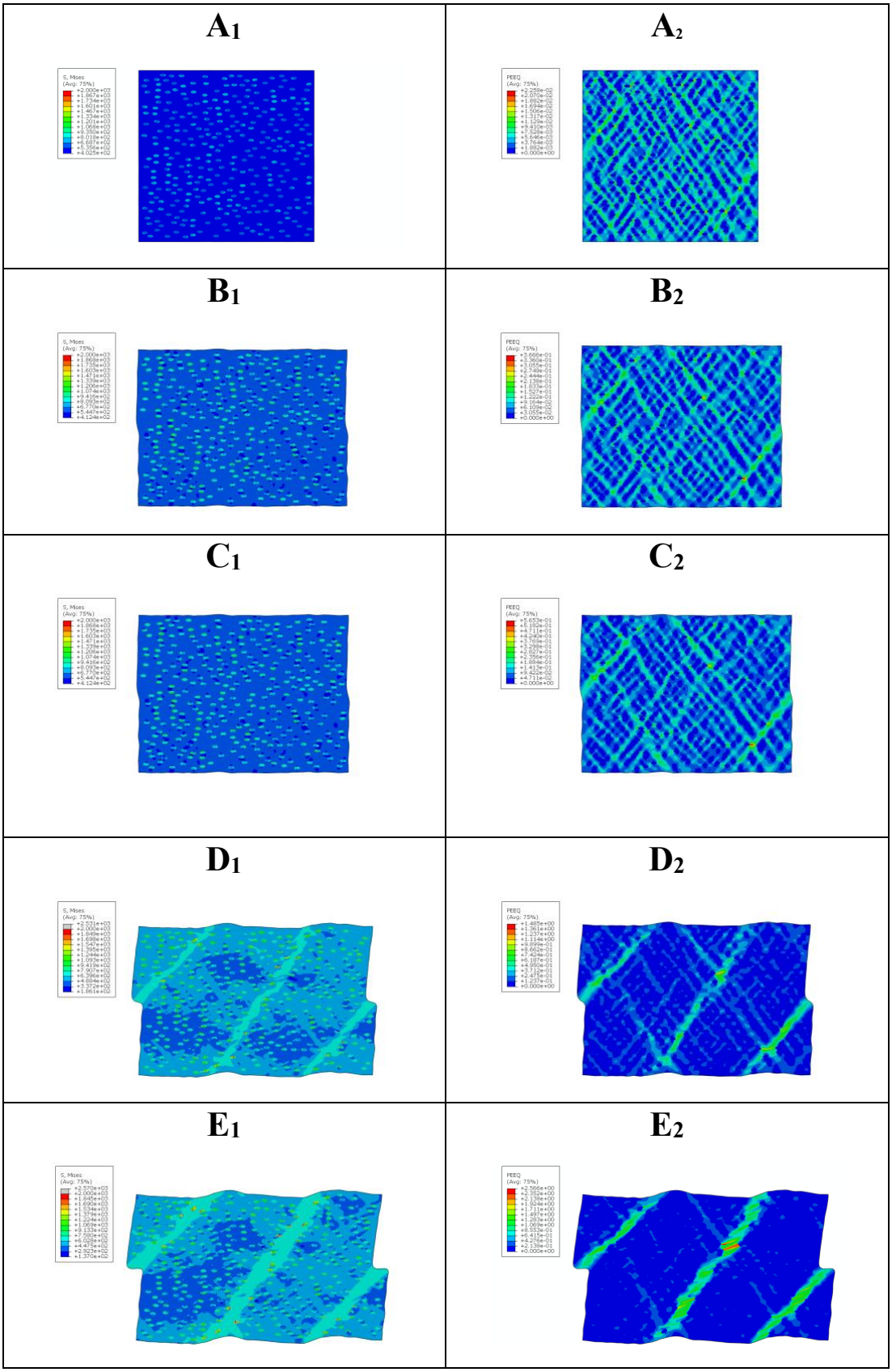

Fig. 78 – von Mises Stress A_1 to E1 and PEEQ A_2 to E_2 with 20% martensite content

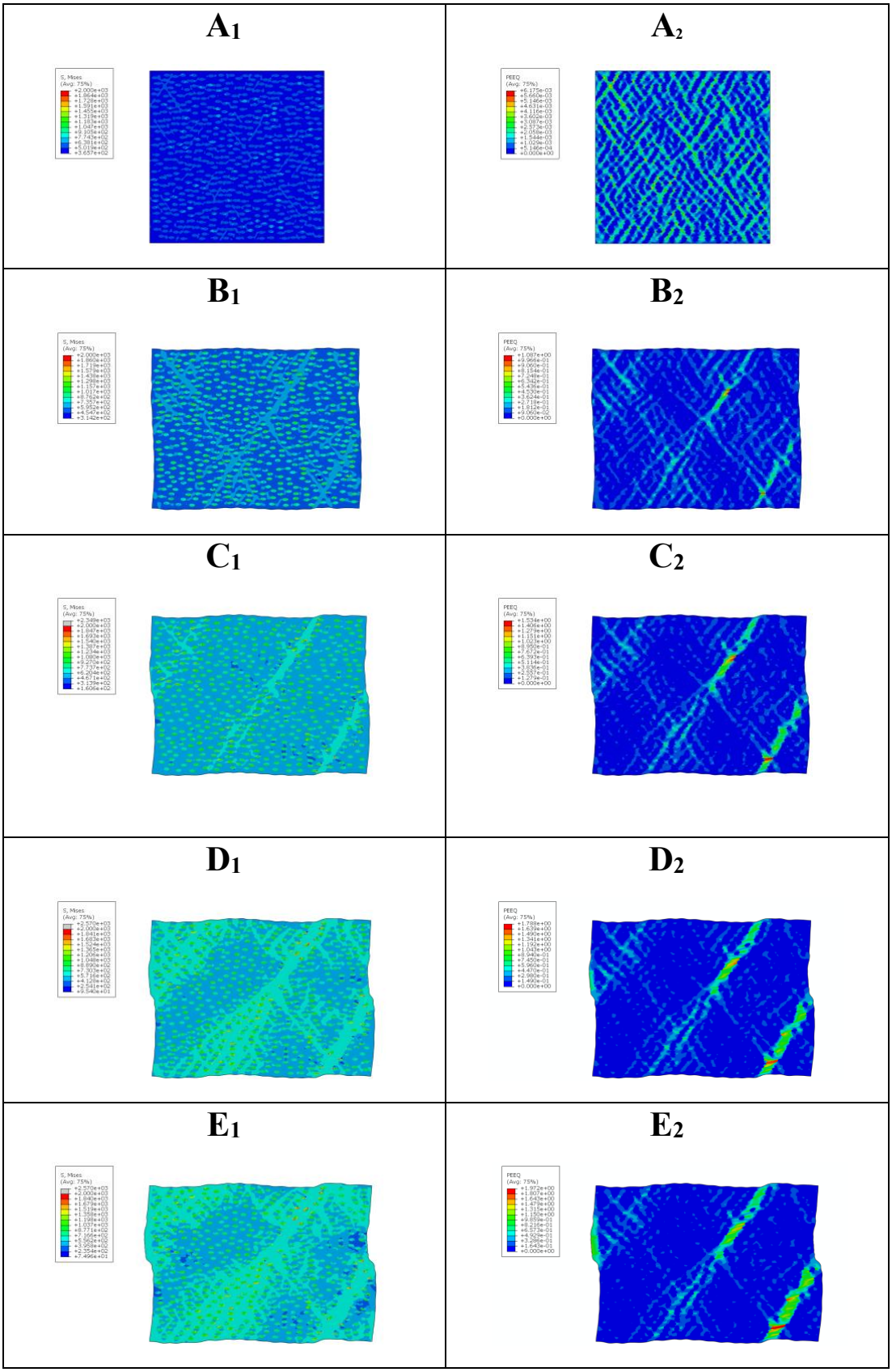

Fig. 79 – von Mises Stress A_1 to E1 and PEEQ A_2 to E_2 with 30% martensite content

6.6 2D Synthetic RVE Conclusions

6.6.1 Randomly Generated Microstructure

For the randomly generated/theoretical microstructures, a composite modelling approach was used to generate 2D RVEs. In this process the dimensions of the RVE were specified which consisted of the ferrite matrix. The RVE was then partitioned with distinct martensite islands populating the matrix until prescribed M-V% was achieved. As the martensite grains were randomly distributed, the process was repeated until 5 RVEs of each volume fraction was created. This process is novel compared to other authors where RVEs were already partitioned into domains that represent the average of the periodic grains and the grains then randomly partitioned into martensite and ferrite [116,163,164]. This method also used martensite grain with an aspect ratio of 2 to account for cold rolling effects of DP steel during manufacturing processes this is different to [99].

The effects of martensite content on DP alloy was investigated by means of using a 2D RVE using randomly distributed discrete grains of martensite throughout. Ovalized grains were used to recreate the effects of cold rolling during the manufacturing process. A simple two-phase model was use, inclusions in the model were not investigated. Results from the modelling showed that increasing martensite content resulted in increased UTS of the DP RVE with a corresponding reduction in the materials ductility.

Strain in the Ferrite phase develops at 45° degrees relative to the loading direction, this can be seen in **Fig. 80** below. Plastic strain flow has a preference to continue developing within the ferrite. Once it reaches a harder martensite particle that strain can no longer continue developing, with stresses building up in the martensite particle instead. Strains will then continue to develop and build in the other regions of the ferrite phase, with this process repeating throughout the 2D RVE. This eventually reaches a point where the Ferrite can no longer continue undergoing plastic strain, at this stage stresses start to build up in the martensite particles. This increase in stress

does not remain solely within the martensite but also develops in the surrounding ferrite phase. Eventually, due to the stress incompatibilities of the two phases, voids form as the interface between the ferrite matrix and martensite particles.

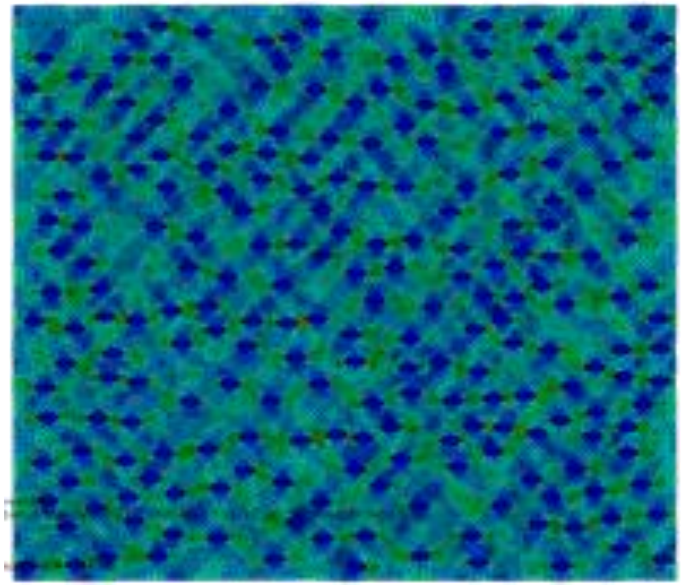

Fig. 80 – 2D RVE showing the development of strain bands 45° relative to the loading direction. Martensite particles interrupt the growth of these strain bands, reinforcing the RVE.

For martensite to act as an effective reinforcement on the 2D RVE, a minimum V% is required. In this thesis, that minimum volume fraction was found to be 10M-V%. Below this value strains develop exclusively in the ferrite phase and some stress develops in the martensite phase. This M-V% value is less than in [165] which found that DP with a M-V% less that 15% global ductility is dependent on the ductility of the ferrite matrix.

Without enough martensite particles in the RVE, the growth of strain bands is not effectively interrupted, with the martensite undergoing displacement within the ferrite matrix. A failure of the RVE occurs without the martensite having effectively acted as a reinforcement. Similar results were found by Shen et. Al [107] who found that in DP steels with a low martensite content only the ferrite would deform with no measurable deformation occurring in the martensite particles.

As martensite V% increases, this results in a higher number of martensite particles in the 2D RVE that can interrupt the growth of strain. This reinforces and strengthens the

DP alloy allowing to withstand higher loading for a given deformation when compared to a DP alloy that has a lower martensite V%. However, due Martensite being more brittle when compared to the Ferrite phase, the total amount of deformation that the 2D RVE can undergo is reduced. It was found from the modelling DP alloy has become less ductile with it failing at a lower global strain.

Considerations need to be made for the distribution of martensite particles. These should be evenly distributed to act as an effective reinforcing agent in the RVE model. Clustering of martensite particles prevents effective reinforcement of the DP alloy, with strain continuing to develop in the Ferrite matrix and failing with Martensite having not been able to act as an effective reinforcement.

A next step would be to include the effect of tertiary elements in the 2D RVE model, inclusions such as carbide particles or ceramic inclusions could be added. This would potentially provide a more holistic nucleation points for voids to develop. This would make it harder to analyse the effects of the individual elements as the complexity of the model would increase. This could be achieved by the further literature review into the property of tertiary inclusions such as strength characteristics volume content and size distribution.

6.6.2 Real Microstructure

Real microstructures could be modelled with the RVE modelling approached used here. The quality of the simulated results was dependent on the distribution of martensite phase in the RVE generated, based on the micrograph image. Combined material properties predicted in the elastic phase is within an allowable error tolerance. However, much beyond the elasto-plastic transition the strength of the RVE drops dramatically. This is due to stress concentration occurring in narrow bands of the martensite phase. Once the martensite fails and is no longer able to provide reinforcement there is a sudden drop of in the material strength.

Controlling the quality of the image used as the foundation of the RVE is key, this has to be both representative of the microstructure as whole, but also be such that it can be implemented in a modelling approach. One of the limits is the manual nature of using real microstructures compared to randomly generated ones. As the image has to be

modified such that it can first be converted into a file that allows for import into Abaqus Simulation Software. The application of material properties needs to be reviewed, ensuring that the correct material properties are applied. Then the node distance must be checked to ensure that a uniform meshing approach can be applied to the RVE. This manual approach is time consuming therefore limiting the number simulations that can be completed in a given time. It also limits the number variations that can be built into the model. Whereas the virtual microstructure approach can, once a baseline has been established as valid can be easily varied to measure impacts of features such martensite grain size and distribution for easily than using a real microstructure.

Results from real microstructures also showed that the morphology and orientation of martensite grain has a significant impact of the strength of the RVE. For elongated martensite particles that are aligned with the loading direction in the RVE, their relative strength and overall contribution to the RVE was higher than martensite grains being loaded transverse to the loading direction in results by Nam [158] who found that thin fibrous martensite particles which were aligned transverse to the loading drawing axis are bent and fracture with increasing longitudinal strain.

6.7 3D Modelling

6.7.1 Introduction

The work up to now has only explored RVE modelling in 2D dimensions even though we live in a Three Dimensional world. This step was meant to explore RVE modelling in 3D. However, due limitations in time approach it was not possible to create valid data that could be analysed. What follows is a brief description of the work done and as a proof of concept.

6.7.2 Developing 3D RVE

Neper/FEPX software [166] was used to develop 3D RVEs for import into Abaqus. This software was used to automatically produce 3D RVEs with specified grain sizes and martensite concentrations. A half cut of a 3D RVE is shown in **Fig. 81.** This shows

in red the ferrite matrix with green martensite crystals distributed throughout. The model part was automatically generated in the Neper software and can now be meshed.

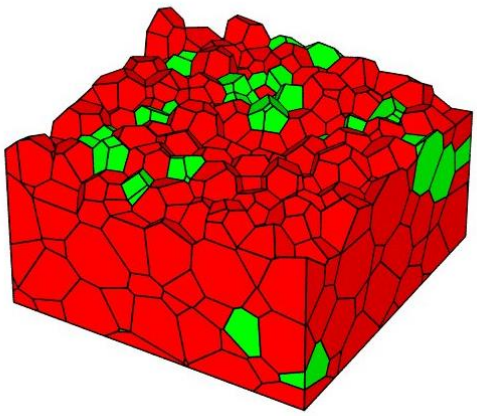

Fig. 81 – Cut at 50% along the z-axis showing the grains in the 3D RVE, green being martensite and red ferrite all generated in NEPER

The RVe was meshed natively in Neper, mesh was automatically generated with an in-house algorithm [166] and is shown in **Fig. 82**. This uses triangular elements with each colour representing a unique grain in the RVE.

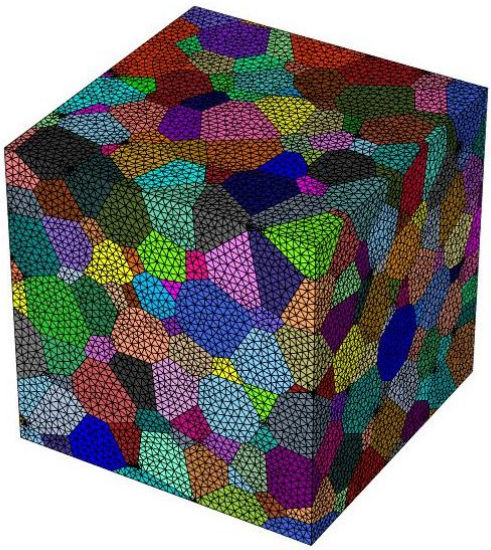

Fig. 82 – 3D RVE tessellation having been meshed in NEPER

Fig. 83 shows the 3D final part of with meshing applied to all components in a file type that could be imported into Abaqus. However, once the parts where imported it was not possible to apply boundary conditions onto the surfaces of the 3D RVE, either via use of with the script developed in Python3.1 or as plugin tool in Abaqus. It was concluded that the element nodes could not be paired to generate the required boundary conditions. It was concluded that an alternative square mesh technique was needed.

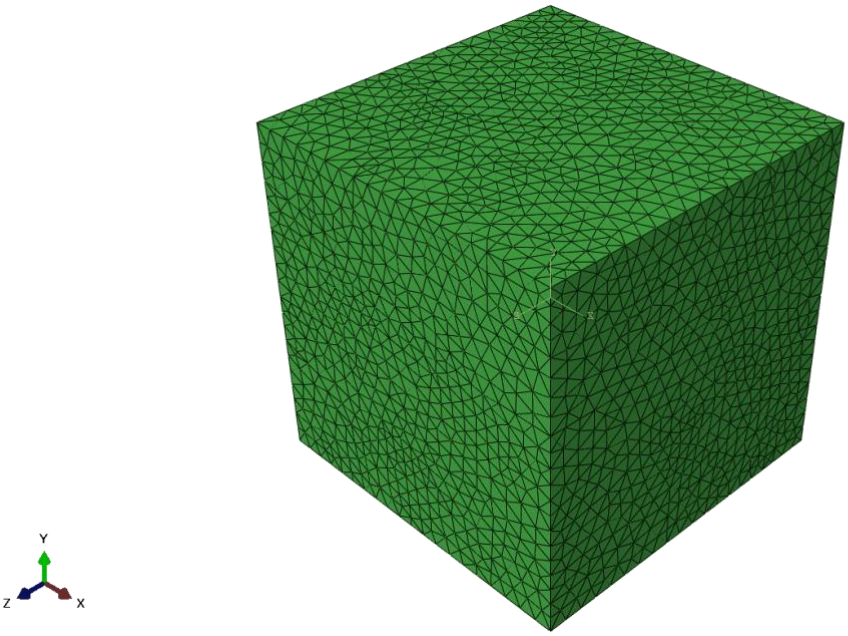

Fig. 83 – Meshed 3D RVE part imported into ABAQUS

6.7.3 3D RVE using different mesh approach

An alternative mesh approach was used where the cordinates on the 6 faces of the RVE would be equal and opposite. This is to allow pairing of nodes for the periodic boundary conditions. Shown in **Fig. 84** and **Fig. 85**. Whilst this limits the accuarcy of the results they still present an interesting study that can be developed in future work.

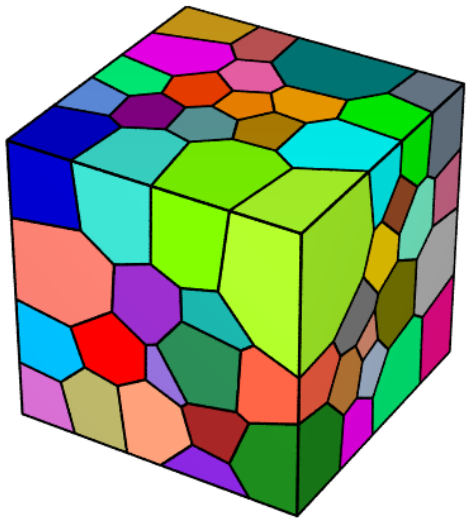

Fig. 84 – 3D Tessellation generated in NEPER

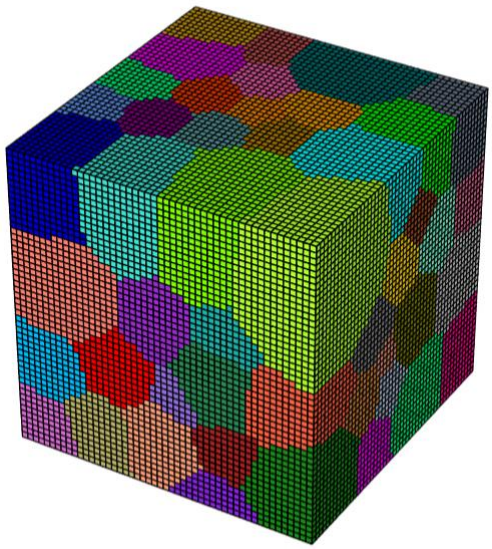

Fig. 85 – Meshed tessellation that can be imported into Abaqus

6.7.4 Visual Results for Stress distribution

Unfortunately it was not possible to extract reliable results from the RVE model. Instead only indicative results could be drawn from the modelling. **Fig. 86** shoes the von Mises stress distribution in the martensite phase with **Fig. 87** showing the distribution of stress in the ferrite phase. It can be seen that like in the 2D RVE stresses concentrate in the martensite phase. With comparatively little happening in the ferrite phase.

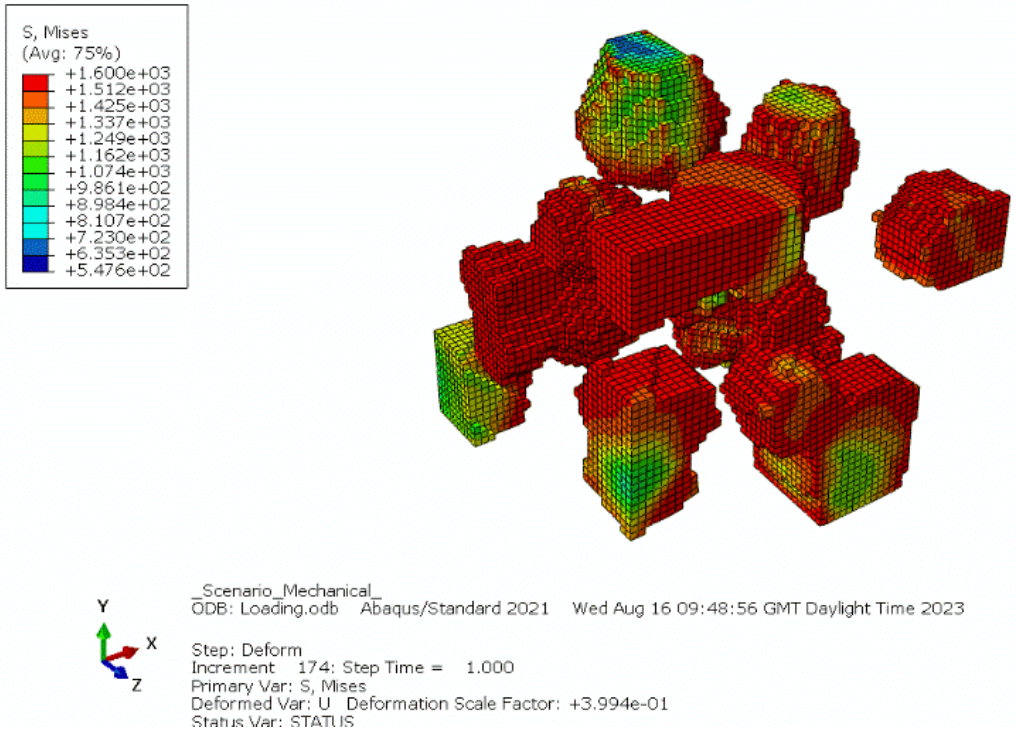

Fig. 86 – Stress in Martensite in the 3D RVE

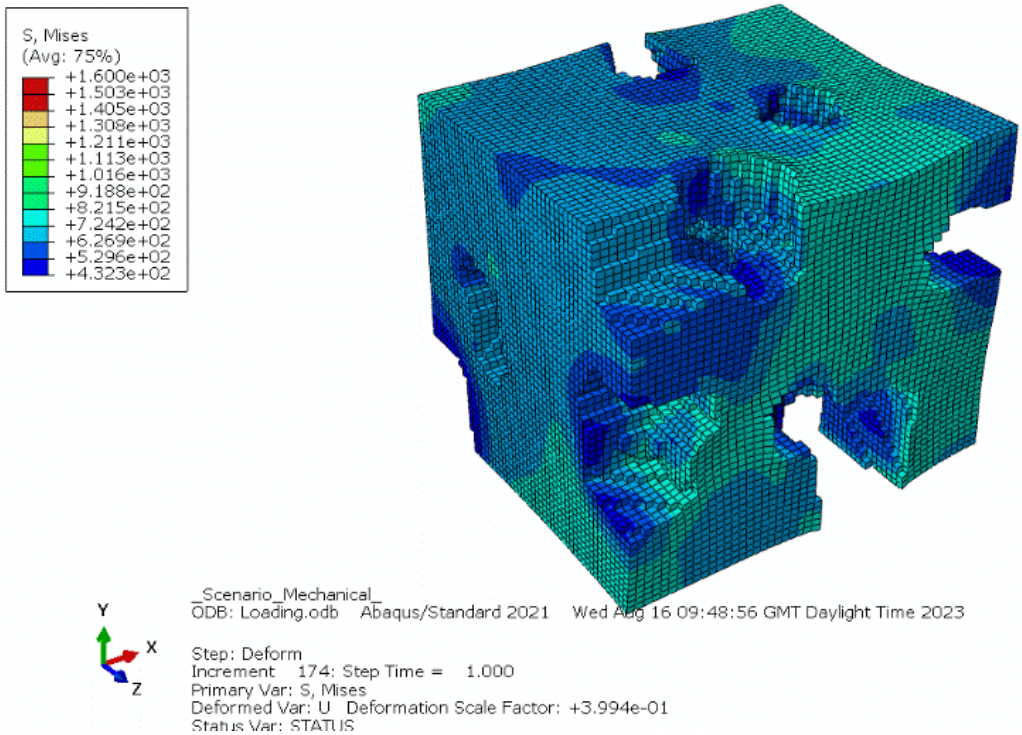

Fig. 87 – Stress in Ferrite in the 3D RVE

It can be seen that similar to the 2D, stresses develop predominantly in the harder martensite phase. With comparatively little occurring in the ferrite matrix. Ferrite that is in close proximity to the martensite phase show a higher level stress compared to areas further away from the martensite. This would suggest that the ferrite in this region is more likely to fail due to stress incompatibilities.

6.7.5 Visual Results Plastic Strain

Fig. 88 and **Fig. 89** shows the plastic equivalent strain in martensite and ferrite phases respectively. Like the 2D RVEs the martensite undergoes little strain with it mostly occurring in the interface regions with ferrite. Suggesting that there are stress incompatibilities between the phases. Whilst in Fig. 92 shows that there are more strains in the ferrite due to its relatively softer material properties compared to martensite.

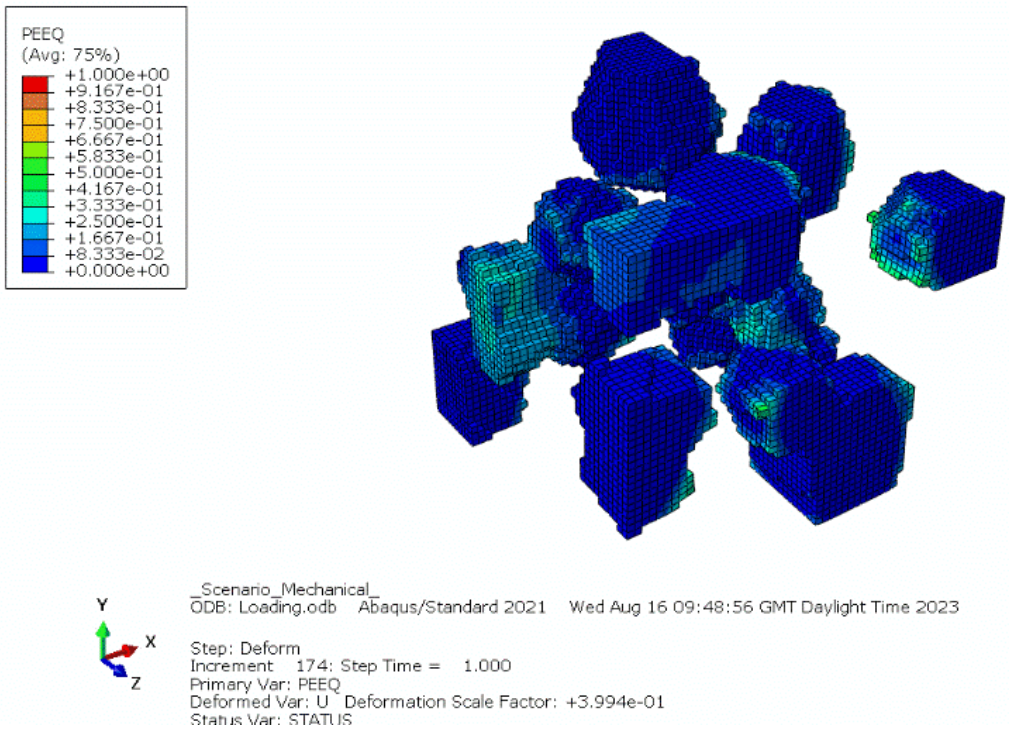

Fig. 88 – Plastic Equivalent Strain in the 3D RVE

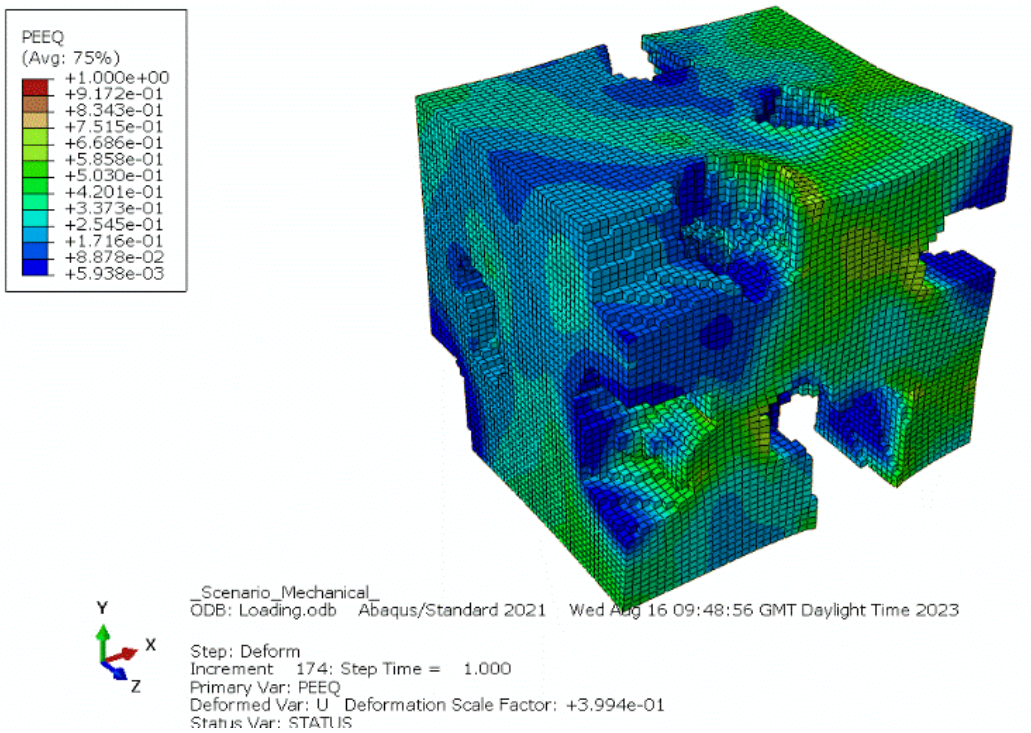

Fig. 89 – Plastic Equivalent Stress Ferrite the 3D RVE

Similar to the 2D modelling approach, strain occurs mostly in the relatively softer ferrite matrix, with relatively happening in the ferrite matrix. In martensite grains, areas that close to the ferrite matrix have higher levels of plastic strain compared to the centre. As martensite is comparatively more brittle, when martensite grain crack this would initiated from the edges and move inwards for complete breaking.

Whilst some results could be obtained from the 3D RVE, the current process does need refinement. Focus on the application of periodic boundary conditions should be done so that the more refined mesh in **Fig. 83** can be used in future analysis. As it can been that the stepped meshed in between the boundary phases does have an impact on the distributions of stresses and strain close interface between a martensite particle and the ferrite matrix.

6.7.6 3D RVE Results

Modelling using Neper tessellation approach: The completed modelling of 3D RVE demonstrates that the principles employed on the 2D random RVE can be replicated.

That being a continuous load-deformation curve with a two-composition model with materials of different strength and ductility, those being the harder martensite and the softer ferrite matrix. The model shows that the harder martensite undergoes little deformation with a build-up of stress, whilst the ferrite does not have the same stress build-up but with an increase in plastic strain as the RVE is deformed and the global load response is recorded. What can also be concluded with 3D model are the initiations of the failure mechanisms that is observed from the 2D random RVE with higher stresses in the ferrite developing near the interface with a martensite grain. The limitations that became evident was the compromises in the mesh approach to correctly apply the right periodic boundary conditions on the faces of the 3D RVE. For the boundary conditions to be successfully applied matching node pairs on the opposite faces were needed, which could only be done with a square mesh. Creating a stepped interface between grains rather than straight line. Any future would have to resolve this before future potential benefits of the 3D model can be effectively used. That being able to add damage initiation and evolution, and the through thickness effects of martensite grains.

Ultimately this 3D RVE whilst a proof concept and broadly follows what type of deformation was happening in the 2D RVE as a tool it requires more development if it to be used for RAP of DP steel alloys.

6.8 Summary

Three types of RVE were modelled, first using a real microstructure that validated the applied boundary conditions. This however had its limitations as it could not be used to validate into plastic deformation with how the ferrite matrix and reinforcing martensite particles were modelled. This then followed the generation of synthetic two-phase DP RVEs generated by a script in python software. This showed how DP fails due to stress incompatibilities and can be used hypothesise material properties of future DP alloys. Lastly 3D RVEs were attempted, whilst these showed that the indicative results are valid this type of modelling approach is more complex and time intensive to develop functioning models.

7 Conclusions

This thesis evaluated the use small scale testing techniques for the use developing novel alloy grades, namely DP800 for the RAP process with ShP tests. DP800 undergoing shear punch tests was investigated to review the use of such testing procedure for new alloy developments. Modelling at the continuum and microlevel was done in Abaqus to how stresses develop in DP whilst undergoing deformation in such a narrow band of material and what effects martensite has on the alloy. Evaluating what the microstructural constituents like the martensite content on the bulk material of the sample was evaluated. This was done via a 2D RVE synthetically generated microstructure which was successful in describing the material deformation at the microstructure level and can be used to predict optimised DP steel microstructures.

The list main objectives of this thesis were:

1. Evaluation of DP800 alloy undergoing miniaturised testing techniques, for this thesis the Shear Punch test was chosen to perform tests on the alloy and evaluate the evolution of stresses during punch loading and serve as a baseline for development of the models later.

2. Perform a parameter study on the Shear Punch Test to review the tolerance requirements for repeatability in results.

3. Develop a 3D model to simulate damage in the Shear Punch

4. Simulate microstructure deformation of Dual Phase steel to study how an anisotropic distribution of two phases affects the bulk material properties via a Representative Volume Elements.

From this the following can be drawn:

The parameter study showed the tight tolerances needed when setting a shear punch test. Whilst some effects like sample thickness can be mitigated, if known as this is

part of the input values for the shear stress. Other factors such as the punch corner tip radius did have an impact on the simulation outputs as these would effectively increase the radial shear zone in the test piece. Having the effect of reducing the punch radius.

A 3D model was developed which incorporated damage mechanisms using a Johnson-Cook damage model. Whilst the model was able to make good prediction on the Yield and Ultimate strength of dual phase steels in shear punch tests, the elongation values did not agree. This shows further refinement is needed in the input for the model development. Particularly as these material properties have produced good results as inputs for small punch simulations and mini tensile simulations.

2D RVEs were developed to evaluate the how an inhomogeneous material microstructure loads and affects the bulk material for duals phase steels. In the 2D RVE the buildup of stress and strain is not evenly distributed throughout the material. Stresses build up in the martensite phase, with higher concentrations of martensite adding strength to the RVE but reducing it ductility. Strain initiates at the interface between ferrite and martensite. Strain develops through the ferrite matrix at a 45° angle relative to loading directions. The growth of strain bands is interrupted by the presence of martensite.

In dual phase steels failure at the microscale occurs in the regions close to where ferrite and martensite are. This failure occurs due to a build-up of strain in the ferrite phase throughout the RVE. Eventually, due to incompatibilty on the stresses and strain between the two phases, failure occurs by ferrite no longer being to contribute to the RVE.

3D RVEs were developed using Neper software. These were more problematic in being able to apply periodic boundary conditions on an appropriately refined mesh. As the node coordinates need to be known on the equal-opposite it was only possible to apply the boundary conditions if the faces have square grid. Some results for visual analysis were used but reliable values for stresses and strains in the individual phases were not. This was particularly prevalent at the interface between grains where the stepped mesh was having an impact on the distributions of stresses and strains.

8 Future Work

As a continuation of tis research, further work should be done on the microstructure analysis of DP800 alloy that undergo ShP testing procedure. There is still a knowledge in how stress initiate and evolve during the testing procedure and where failure occurs. This is currently not known and can only be inferred from the modelling approach undertaken as outlined in this thesis. This is particularly relevant where more complex microstructures are present or imperfect distributions happen during the manufacturing process such as banding in DP800 alloy.

Further developments are still needed in the 3D continuum modelling of the ShP test. The generation of appropriate material parameters are key for generating appropriate stress-strain flow curves that match experimental testing. This is largely via an improved ductile damage and Johnson-Cook model needed to better evaluate the ductility and elongation in the model. Whilst the model produces good values for the Yield Strength and Ultimate Strength, elongation values was not easily replicated. This even if material parameters have been used successfully to evaluate and successfully model miniaturized tensile tests and small punch tests where good replicability was produced. This refinement in the material parameters can then be used to continue the modelling approach and understand how stresses develop during ShP testing of other metallic materials to examine the robustness of the model.

Refinement of the virtual RVE script to include greater variation of martensite particle sizes in the simulation to measure the impacts that this variance on the model output as well as using varying grain geometries can be applied, a clustering algorithm for the martensite grains to evaluate the effects that an uneven distribution of martensite grain would have, and the inclusion of secondary elements to move to a more complex model rather than the two-phase microstructure that has been used. This would all feed into the development of a refined 3D model with the correct boundary conditions applied.

References

1. Environmental aspects of the automotive industry | Internal Market, Industry, Entrepreneurship and SMEs [Internet]. [cited 2021 Jul 30]. Available from: https://ec.europa.eu/growth/sectors/automotive/environment-protection_en

2. Raabe D, Ponge D, Dmitrieva O, Sander B. Nanoprecipitate-hardened 1.5GPa steels with unexpected high ductility. Scr Mater [Internet]. 2009;60(12):1141–4. Available from: https://www.sciencedirect.com/science/article/pii/S1359646209001626

3. Frommeyer G, Brüx U. Microstructures and mechanical properties of high-strength Fe-Mn-Al-C light-weight TRIPLEX steels. Steel Res Int. 2006;77(9–10):627–33.

4. Springer H, Raabe D. Rapid alloy prototyping: Compositional and thermo-mechanical high throughput bulk combinatorial design of structural materials based on the example of 30Mn–1.2C–xAl triplex steels. Acta Mater [Internet]. 2012;60(12):4950–9. Available from: https://www.sciencedirect.com/science/article/pii/S1359645412003278

5. Kada SR, de Vaucorbeil A, Fabijanic D, Barnett MR. Work hardening and the scratch resistance of Ni–Co alloys using a rapid prototyping approach. Wear [Internet]. 2022;510–511:204493. Available from: https://www.sciencedirect.com/science/article/pii/S0043164822002502

6. Rao Z, Springer H, Ponge D, Li Z. Combinatorial development of multicomponent Invar alloys via rapid alloy prototyping. Materialia (Oxf) [Internet]. 2022;21:101326. Available from: https://www.sciencedirect.com/science/article/pii/S2589152922000138

7. Blindheim J, Welo T, Steinert M. Rapid prototyping and physical modelling in the development of a new additive manufacturing process for aluminium alloys. Procedia Manuf [Internet]. 2019;34:489–96. Available from: https://www.sciencedirect.com/science/article/pii/S2351978919309424

8. Wang H, Jiang W, Ouyang J, Kovacevic R. Rapid prototyping of 4043 Al-alloy parts by VP-GTAW. J Mater Process Technol. 2004 May 1;148(1):93–102.

9. Farrugia D, Brown S, Lavery NP, Pleydell-Pearce C, Davis C. Rapid Alloy Prototyping for a range of strip related advanced steel grades. Procedia Manuf [Internet]. 2020;50:784–90. Available from: https://www.sciencedirect.com/science/article/pii/S2351978920318400

10. Zhu Y, Slater C, Connolly S, Farrugia D, Davis C. Rapid alloy prototyping for strip steel development: DP800 steel case study. Ironmaking & Steelmaking [Internet]. 2021;48(5):493–504. Available from: https://doi.org/10.1080/03019233.2021.1880036

11. Zhang L, Harrison W, Yar MA, Mehraban S, Brown SGR, Lavery NP. Use of miniaturized tensile specimens to evaluate the ductility and formability of dual phased steels for Rapid Alloy Prototyping. Materials Science and Engineering: A [Internet]. 2023;875:145075. Available from: https://www.sciencedirect.com/science/article/pii/S0921509323004999

12. Manahan MP, Argon AS, Harling OK. The development of a miniaturized disk bend test for the determination of postirradiation mechanical properties. Journal of Nuclear Materials. 1981 Jan 1;104(C):1545–50.

13. Bruchhausen M, Turba K, De Haan F, Hähner P, Austin T, De Carlan Y. Characterization of a 14Cr ODS steel by means of small punch and uniaxial testing with regard to creep and fatigue at elevated temperatures. Journal of Nuclear Materials. 2014 Jan 1;444(1–3):283–91.

14. Gülçimen B, Durmuş A, Ülkü S, Hurst RC, Turba K, Hähner P. Mechanical characterisation of a P91 weldment by means of small punch fracture testing. International Journal of Pressure Vessels and Piping. 2013 May 1;105–106:28–35.

15. Bruchhausen M, Holmström S, Simonovski I, Austin T, Lapetite JM, Ripplinger S, et al. Recent developments in small punch testing: Tensile properties and DBTT. Theoretical and Applied Fracture Mechanics [Internet]. 2016;86:2–10. Available from: http://dx.doi.org/10.1016/j.tafmec.2016.09.012

16. Bruchhausen M, Austin T, Holmström S, Altstadt E, Dymacek P, Jeffs S, et al. European Standard on Small Punch Testing of Metallic Materials. In: Volume 1A: Codes and Standards [Internet]. American Society of Mechanical Engineers; 2017. Available from: https://asmedigitalcollection.asme.org/PVP/proceedings/PVP2017/57908/Waikoloa,

17. Holmström S, Simonovski I, Baraldi D, Bruchhausen M, Altstadt E, Delville R. Developments in the estimation of tensile strength by small punch testing. Theoretical and Applied Fracture Mechanics [Internet]. 2019;101:25–34. Available from: https://www.sciencedirect.com/science/article/pii/S0167844218304038

18. Rodríguez González MC, García Cabezas J, Cárdenas Paredes DE, Belzunce Varela FJ, Betegón Biempica MC. Mechanical properties characterization of heat-affected zone using the small punch test. 2009;

19. García TE, Rodríguez C, Belzunce FJ, Peñuelas I, Arroyo B. Development of a methodology to study the hydrogen embrittlement of steels by means of the small punch test. Materials Science and Engineering A [Internet]. 2015;626:342–51. Available from: http://dx.doi.org/10.1016/j.msea.2014.12.083

20. Simonovski I, Holmström S, Bruchhausen M. Small punch tensile testing of curved specimens: Finite element analysis and experiment. Int J Mech Sci. 2017 Jan 1;120:204–13.

21. Dymáček P. Recent developments in small punch testing: Applications at elevated temperatures. Theoretical and Applied Fracture Mechanics. 2016 Dec 1;86:25–33.

22. CEN Workshop Business Plan CEN Workshop Business Plan : ‘Small Punch Test Method for Metallic Materials’ 1 The CEN Workshop.

23. Hamada AS, Kisko A, Khosravifard A, Hassan MA, Karjalainen LP, Porter D. Ductility and formability of three high-Mn TWIP steels in quasi-static and high-speed tensile and Erichsen tests. Materials Science and Engineering: A [Internet]. 2018;712:255–65. Available from: https://www.sciencedirect.com/science/article/pii/S092150931731571X

24. Lancaster R, Davies G, Illsley H, Jeffs S, Baxter G. Structural integrity of an electron beam melted titanium alloy. Materials. 2016 Jun 14;9(6).

25. Janča A, Siegl J, Haušild P. Small punch test evaluation methods for material characterisation. Journal of Nuclear Materials. 2016;481:201–13.

26. Dymáček P. Recent developments in small punch testing: Applications at elevated temperatures. Theoretical and Applied Fracture Mechanics. 2016 Dec 1;86:25–33.

27. Altstadt E, Houska M, Simonovski I, Bruchhausen M, Holmström S, Lacalle R. On the estimation of ultimate tensile stress from small punch testing. Int J Mech Sci [Internet]. 2018;136:85–93. Available from: https://www.sciencedirect.com/science/article/pii/S0020740317331156

28. Rasche S, Kuna M. Improved small punch testing and parameter identification of ductile to brittle materials. International Journal of Pressure Vessels and Piping [Internet]. 2015;125:23–34. Available from: http://dx.doi.org/10.1016/j.ijpvp.2014.09.001

29. Simonovski I, Baraldi D, Holmström S, Altstadt E, Delville R, Bruchhausen M. Determining the ultimate tensile strength of fuel cladding tubes by small punch testing. Journal of Nuclear Materials. 2018;509:620–30.

30. Lancaster RJ, Jeffs SP, Haigh BJ, Barnard NC. Materials & Design Derivation of material properties using small punch and shear punch test methods. Mater Des [Internet]. 2022 [cited 2022 Mar 2];215:110473. Available from: https://doi.org/10.1016/j.matdes.2022.110473

31. Linse T, Kuna M, Schuhknecht J, Viehrig HW. Usage of the small-punch-test for the characterisation of reactor vessel steels in the brittle-ductile transition region. Eng Fract Mech. 2008;75(11):3520–33.

32. García TE, Rodríguez C, Belzunce FJ, Suárez C. Estimation of the mechanical properties of metallic materials by means of the small punch test. J Alloys Compd. 2014;582:708–17.

33. Simonovski I, Holmström S, Bruchhausen M. Small punch tensile testing of curved specimens: Finite element analysis and experiment. Int J Mech Sci. 2017 Jan 1;120:204–13.

34. Chica JC, Bravo Díez PM, Preciado Calzada M. Improved correlation for elastic modulus prediction of metallic materials in the Small Punch Test. Int J Mech Sci. 2017;134(September):112–22.

35. Mao X, Takahashi H. Development of a further-miniaturized specimen of 3 mm diameter for tem disk (ø 3 mm) small punch tests. Journal of Nuclear Materials. 1987 Sep 1;150(1):42–52.

36. Rodríguez González MC, García Cabezas J, Cárdenas Paredes DE, Belzunce Varela FJ, Betegón Biempica MC. Mechanical properties characterization of heat-affected zone using the small punch test. 2009;

37. Priel E, Mittelman B, Haroush S, Turgeman A, Shneck R, Gelbstein Y. Estimation of yield and ultimate stress using the small punch test method applied to non-standard specimens: A computational study validated by experiments. Int J Mech Sci. 2018 Jan 1;135:484–98.

38. Pandey AV, Karthik V, Shaik AR, Kolhatkar A, R. D. Estimation of UTS from small punch test using an improved method. International Journal of Pressure Vessels and Piping [Internet]. 2022;200:104818. Available from: https://www.sciencedirect.com/science/article/pii/S0308016122002034

39. Altstadt E, Ge HE, Kuksenko V, Serrano M, Houska M, Lasan M, et al. Critical evaluation of the small punch test as a screening procedure for mechanical properties. Journal of Nuclear Materials. 2016 Apr 15;472:186–95.

40. Guduru RK, Darling KA, Kishore R, Scattergood RO, Koch CC, Murty KL. Evaluation of mechanical properties using shear–punch testing. Materials Science and Engineering: A. 2005 Mar 25;395(1–2):307–14.

41. Esfandyarpour MJ, Alizadeh R, Mahmudi R. Applicability of shear punch testing to the evaluation of hot tensile deformation parameters and constitutive analyses. Journal of Materials Research and Technology. 2019 Jan 1;8(1):996–1002.

42. Sellamuthu P, Collins PK, Hodgson PD, Stanford N. Correlation of tensile test properties with those predicted by the shear punch test. Mater Des. 2013 May 1;47:258–66.

43. Guduru RK, Nagasekhar A V., Scattergood RO, Koch CC, Murty KL. Finite element analysis of a shear punch test. Metall Mater Trans A Phys Metall Mater Sci. 2006;37(5):1477–83.

44. Guduru RK, Nagasekhar AV, Scattergood RO, Koch CC, Murty KL. Thickness and Clearance Effects in Shear Punch Testing. Adv Eng Mater [Internet]. 2007;9(3):157–60. Available from: https://advanced.onlinelibrary.wiley.com/doi/abs/10.1002/adem.200600255

45. Karthik V, Visweswaran P, Vijayraghavan A, Kasiviswanathan K V, Raj B. Tensile–shear correlations obtained from shear punch test technique using a modified experimental approach. Journal of Nuclear Materials [Internet]. 2009;393(3):425–32. Available from: https://www.sciencedirect.com/science/article/pii/S0022311509006904

46. Esfandyarpour MJ, Alizadeh R, Mahmudi R. Applicability of shear punch testing to the evaluation of hot tensile deformation parameters and constitutive analyses. Journal of Materials Research and Technology. 2019 Jan 1;8(1):996–1002.

47. Sellamuthu P, Collins PK, Hodgson PD, Stanford N. Correlation of tensile test properties with those predicted by the shear punch test. Mater Des. 2013 May 1;47:258–66.

48. Guduru RK, Darling KA, Kishore R, Scattergood RO, Koch CC, Murty KL. Evaluation of mechanical properties using shear–punch testing. Materials Science and Engineering: A. 2005 Mar 25;395(1–2):307–14.

49. Goyal S, Karthik V, Kasiviswanathan K V., Valsan M, Rao KBS, Raj B. Finite element analysis of shear punch testing and experimental validation. Mater Des. 2010 May 1;31(5):2546–52.

50. Acharya S, Ray KK. Assessment of tensile properties of spot welds using shear punch test. Materials Science and Engineering: A. 2013 Mar 10;565:405–13.

51. Lancaster RJ, Jeffs SP, Haigh BJ, Barnard NC. Derivation of material properties using small punch and shear punch test methods. Mater Des [Internet]. 2022;215:110473. Available from: https://www.sciencedirect.com/science/article/pii/S0264127522000946

52. Karthik V, Laha K, Parameswaran P, Chandravathi KS, Kasiviswanathan K V., Jayakumar T, et al. Tensile properties of modified 9Cr-1Mo steel by shear punch testing and correlation with microstructures. International Journal of Pressure Vessels and Piping. 2011 Oct 1;88(10):375–83.

53. Guduru RK, Nagasekhar A V., Scattergood RO, Koch CC, Murty KL. Finite element analysis of a shear punch test. Metall Mater Trans A Phys Metall Mater Sci. 2006;37(5):1477–83.

54. Zergani A, Mirzadeh H, Mahmudi R. Finite element analysis of plastic deformation in shear punch test. Mater Lett. 2021 Feb 1;284:128953.

55. Dotcheva M, Millward H. The application of tolerance analysis to the theoretical and experimental evaluation of a CNC corner-milling operation. J Mater Process Technol. 2005 Dec 14;170(1–2):284–97.

56. Linse T, Kuna M, Viehrig HW. Quantification of brittle-ductile failure behavior of ferritic reactor pressure vessel steels using the Small-Punch-Test and micromechanical damage models. Materials Science and Engineering A [Internet]. 2014;614:136–47. Available from: http://dx.doi.org/10.1016/j.msea.2014.05.095

57. Acharya S, Ray KK. Assessment of tensile properties of spot welds using shear punch test. Materials Science and Engineering: A. 2013 Mar 10;565:405–13.

58. Goyal S, Karthik V, Kasiviswanathan K V., Valsan M, Rao KBS, Raj B. Finite element analysis of shear punch testing and experimental validation. Mater Des. 2010 May 1;31(5):2546–52.

59. Schmid H, Hetz P, Merklein M. Failure behavior of different sheet metals after passing a drawbead. Procedia Manuf. 2019 May;34:125–32.

60. Emanuela A, Marion M. Metallographic Analysis of Nakajima Tests for the Evaluation of the Failure Developments. Procedia Eng [Internet]. 2017;183:83–8. Available from: https://www.sciencedirect.com/science/article/pii/S1877705817315205

61. Khalilabad M, Perdahcıoglu E, Atzema E, den Boogaard T. An In-Plane Bending Test to Characterize Edge Ductility in High-Strength Steels. J Mater Eng Perform. 2022 May;

62. Schmid H, Suttner S, Merklein M. An incremental analysis of a deep drawing steel's material behaviour undergoing the predeformation using drawbeads. J Phys Conf Ser. 2017 May;896:12010.

63. Keeler SP. Plastic instability and fracture in sheets stretched over rigid punches. In 1961. Available from: https://api.semanticscholar.org/CorpusID:139249997

64. Zhang L, Harrison W, Abdullah T, Mehraban S, Lavery NP. Formability prediction of interstitial-free steel via miniaturized tensile specimen for Rapid Alloy Prototyping. Appl Math Model [Internet]. 2023;124:713–33. Available from: https://www.sciencedirect.com/science/article/pii/S0307904X23003761

65. Mirmohammad H, Sarker S, Berke R, Kingstedt O. A multi-length-scale investigation of the applicability of ductility laws for annealed and work-hardened copper. Materials Science and Engineering: A [Internet]. 2023;883:145464. Available from: https://www.sciencedirect.com/science/article/pii/S0921509323008882

66. Cola Jr GM, Hanhold B, Lolla T, Radhakrishnan B, Babu S. On the tensile elongation of advanced high-strength steels. Iron & Steel Technology. 2013;10(4):276–81.

67. JAGOTA V, SETHI APS, KUMAR K. Finite Element Method: An Overview. Walailak Journal of Science and Technology (WJST) [Internet]. 2013 Jan;10(1):1–8. Available from: https://wjst.wu.ac.th/index.php/wjst/article/view/499

68. Zienkiewicz OC, Taylor RL, Nithiarasu P, editors. The Finite Element Method for Fluid Dynamics. In: The Finite Element Method for Fluid Dynamics (Seventh Edition) [Internet]. Seventh Edition. Oxford: Butterworth-Heinemann; 2014. p. iii. Available from: https://www.sciencedirect.com/science/article/pii/B9781856176354000182

69. Wilson EL, Bathe KJ, Peterson FE. Finite element analysis of linear and nonlinear heat transfer. Nuclear Engineering and Design [Internet]. 1974;29(1):110–24. Available from: https://www.sciencedirect.com/science/article/pii/0029549374901010

70. Biro O, Preis K. Finite element analysis of 3-D eddy currents. IEEE Trans Magn. 1990;26(2):418–23.

71. Sabat Lovely and Kundu CK. History of Finite Element Method: A Review. In: Das Bibhuti Bhusan and Barbhuiya S and GR and SP, editor. Recent Developments in Sustainable Infrastructure . Singapore: Springer Singapore; 2021. p. 395–404.

72. Kuczmann M. Overview of the Finite Element Method. Acta Technica Jaurinensis. 2015 May;8:347.

73. Aragón AM, Duarte CA. 2 - The finite element method. In: Aragón AM, Duarte CA, editors. Fundamentals of Enriched Finite Element Methods [Internet]. Elsevier; 2024. p. 13–56. Available from: https://www.sciencedirect.com/science/article/pii/B978032385515000009X

74. Nakata T, Komazaki S, Kohno Y, Tanigawa H. Effects of Geometry and Dimension of Specimen and Rig on Small Punch Creep Property. Exp Mech [Internet]. 2017;57(3):487–94. Available from: https://doi.org/10.1007/s11340-016-0250-2

75. ABAQUS/Standard User's Manual, Version 6.9. United States: Dassault Systèmes Simulia Corp; 2019.

76. Harewood FJ, McHugh PE. Comparison of the implicit and explicit finite element methods using crystal plasticity. Comput Mater Sci [Internet]. 2007;39(2):481–94. Available from: https://www.sciencedirect.com/science/article/pii/S0927025606002278

77. Börgesson L. ABAQUS. In: Stephansson O, Jing L, Tsang CF, editors. Coupled Thermo-Hydro-Mechanical Processes of Fractured Media [Internet]. Elsevier; 1996. p. 565–70. (Developments in Geotechnical Engineering; vol. 79). Available from: https://www.sciencedirect.com/science/article/pii/S0165125096800472

78. Karthik V, Laha K, Parameswaran P, Chandravathi KS, Kasiviswanathan K V., Jayakumar T, et al. Tensile properties of modified 9Cr-1Mo steel by shear punch testing and correlation with microstructures. International Journal of Pressure Vessels and Piping. 2011 Oct 1;88(10):375–83.

79. Mahmudi R, Sadeghi M. Correlation between shear punch and tensile strength for low-carbon steel and stainless steel sheets. J Mater Eng Perform. 2013 Feb 1;22(2):433–8.

80. Quitzke C, Schröder C, Ullrich C, Mandel M, Krüger L, Volkova O, et al. Evaluation of strain-induced martensite formation and mechanical properties in N-alloyed austenitic stainless steels by in situ tensile tests. Materials Science and Engineering: A [Internet]. 2021;808:140930. Available from: https://www.sciencedirect.com/science/article/pii/S0921509321001994

81. Zhang Q, Ma S, Jing T. Mechanical Properties of a Thermally-aged Cast Duplex Stainless Steel by in Situ Tensile Test at the Service Temperature. Metals

(Basel) [Internet]. 2019;9(3). Available from: https://www.mdpi.com/2075-4701/9/3/317

82. Haddad M, Ivanisenko Y, Courtois-Manara E, Fecht HJ. In-situ tensile test of high strength nanocrystalline bainitic steel. Materials Science and Engineering: A [Internet]. 2015;620:30–5. Available from: https://www.sciencedirect.com/science/article/pii/S0921509314012040

83. Haque MA, Saif MTA. In-situ tensile testing of nano-scale specimens in SEM and TEM. Exp Mech [Internet]. 2002;42(1):123–8. Available from: https://doi.org/10.1007/BF02411059

84. Wilkinson AJ, Britton TBen. Strains, planes, and EBSD in materials science. Materials Today [Internet]. 2012;15(9):366–76. Available from: https://www.sciencedirect.com/science/article/pii/S1369702112701633

85. Brewer Luke N. and Field DP and MCC. Mapping and Assessing Plastic Deformation Using EBSD. In: Schwartz Adam J. and Kumar M and ABL and FDP, editor. Electron Backscatter Diffraction in Materials Science [Internet]. Boston, MA: Springer US; 2009. p. 251–62. Available from: https://doi.org/10.1007/978-0-387-88136-2_18

86. Ryde L. Application of EBSD to analysis of microstructures in commercial steels. Materials Science and Technology [Internet]. 2006;22(11):1297–306. Available from: https://doi.org/10.1179/174328406X130948

87. Lee T, Lee H, Kang SJ, Ibupoto FA, Lee JM, Lee JH, et al. Small punch test and simulation of HR3C steel. Journal of Mechanical Science and Technology. 2018;32(7):3115–21.

88. Brown V. Finite Element Modelling of the Small Punch Test for Structure Critical Design. 2020;(November).

89. Hähner P, Soyarslan C, Gülçimen Çakan B, Bargmann S. Determining tensile yield stresses from Small Punch tests: A numerical-based scheme. Mater Des. 2019 Nov 15;182:107974.

90. Cuesta II, Alegre JM, Lacalle R. Determination of the Gurson-Tvergaard damage model parameters for simulating small punch tests. Fatigue Fract Eng Mater Struct. 2010;33(11):703–13.

91. Calaf Chica J, Bravo Díez PM, Preciado Calzada M. Development of an improved prediction method for the yield strength of steel alloys in the Small Punch Test. Mater Des. 2018 Jun 15;148:153–66.

92. Abendroth M. FEM Analysis of Small Punch Tests. In: Small Sample Test Technique. Trans Tech Publications Ltd; 2017. p. 23–36. (Key Engineering Materials; vol. 734).

93. CEN Workshop Business Plan CEN Workshop Business Plan : 'Small Punch Test Method for Metallic Materials' 1 The CEN Workshop.

94. Dymáček P, Seitl S, Milička K, Dobeš F. Influence of Friction on Stress and Strain Distributions in Small Punch Creep Test Models. In: Advances in Fracture and Damage Mechanics VIII. Trans Tech Publications Ltd; 2010. p. 561–4. (Key Engineering Materials; vol. 417).

95. Reid JD, Hiser NR. Friction modelling between solid elements. International Journal of Crashworthiness [Internet]. 2004;9(1):65–72. Available from: https://doi.org/10.1533/ijcr.2004.0272

96. Ramazani A, Schwedt A, Aretz A, Prahl U, Bleck W. Characterization and modelling of failure initiation in DP steel. Comput Mater Sci. 2013 Jul 1;75:35–44.

97. Kadkhodapour J, Butz A, Ziaei-Rad S, Schmauder S. A micro mechanical study on failure initiation of dual phase steels under tension using single crystal plasticity model. Int J Plast. 2011 Jul 1;27(7):1103–25.

98. Ghadbeigi H, Pinna C, Celotto S. Failure mechanisms in DP600 steel: Initiation, evolution and fracture. Materials Science and Engineering A. 2013 Dec 20;588:420–31.

99. Paul SK. Real microstructure based micromechanical model to simulate microstructural level deformation behavior and failure initiation in DP 590 steel. Mater Des. 2013 Feb 1;44:397–406.

100. Paul SK. Effect of martensite volume fraction on stress triaxiality and deformation behavior of dual phase steel. Mater Des. 2013 Sep 1;50:782–9.

101. Shen HP, Lei TC, Liu JZ. Microscopic deformation behaviour of martensitic–ferritic dual-phase steels. Materials Science and Technology [Internet]. 1986;2(1):28–33. Available from: https://doi.org/10.1179/mst.1986.2.1.28

102. Ramazani A, Abbasi M, Kazemiabnavi S, Schmauder S, Larson R, Prahl U. Development and application of a microstructure-based approach to characterize and model failure initiation in DP steels using XFEM. Materials Science and Engineering A. 2016 Apr 13;660:181–94.

103. Avramovic-Cingara G, Saleh CAR, Jain MK, Wilkinson DS. Void nucleation and growth in dual-phase steel 600 during uniaxial tensile testing. Metall Mater Trans A Phys Metall Mater Sci. 2009 Dec;40(13):3117–27.

104. Santos RO, Da Silveira LB, Moreira LP, Cardoso MC, Da Silva FRF, Dos Santos Paula A, et al. Damage identification parameters of dual-phase 600-800 steels based on experimental void analysis and finite element simulations. Journal of Materials Research and Technology. 2019 Jan 1;8(1):644–59.

105. Ch.Darabi A, Chamani HR, Kadkhodapour J, Anaraki AP, Alaie A, Ayatollahi MR. Micromechanical analysis of two heat-treated dual phase steels: DP800 and DP980. Mechanics of Materials. 2017 Jul 1;110:68–83.

106. Nick M, Feuerhack A, Bergs T, Clausmeyer T. Numerical Investigation of Damage in Single-step, Two-step, and Reverse Deep Drawing of Rotationally Symmetric Cups from DP800 Dual Phase Steel. Procedia Manuf. 2020 Jan 1;47:636–42.

107. H.P. Shen TCL, Liu JZ. Microscopic deformation behaviour of martensitic–ferritic dual-phase steels. Materials Science and Technology [Internet]. 1986;2(1):28–33. Available from: https://doi.org/10.1179/mst.1986.2.1.28

108. Ramazani A, Ebrahimi Z, Prahl U. Study the effect of martensite banding on the failure initiation in dual-phase steel. Comput Mater Sci. 2014 May 1;87:241–7.

109. Fonstein N. 7 - Dual-phase steels. In: Rana R, Singh SB, editors. Automotive Steels [Internet]. Woodhead Publishing; 2017. p. 169–216. Available from: https://www.sciencedirect.com/science/article/pii/B9780081006382000079

110. Ghassemi-Armaki H, Maaß R, Bhat SP, Sriram S, Greer JR, Kumar KS. Deformation response of ferrite and martensite in a dual-phase steel. Acta Mater [Internet]. 2014;62:197–211. Available from: https://www.sciencedirect.com/science/article/pii/S1359645413007477

111. Ishikawa T. 1 - Understanding and controlling microstructural evolution in metal forming: an overview. In: Lin J, Balint D, Pietrzyk M, editors. Microstructure Evolution in Metal Forming Processes [Internet]. Woodhead Publishing; 2012. p. 3–16. (Woodhead Publishing Series in Metals and Surface Engineering). Available from: https://www.sciencedirect.com/science/article/pii/B9780857090744500016

112. Rashid MS. Dual Phase Steels. Annu Rev Mater Res [Internet]. 1981;11(Volume 11, 1981):245–66. Available from: https://www.annualreviews.org/content/journals/10.1146/annurev.ms.11.080181.001333

113. Yan B, Laurin K, Xu K, Sriram S, Huang M, Chintamani J, et al. A New Dual Phase Steel for Automotive Body Panels. SAE Transactions [Internet]. 2003;112:228–37. Available from: http://www.jstor.org/stable/44699577

114. Park KS, Park KT, Lee DL, Lee CS. Effect of heat treatment path on the cold formability of drawn dual-phase steels. Materials Science and Engineering: A [Internet]. 2007;449–451:1135–8. Available from: https://www.sciencedirect.com/science/article/pii/S0921509306013141

115. Saeidi N, Ashrafizadeh F, Niroumand B, Forouzan MR, Barlat F. Damage mechanism and modeling of void nucleation process in a ferrite–martensite dual phase steel. Eng Fract Mech. 2014 Sep 1;127:97–103.

116. Tasan CC, Diehl M, Yan D, Bechtold M, Roters F, Schemmann L, et al. An overview of dual-phase steels: advances in microstructure-oriented processing and micromechanically guided design. Annu Rev Mater Res. 2015;45(1):391–431.

117. Cheloee Darabi A, Kadkhodapour J, Pourkamali Anaraki A, Khoshbin M, Alaie A, Schmauder S. Micromechanical modeling of damage mechanisms in dual-phase steel under different stress states. Eng Fract Mech. 2021 Feb 15;243:107520.

118. Topilla L, Toros S. Stress-strain distribution and failure mechanisms in dual-phase steels investigated with microstructure-based modeling. Latin American Journal of Solids and Structures. 2022;19(7):e468.

119. Tasan CC, Hoefnagels JPM, Diehl M, Yan D, Roters F, Raabe D. Strain localization and damage in dual phase steels investigated by coupled in-situ deformation experiments and crystal plasticity simulations. Int J Plast. 2014 Dec 1;63:198–210.

120. Krauss G. Martensite in steel: strength and structure. Materials Science and Engineering: A [Internet]. 1999;273–275:40–57. Available from: https://www.sciencedirect.com/science/article/pii/S0921509399002889

121. Zucchetti M, Testoni R. Essays on Nuclear Technology. Volume 1: 2018. 2018.

122. Calcagnotto M, Adachi Y, Ponge D, Raabe D. Deformation and fracture mechanisms in fine- and ultrafine-grained ferrite/martensite dual-phase steels and the effect of aging. Acta Mater [Internet]. 2011;59(2):658–70. Available from: https://www.sciencedirect.com/science/article/pii/S1359645410006488

123. Ramazani A, Schwedt A, Aretz A, Prahl U, Bleck W. Characterization and modelling of failure initiation in DP steel. Comput Mater Sci [Internet]. 2013;75:35–

44. Available from:
https://www.sciencedirect.com/science/article/pii/S0927025613001614

124. Sherman AM, Davies RG. Influence of martensite carbon content on the cyclic properties of dual-phase steel. Int J Fatigue [Internet]. 1981;3(4):195–8. Available from:
https://www.sciencedirect.com/science/article/pii/0142112381900207

125. Liedl U, Traint S, Werner EA. An unexpected feature of the stress–strain diagram of dual-phase steel. Comput Mater Sci [Internet]. 2002;25(1):122–8. Available from:
https://www.sciencedirect.com/science/article/pii/S0927025602002562

126. Paul SK. Effect of forming strain on low cycle, high cycle and notch fatigue performance of automotive grade dual phase steels: A review. Forces in Mechanics [Internet]. 2023;11:100184. Available from:
https://www.sciencedirect.com/science/article/pii/S2666359723000197

127. Kim JH, Kim D, Barlat F, Lee MG. Crystal plasticity approach for predicting the Bauschinger effect in dual-phase steels. Materials Science and Engineering A. 2012 Mar 30;539:259–70.

128. Calcagnotto M, Ponge D, Raabe D. On the effect of manganese on grain size stability and hardenability in ultrafine-grained ferrite/martensite dual-phase steels. Metall Mater Trans A Phys Metall Mater Sci. 2012 Jan;43(1):37–46.

129. Bouaziz O, Embury JD. Microstructural Design for Advanced Structural Steels. In: THERMEC 2006. Trans Tech Publications Ltd; 2007. p. 42–50. (Materials Science Forum; vol. 539).

130. Kumar A, Singh SB, Ray KK. Influence of bainite/martensite-content on the tensile properties of low carbon dual-phase steels. Materials Science and Engineering: A [Internet]. 2008;474(1):270–82. Available from:
https://www.sciencedirect.com/science/article/pii/S0921509307010179

131. de la Concepción VL, Lorusso HN, Svoboda HG. Effect of Carbon Content on Microstructure and Mechanical Properties of Dual Phase Steels. Procedia Materials Science [Internet]. 2015;8:1047–56. Available from: https://www.sciencedirect.com/science/article/pii/S2211812815001686

132. Lanzillotto CAN, Pickering FB. Structure–property relationships in dual-phase steels. Metal Science [Internet]. 1982;16(8):371–82. Available from: https://doi.org/10.1179/030634582790427433

133. Abid NH, Abu Al-Rub RK, Palazotto AN. Micromechanical finite element analysis of the effects of martensite morphology on the overall mechanical behavior of dual phase steel. Int J Solids Struct [Internet]. 2017;104–105:8–24. Available from: https://www.sciencedirect.com/science/article/pii/S0020768316303286

134. Ismail K, Perlade A, Jacques PJ, Pardoen T, Brassart L. Impact of second phase morphology and orientation on the plastic behavior of dual-phase steels. Int J Plast [Internet]. 2019;118:130–46. Available from: https://www.sciencedirect.com/science/article/pii/S0749641918304893

135. Zhang J, Di H, Deng Y, Misra RDK. Effect of martensite morphology and volume fraction on strain hardening and fracture behavior of martensite–ferrite dual phase steel. Materials Science and Engineering: A [Internet]. 2015;627:230–40. Available from: https://www.sciencedirect.com/science/article/pii/S0921509315000118

136. Pierman AP, Bouaziz O, Pardoen T, Jacques PJ, Brassart L. The influence of microstructure and composition on the plastic behaviour of dual-phase steels. Acta Mater [Internet]. 2014;73:298–311. Available from: https://www.sciencedirect.com/science/article/pii/S1359645414002547

137. Tasan CC, Diehl M, Yan D, Bechtold M, Roters F, Schemmann L, et al. An Overview of Dual-Phase Steels: Advances in Microstructure-Oriented Processing and Micromechanically Guided Design. Annu Rev Mater Res [Internet]. 2015;45(Volume 45, 2015):391–431. Available from:

https://www.annualreviews.org/content/journals/10.1146/annurev-matsci-070214-021103

138. Kim NJ, Thomas G. EFFECTS OF MORPHOLOGY ON THE MECHANICAL BEHAVIOR OF A DUAL PHASE Fe/2Si/0. 1C STEEL. Metallurgical transactions A, Physical metallurgy and materials science. 1981;12 A(3):483–9.

139. Leslie WC, Hornbogen E. Physical metallurgy of steels. Physical metallurgy. 1996;1555–620.

140. Zhang L, Harrison W, Yar MA, Brown SGR, Lavery NP. The development of miniature tensile specimens with non-standard aspect and slimness ratios for rapid alloy prototyping processes. Journal of Materials Research and Technology [Internet]. 2021;15:1830–43. Available from: https://www.sciencedirect.com/science/article/pii/S2238785421010103

141. Niu L, Cao M, Liang Z, Han B, Zhang Q. A modified Johnson-Cook model considering strain softening of A356 alloy. 2020; Available from: https://doi.org/10.1016/j.msea.2020.139612

142. Hoile S. Processing and properties of mild interstitial free steels. Materials Science and Technology [Internet]. 2000;16(10):1079–93. Available from: https://journals.sagepub.com/doi/abs/10.1179/026708300101506902

143. Loveday MS, Gray T, Aegerter J. Tensile testing of metallic materials: A review. Final report of the TENSTAND project of work package. 2004;1.

144. Shrot A, Bäker M. Determination of Johnson-Cook parameters from machining simulations. Comput Mater Sci [Internet]. 2012;52(1):298–304. Available from: http://dx.doi.org/10.1016/j.commatsci.2011.07.035

145. Milani AS, Dabboussi W, Nemes JA, Abeyaratne RC. An improved multi-objective identification of Johnson-Cook material parameters. Int J Impact Eng [Internet]. 2009;36(2):294–302. Available from: http://dx.doi.org/10.1016/j.ijimpeng.2008.02.003

146. Umbrello D, M'Saoubi R, Outeiro JC. The influence of Johnson-Cook material constants on finite element simulation of machining of AISI 316L steel. Int J Mach Tools Manuf. 2007;47(3–4):462–70.

147. Nam HS, Kim JS, Han JJ, Kim JW, Kim YJ. Ductile fracture simulation for A106 Gr.B carbon steel under high strain rate loading condition. In: Ye L, editor. Recent Advances in Structural Integrity Analysis - Proceedings of the International Congress (APCF/SIF-2014) [Internet]. Oxford: Woodhead Publishing; 2014. p. 37–41. Available from: https://www.sciencedirect.com/science/article/pii/B9780081002032500085

148. Wang X, Chandrashekhara K, Rummel SA, Lekakh S, Van Aken DC, O'Malley RJ. Modeling of mass flow behavior of hot rolled low alloy steel based on combined Johnson-Cook and Zerilli-Armstrong model. J Mater Sci. 2017 Mar 1;52(5):2800–15.

149. Eshtayeh MM, Hrairi M. Recent and future development of the application of finite element analysis in clinching process. The International Journal of Advanced Manufacturing Technology [Internet]. 2016;84(9):2589–608. Available from: https://doi.org/10.1007/s00170-015-7781-z

150. Zergani A, Mirzadeh H, Mahmudi R. Finite element analysis of plastic deformation in shear punch test. Mater Lett. 2021 Feb 1;284:128953.

151. Martínez-Pañeda E, Cuesta II, Peñuelas I, Díaz A, Alegre JM. Damage modeling in Small Punch Test specimens. 2016;

152. Šulda J, Adámek V. Non-Stationary Waves in Thick Elastic and Viscoelastic Plates. In 2024. p. 294–7.

153. Kim SA, Johnson WL. Elastic constants and internal friction of martensitic steel, ferritic-pearlitic steel, and α-iron. Materials Science and Engineering A. 2007 Apr 15;452–453:633–9.

154. Webber E, Knezevic M. Assessing strength of ferrite and martensite in five dual phase and two martensitic steels via high throughput nanoindentation to

elucidate origins of strength. Journal of Materials Research and Technology [Internet]. 2024;33:3635–48. Available from: https://www.sciencedirect.com/science/article/pii/S223878542402324X

155. Atreya V, Van Dokkum JS, Bos C, Santofimia MJ. Effect of the anisotropy of martensitic transformation on ferrite deformation in Dual-Phase steels. Mater Des. 2022 Jul 1;219.

156. Rodriguez RM, Gutiérrez I. Unified Formulation to Predict the Tensile Curves of Steels with Different Microstructures. In: THERMEC'2003. Trans Tech Publications Ltd; 2003. p. 4525–30. (Materials Science Forum; vol. 426).

157. B. Joós, M. S. Duesbuery. The Peierls Stress of Dislocations: An Analytic Formula. Phys Rev Lett [Internet]. 1997 Jan 13 [cited 2024 Sep 23];(78):266–9. Available from: https://link.aps.org/doi/10.1103/PhysRevLett.78.266

158. Nam WJ, Bae CM. Microstructural evolution and its relation to mechanical properties in a drawn dual-phase steel. J Mater Sci. 1999;34:5661–8.

159. Li S, Sitnikova E. Chapter 6 - Formulation of unit cells. In: Li S, Sitnikova E, editors. Representative Volume Elements and Unit Cells [Internet]. Woodhead Publishing; 2020. p. 107–87. (Woodhead Publishing Series in Composites Science and Engineering). Available from: https://www.sciencedirect.com/science/article/pii/B9780081026380000062

160. Tian C, Kusche CF, Medina A, Lee S, Wollenweber MA, Pippan R, et al. Understanding the damage initiation and growth mechanisms of two DP800 dual phase grades. Mater Des [Internet]. 2024;238:112630. Available from: https://www.sciencedirect.com/science/article/pii/S0264127524000029

161. Deng N, Korkolis YP. Elastic anisotropy of dual-phase steels with varying martensite content. Int J Solids Struct [Internet]. 2018;141–142:264–78. Available from: https://www.sciencedirect.com/science/article/pii/S0020768318300854

162. Huang JX, Liu Y, Xu T, Chen XF, Lai QQ, Xiao LR, et al. Dual-phase hetero-structured strategy to improve ductility of a low carbon martensitic steel.

Materials Science and Engineering: A [Internet]. 2022;834:142584. Available from: https://www.sciencedirect.com/science/article/pii/S092150932101844X

163. Saai A, Hopperstad O, Fritz J, Larsson J. A numerical study on the effects of DP steel microstructure on the yield locus and the stress–strain response under strain path change. International Journal of Material Forming. 2023 Jun;16.

164. Raabe D, Sun B, Kwiatkowski Da Silva A, Gault B, Yen HW, Sedighiani K, et al. Current Challenges and Opportunities in Microstructure-Related Properties of Advanced High-Strength Steels. Metall Mater Trans A Phys Metall Mater Sci [Internet]. 2020 Nov 1 [cited 2021 Apr 15];51(11):5517–86. Available from: https://doi.org/10.1007/s11661-020-05947-2

165. Sun X, Choi KS, Soulami A, Liu WN, Khaleel MA. On key factors influencing ductile fractures of dual phase (DP) steels. Materials Science and Engineering: A [Internet]. 2009;526(1):140–9. Available from: https://www.sciencedirect.com/science/article/pii/S0921509309009071

166. Quey R, Kasemer M. The Neper/FEPX Project: Free / Open-source Polycrystal Generation, Deformation Simulation, and Post-processing. IOP Conf Ser Mater Sci Eng [Internet]. 2022 Jul;1249(1):12021. Available from: https://dx.doi.org/10.1088/1757-899X/1249/1/012021